

Enhanced sheet conductivity of Langmuir–Blodgett assembled graphene thin films by chemical doping

This content has been downloaded from IOPscience. Please scroll down to see the full text.

2016 2D Mater. 3 015002

(<http://iopscience.iop.org/2053-1583/3/1/015002>)

View [the table of contents for this issue](#), or go to the [journal homepage](#) for more

Download details:

IP Address: 132.239.1.230

This content was downloaded on 18/01/2016 at 18:44

Please note that [terms and conditions apply](#).

2D Materials



PAPER

Enhanced sheet conductivity of Langmuir–Blodgett assembled graphene thin films by chemical doping

RECEIVED
14 August 2015

REVISED
6 November 2015

ACCEPTED FOR PUBLICATION
15 December 2015

PUBLISHED
18 January 2016

Aleksandar Matković¹, Ivana Milošević¹, Marijana Milićević¹, Tijana Tomašević-Ilić¹, Jelena Pešić¹, Milenko Musić¹, Marko Spasenović¹, Djordje Jovanović¹, Borislav Vasić¹, Christopher Deeks², Radmila Panajotović¹, Milivoj R Belić³ and Radoš Gajić¹

¹ Center for Solid State Physics and New Materials, Institute of Physics, University of Belgrade, Pregrevica 118, 11080 Belgrade, Serbia

² Thermo Fisher Scientific, Unit 24, The Birches Industrial Estate, East Grinstead, RH19 1UB, UK

³ Texas A & M University at Qatar, PO Box 23874 Doha, Qatar

E-mail: amatkovic@ipb.ac.rs

Keywords: graphene, nitric acid doping, Langmuir–Blodgett assembly, enhanced conductivity

Supplementary material for this article is available [online](#)

Abstract

We demonstrate a facile fabrication technique for highly conductive and transparent thin graphene films. Sheet conductivity of Langmuir–Blodgett assembled multi-layer graphene films is enhanced through doping with nitric acid, leading to a fivefold improvement while retaining the same transparency as un-doped films. Sheet resistivity of such chemically improved films reaches $10 \text{ k}\Omega/\square$, with optical transmittance 78% in the visible. When the films are encapsulated, the enhanced sheet conductivity effect is stable in time. In addition, stacking of multiple layers, as well as the dependence of the sheet resistivity upon axial strain have been investigated.

1 Introduction

Graphene has a multitude of potential applications from high-speed electronics, to energy storage and conversion, to use as transparent conductor [1–3]. As graphene technology matures, applications are moving from the lab to the market, and the performance-to-cost ratio is becoming a crucial parameter in technology adoption, raising the importance of scalable and cost effective routes for production of graphene and related materials [4–7].

Transparent conductive electrodes (TCEs) [8] are an exemplary technology for which graphene offers key advantages compared to established standards. The unique properties that graphene TCEs offer are flexibility [9], thermal and chemical stability [10, 11], functionalization [12] and ease of integration with organic semiconductors [13–15]. Therefore, the use of graphene has already been demonstrated in photovoltaic solar cells [11, 16–18], liquid crystal displays [10], touch-screen panels [19], organic light emitting diodes [20, 21] and many others.

Most of these applications currently rely on graphene obtained through chemical vapor deposition (CVD) [22–24]. Although the CVD process

produces some of the highest quality graphene films [25], there are several drawbacks of this technique. CVD of graphene requires high growth temperatures, a vacuum environment and transfer from the metallic substrate, during which the costly metal is usually sacrificed [26]. Nonetheless, multiple layers of CVD graphene grown on copper, transferred, stacked [27] and chemically doped [19, 28] have managed to surpass the industry standard [8] for TCEs set by indium–tin–oxide.

A low-cost alternative to CVD is solution-processed synthesis of graphene and related materials, the first experiments of which yielded graphene oxide [29–31]. Solution-processed sheets of reduced graphene oxide are functionalized with hydroxyls and epoxides and cannot be fully reduced to graphene, which limits film conductance. This issue can be overcome by using a non-covalent liquid phase exfoliation (LPE) of graphite in organic solvents with matching surface energy. LPE was first demonstrated for graphene [10, 32, 33], and then adopted for other two-dimensional materials such as boron-nitride, MoS_2 , WS_2 , WSe_2 and other [7, 34–36]. LPE of graphite results in a dispersion of graphene and multi-layer graphene sheets (GSs) in the solvent. There are many ways

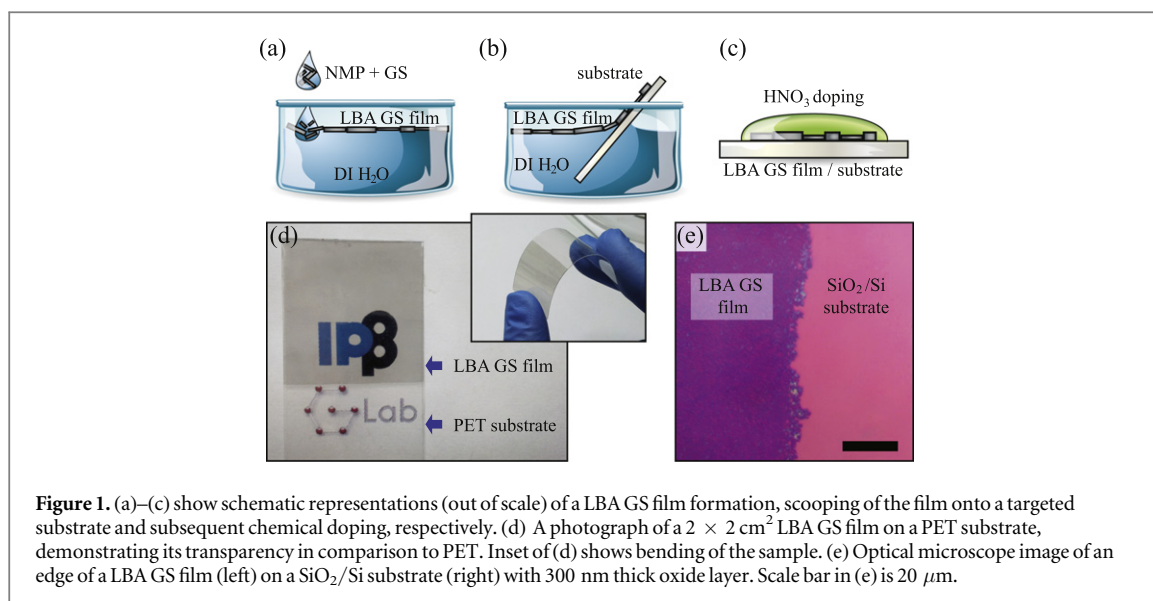


Figure 1. (a)–(c) show schematic representations (out of scale) of a LBA GS film formation, scooping of the film onto a targeted substrate and subsequent chemical doping, respectively. (d) A photograph of a $2 \times 2 \text{ cm}^2$ LBA GS film on a PET substrate, demonstrating its transparency in comparison to PET. Inset of (d) shows bending of the sample. (e) Optical microscope image of an edge of a LBA GS film (left) on a SiO_2/Si substrate (right) with 300 nm thick oxide layer. Scale bar in (e) is $20 \mu\text{m}$.

to deposit these sheets onto a targeted substrate, for example spray coating [10], ink-jet printing [37–39], vacuum filtration [31, 40], Langmuir–Blodgett assembly (LBA) [41–44], or self-assembly on a liquid–liquid interface [45–47]. Still, the electronic conductance of LPE films is inferior to that of CVD graphene, and any improvement is a step towards industrial applications of solution processed graphene.

We make transparent conductive films of multilayer GSs on flexible polyethylene terephthalate (PET) by LBA on a water–air interface. The sheets adhere strongly to the PET substrate, which allows immersion into other liquids without the risk of the film washing away. We make use of the strong adhesion to chemically dope the graphene in nitric acid for enhanced conductivity, and to stack multiple films on top of each other, opening a gateway to liquid phase assembly of Van der Waals heterostructures [36, 48, 49]. The power of this method is demonstrated by the fivefold reduction in sheet resistivity for a single LBA layer, while maintaining the same optical transparency of the unperturbed films.

We show that LBA GS films can be very effectively p-doped by nitric acid, making them a more suitable low-cost alternative to CVD graphene for various TCE applications. As indicated by the work function measurements and by the measurements of the sheet resistivity under axial strain, chemical doping does not only increase carrier concentration of individual GSs, but also reduces the contact resistance between GSs, which additionally contributes to a larger reduction factor of the sheet resistivity.

2 LBA GS film fabrication and morphological characterization

2.1 Preparation of GS dispersion

As a starting material for the formation of LBA layers, a dispersion of GSs in *N*-methylpyrrolidone (NMP) has

been used. The dispersion fabrication process is based on the earlier established protocol [32]. An initial concentration of graphite powder (Sigma Aldrich-332461) was 18 mg ml^{-1} in NMP (Sigma Aldrich-328634). The solution was sonicated in a low-power ultrasonic bath for 14 h, and centrifuged for one hour at 3000 rpm immediately after sonication. The results of this process are GSs in solution, with a concentration of 0.36 mg ml^{-1} . The concentration was determined via UV–VIS spectrophotometry (SUPER SCAN, Varian) [32]. This particular set of LPE parameters was chosen since the resulting dispersion of GSs in NMP was found to be stable for over six months.

2.2 Langmuir–Blodgett assembly

GSs suspended in NMP were used to fabricate transparent and conductive films by LBA at a water–air interface [43]. Since the LPE process introduces a low degree of oxidation and covalent functionalization, resulting GSs have high hydrophobicity, which is very favorable for the formation of LBA layers [41]. Furthermore, driven by the minimization of interfacial energy, LBA produces a close packed structure of GSs [45]. A schematic representation of LBA GS film formation is presented in figure 1(a). Beakers filled with deionized water ($18.2 \text{ M}\Omega$) with a water–air interface surface-to-water volume ratio of 0.5 cm^{-1} were used for film formation. A 1.5–2 vol% of GS + NMP was added to the interface with a continuous flow rate of $5\text{--}10 \mu\text{l s}^{-1}$. A closely packed LBA GS film was found to form on the water–air interface with this set of parameters. Formation of the LBA film was found to be self-limiting, meaning that prior to the film formation on the whole given surface, added GSs are fixed at the interface, and after the complete film was formed, any additional GSs fall through the interface to the bottom of the beaker. Only several microliters of the GS+NMP solution are needed to

fabricate several square centimeters of film. When scaled up, one liter of GS+NMP solution would be sufficient to produce $150 \times 150 \text{ m}^2$ of LBA GS films. Compared to CVD graphene, fabrication cost of these TCEs would be at least three orders of magnitude smaller [4].

2.3 Deposition on a substrate and chemical doping

Interestingly, as proposed by Kim *et al* [43], this process dissolves NMP in the water, effectively removing most of the solvent from the graphene layer. After the film is formed, it is slowly scooped onto the targeted substrate, as schematically presented in figure 1(b). The substrate was either pre-positioned vertically at the edge of the beaker, or was introduced after the LBA film was formed, puncturing the film near the edge of the beaker. Films are then left to dry for several minutes in ambient conditions. After the films were transferred onto the targeted substrates their sheet conductivity was enhanced by chemical doping. This was achieved either by dipping into or covering LBA GS films with a 65% solution of nitric acid in water (see figure 1(c)), followed by quick drying with an air gun.

Our procedure yields quality films on all tested substrates, including SiO_2/Si , quartz, glass and PET. We typically pre-fabricated $\sim 50 \text{ nm}$ thick gold electrodes on the substrates prior to GS deposition. Figures 1(d) and (e) show LBA GS films on the PET and SiO_2/Si substrate, respectively. Films fabricated with this method are uniform over the entire substrate area. Up to several square centimeters of uniform LBA GS films on various substrates were fabricated using this technique, with sheet conductivity and optical transparency not varying more than 5% from the mean value over the entire film.

2.4 Film morphology

The morphology of the obtained LBA GS films was characterized with atomic force microscopy (AFM) and scanning electron microscopy (SEM). AFM measurements were carried out on an atomic force microscope, NTEGRA Spectra, in tapping mode. A typical AFM profile of an LBA GS film on a SiO_2/Si substrate is shown in figure 2(a). SiO_2/Si was chosen as a substrate for AFM due to its low surface roughness. Figure 2(b) shows a height histogram of a $5 \times 5 \mu\text{m}^2$ AFM topography image containing a sharp edge of the LBA GS layer (inset). Ten height histograms of sample/substrate edge areas were used to estimate the thickness of LBA GS films. Each histogram had two clearly resolved peaks corresponding to LBA GS film and the substrate. An average film thickness was estimated as a peak-to-peak distance. While the substrate peak is narrow, due to the low roughness of the SiO_2 , (left peak in figure 2(b)), the LBA GS film has a much broader height distribution. The sample peak was fitted with a log-normal curve, yielding a mean

film thickness (3.4 ± 0.7) nm. This indicates that LBA GS films have an average thickness of ~ 10 layers.

The lateral profile of graphene flakes was analyzed with a Tescan MIRA3 field-emission gun SEM. A histogram of flake diameter is presented in figure 2(c). The distribution of flake diameters from six $5 \times 5 \mu\text{m}^2$ SEM images (~ 2000 flakes) was fitted with a log-normal curve, giving an average flake diameter of 120 nm. Both AFM and SEM images were used to estimate a surface coverage of over 90%.

3 Results and discussion

3.1 Nitric acid doping

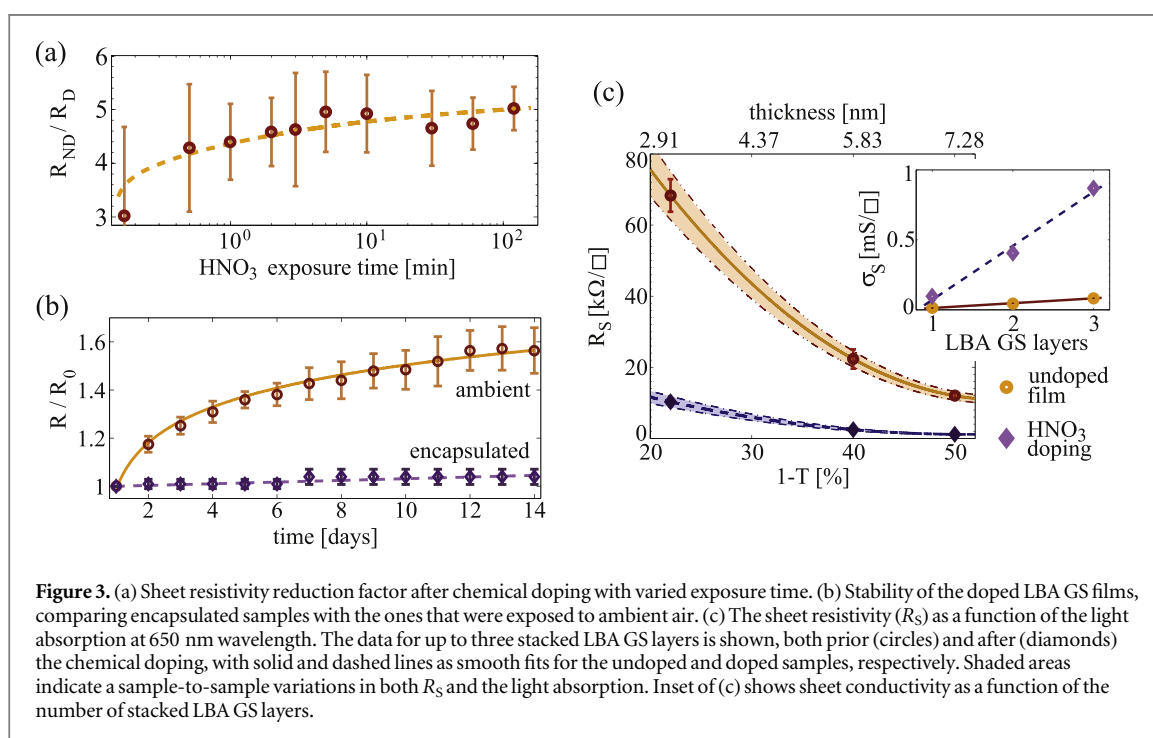
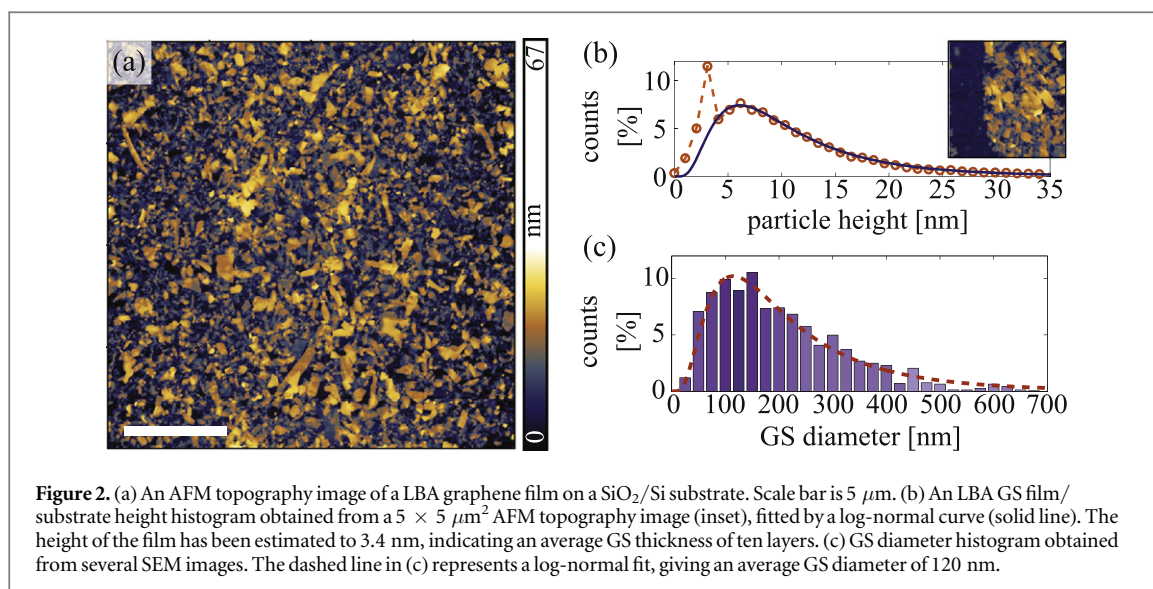
The key result of this study is doping of LBA GS films with nitric acid for improved sheet conductivity. Chemical doping of graphene can be accomplished with various liquids, vapors and polymers [10, 16, 17, 19, 28, 50–53]. One of the most efficient p-type chemical dopants of graphite and graphene is nitric acid [19, 28, 52, 54, 55]. Nitric acid has been used to chemically dope CVD graphene, and reduce the sheet resistivity by a factor of two to three [17, 19, 28, 50]. It was also used to chemically dope reduced GO [53]. Nitric acid doping of graphene was found to be very favorable for photovoltaic solar cells, where graphene is used as a top anode [16, 17, 50, 56]. Besides a reduction in sheet resistivity, the doping increases graphene's work function from about 4.5 to 5 eV, making these TCEs more suitable anode electrodes for various types of hybrid solar cells [17, 50, 52, 56, 57]. Recently, nitrogen-doped reduced GO and carbon have been demonstrated to show enhancement in energy storage [58, 59]. In the following sections we discuss the results of doping LBA GS films with nitric acid.

3.2 Nitric acid exposure time

In order to determine optimal conditions for chemical doping, the exposure time of a single layer LBA GS layer to nitric acid was varied between 10 s and 2 h. Figure 3(a) shows the exposure time dependent reduction factor of the sheet resistivity, obtained as the ratio of the sheet resistivity prior and after the doping ($R_{\text{ND}}/R_{\text{D}}$). Even after only 30 s of the exposure, the reduction factor greater than four was achieved, and after several minutes the reduction factor was found to saturate at (5 ± 1). In order to ensure the control over chemical doping, the exposure time of 5 min was chosen as an optimal value in this study.

3.3 Time stability of the enhanced conductivity effect

Considering that nitric acid is volatile and that dopants can be desorbed from the sample, the stability of the sheet resistivity was examined over an extended period of time. Two batches of LBA GS films were prepared,



one with the doped LBA GS surface exposed to the ambient conditions, and the other encapsulated (covered with Scotch tape) immediately after chemical doping. Figure 3(b) shows the relative change of sheet resistivity in time as $R(t)/R_0$, where R_0 stands for the initial sheet resistivity. Encapsulated samples show excellent time stability, with less than 5% change in sheet resistivity over two weeks.

3.4 Stacking of multiple LBA GS layers

The excellent adhesion of LBA GS sheets to the PET substrate allows not only for straightforward methods of chemical doping using liquids, but also for reproducible stacking of additional LBA layers. This is a very promising technique for making solution-based GRM

heterointerfaces [36], using a simple, one-step, low-cost and high-yield self-assembly process.

Figure 3(c) shows the sheet resistivity (R_S) as a function of optical transmittance of stacked LBA GS layers. After stacking, samples were exposed to nitric acid for 5 min. The lowest sheet resistivity obtained were on the order of 800 Ω/□, albeit at only 50% transmittance. The fact that subsequent doping can affect the entire film could be attributed to intercalation of nitric acid into the LBA GS stacks [28].

The sheet conductivity ($\sigma_S = 1/R_S$) of both doped and undoped samples was found to linearly depend on the number of LBA layers, as shown in the inset of figure 3(c). This indicates that appended LBA layers act as additional transport channels, and that the current is homogeneously distributed across the entire film

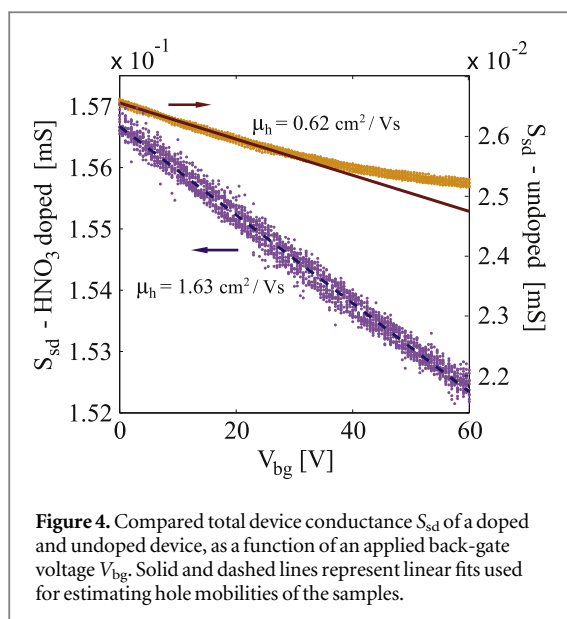


Figure 4. Compared total device conductance S_{sd} of a doped and undoped device, as a function of an applied back-gate voltage V_{bg} . Solid and dashed lines represent linear fits used for estimating hole mobilities of the samples.

when the distance between the electrodes is in the millimeter range [28].

3.5 Sheet resistivity and DC electrical characteristics measurements

The total resistance of each sample was measured in a two-point probe configuration, and the sheet resistivity was obtained by including the sample geometry factors. More details are given in supplementary information. The contact resistance was neglected being a three orders of magnitude smaller than the LBA GS film resistance. Sheet resistivity of as produced LBA GS films on PET was $(70 \pm 6) \text{ k}\Omega/\square$ for films with average thickness of 10 graphene layers. The sheet resistivity of the films after the doping was found to be reduced by the factor of five to six, reaching the value of $(12 \pm 3) \text{ k}\Omega/\square$. This change is two times larger than that reported for nitric acid doping of CVD graphene [17, 19, 28, 50]. Such a large reduction of sheet resistivity can be attributed to the fact that LPE based films have a large amount of un-functionalized GS edges, thus having more sites available for adsorption of NO_3^- and hydroxyl groups [53].

In order to characterize electrical properties of both undoped and chemically doped LBA GS films, measurements of direct-current (DC) electrical characteristics were carried out at room temperature. Device preparation, schematic representation of the measurement setups and measurements of the current between source (s) and drain (d) electrodes as a function of applied source–drain voltage V_{sd} are given in supplementary information.

Figure 4 shows the dependence of the total conductance (S_{ds}) as a function of back gate voltage (V_{bg}) for several consequent sweeps between 0 and 60 V. The negative slope of $S_{ds}(V_{bg})$ confirms that both undoped and chemically doped LBA GS films have holes as dominant charge carriers. Unintentional

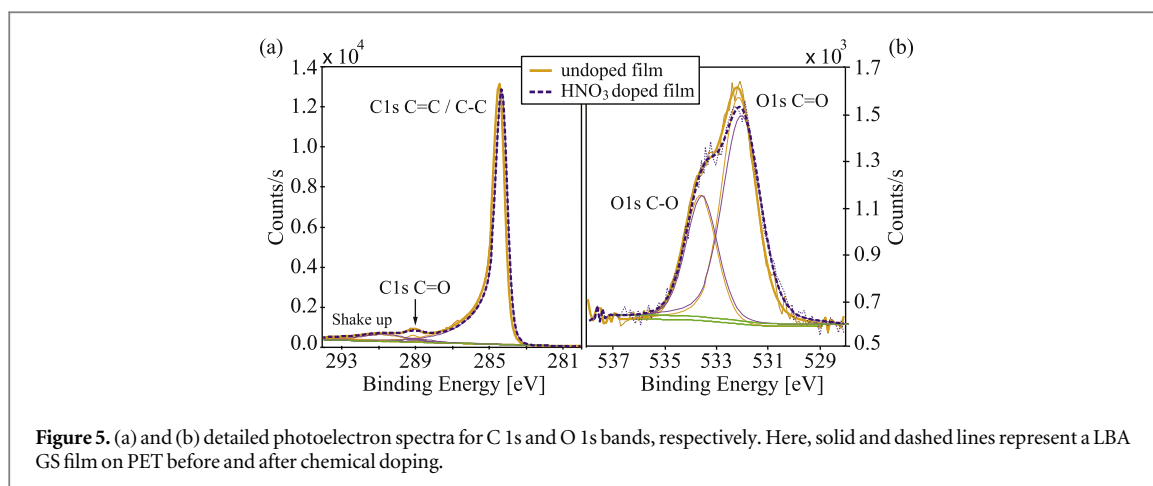
p-doping of the sample prior to the exposure to nitric acid is attributed to the remaining water and NMP residue at the interface during film transfer [32]. Conductance function was approximated to be linear, neglecting the deviation of the undoped sample at higher voltages, which is likely due to approaching a charge neutrality point. Using the linear approximation, carrier mobility has been estimated [43, 60] to be $0.6\text{--}0.8 \text{ cm}^2 \text{ V}^{-1} \text{ s}^{-1}$ for the undoped samples, and $1.55\text{--}1.75 \text{ cm}^2 \text{ V}^{-1} \text{ s}^{-1}$ for the samples that were exposed to nitric acid.

3.6 X-ray photoelectron spectroscopy (XPS)

XPS was used to elucidate the mechanisms behind the doping of graphene with HNO_3 . Measurements were carried out on a Thermo Scientific Theta Probe XPS system, providing the quantitative elemental analysis. The samples were not encapsulated, and the measurements were carried out at room temperature without *in situ* heating. In addition, angle resolved XPS was used to obtain qualitative information of elemental distribution along the depth of the samples. Experimental details are given in supplementary information. XPS indicated the presence of carbon, oxygen, and nitrogen in the sample (see supplementary information figure S2). Nitrogen 1s core level intensities of undoped LBA GS film on PET imply nitrogen concentrations of ~ 0.5 at%, which is an indication of intrinsic film doping by residual NMP [32].

Figures 5(a) and (b) show C 1s and O 1s core-level XPS spectra of the pristine and HNO_3 -treated graphene films deposited on PET. In figure 5(a) the C 1s band is deconvoluted to reveal peaks corresponding to binding energies of graphene (sp^2)/C–C bonds (284.4 eV), as well as the C–O (288.6 eV) and C=O bonds (289.1 eV). The origin of a small C=O peak in the pristine graphene/PET sample may be from photoelectrons ejected from the PET substrate or from the water molecules trapped between the flakes in the film.

In figure 5(b), the O 1s band peak has been deconvoluted to reveal the C–O (533.6 eV) and C=O (532 eV) bonds. In both C 1s and O 1s bands the chemical modification by HNO_3 is evident through the change in the intensity of C=O peaks. This change is small (oxygen content is reduced from 7.3 to 5.9 at%) and can not solely account for the change in conductivity of graphene films after the treatment with nitric acid. The relative depth plot (see supplementary information figure S3) reveals the change in the elemental distribution across the graphene layer. In pristine graphene films, oxygen atoms are mostly placed closer to the surface layer, while in the acid-treated films the situation is reversed. This can be an indication of the rearrangement in the LBA graphene films on the substrate, with oxygen bonds established between the edges of the graphene flakes deeper in the film. This result is in accordance with the reduction of



the relative intensity of the D- and G-modes in our Raman spectra, corresponding to the GS edges.

The amount of nitrogen in acid-treated films increased from 0.5 to 1 at%. The nature of the measurements could potentially diminish in a small fraction the amount of nitrogen present in the sample. However, the samples were not heated and the nitrogen is incorporated within the film, therefore the change in at% of nitrogen that could arise from these measurements is neglected. In the high-resolution spectrum of N 1s band (see supplementary information figure S3), there is no evidence of the shift in binding energy corresponding to N–O or N–C chemical bonding. Its binding energy (399.8 eV) corresponds to previously reported conjugated nitrogen which does not belong to the graphene molecule [61].

XPS analysis indicates that nitrogen is not incorporated in the honeycomb lattice structure as this would result in n-doping of graphene [51]. The $\text{C}=\text{O}^-$, $\text{C}(\text{O})\text{OH}^-$, and NO_3^- bonds are changing the carbon atoms hybridization and possibly allowing for the creation of edge-plane like catalytic sites in graphene [52, 62]. Which one of these chemical moieties is the most important factor contributing to the improved conductivity of HNO_3 -treated graphene is not clear.

3.7 Transmittance measurements

The effect of chemical doping on optical properties of LBA GS films was investigated with measurements of optical transmittance, using a spectroscopic ellipsometer in photometric mode (SOPRA GES5E IRSE). Figure 6(a) shows the transmittance of a LBA GS film in the visible and UV ranges on quartz. In the UV, the transmittance of graphene is dominated by an exciton-shifted van Hove peak in absorption [63–65]. For this reason the measured data was fitted with a Fano resonant function [65, 66]. Average transmittance of a single LBA GS film at a wavelength of 650 nm was $(78 \pm 4)\%$. Considering that each layer of graphene absorbs 2.3% of incident light in the visible part of the spectrum [67] and has a thickness of 0.335 nm, the

average film thickness indicated by transmittance measurements is (3.2 ± 0.6) nm, in agreement with AFM measurements.

The transmittance of the doped film at the same wavelength is 74%, which is within the experimental error and the variation between individual samples (figure 6(a), shaded area). While the transmittance decreased only slightly with chemical doping, the sheet resistivity of this sample decreased by a factor of ~ 4.5 .

3.8 Raman spectroscopy

Raman spectra of LBA GS films prior to and after nitric acid doping were also investigated. Room temperature measurements of Raman spectra were obtained using a TriVista 557 S&I GmbH Raman spectrometer ($\lambda = 532$ nm). Figure 6(b) shows Raman spectra of a LBA GS film on a glass substrate prior to (solid line) and after (dashed line) chemical doping, compared with graphite powder (dotted-line) before the LPE process. Analogous results were obtained for films on a PET substrate (see supplementary information), however in this case Raman spectra is dominated by PET modes. No significant shifts of any characteristic Raman modes of graphene (graphite) were detected after chemical doping. The only notable change of the Raman spectra due to chemical doping was the reduction of a $I(\text{D})/I(\text{G})$ relative intensity by 25% (see figure 6(b) inset). The relative intensity $I(\text{D})/I(\text{G})$ is indicative of the amount of GS edge scattering [68], hence our results point to a weakening of edge effects in doped films.

3.9 Work function measurements

The work function of a surface holds important information about the electronic structure. Using Kelvin probe force microscopy (KPFM, NTEGRA Spectra), we measured the work function of LBA GS films prior to and after chemical treatment, using the tabulated value of the work function for highly ordered pyrolytic graphite (HOPG) [69, 70] as a reference for

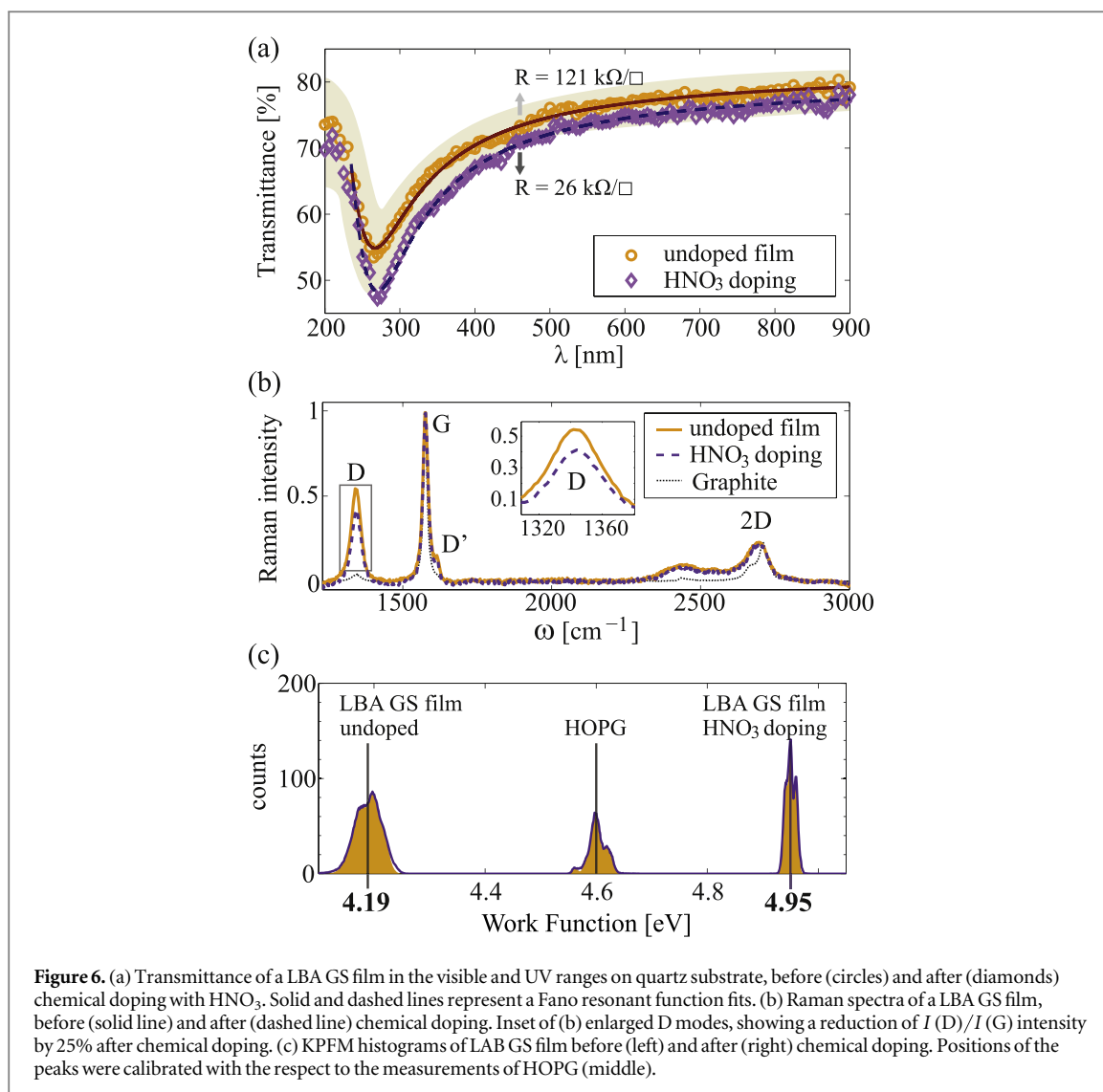


Figure 6. (a) Transmittance of a LBA GS film in the visible and UV ranges on quartz substrate, before (circles) and after (diamonds) chemical doping with HNO₃. Solid and dashed lines represent a Fano resonant function fits. (b) Raman spectra of a LBA GS film, before (solid line) and after (dashed line) chemical doping. Inset of (b) enlarged D modes, showing a reduction of $I(D)/I(G)$ intensity by 25% after chemical doping. (c) KPFM histograms of LAB GS film before (left) and after (right) chemical doping. Positions of the peaks were calibrated with the respect to the measurements of HOPG (middle).

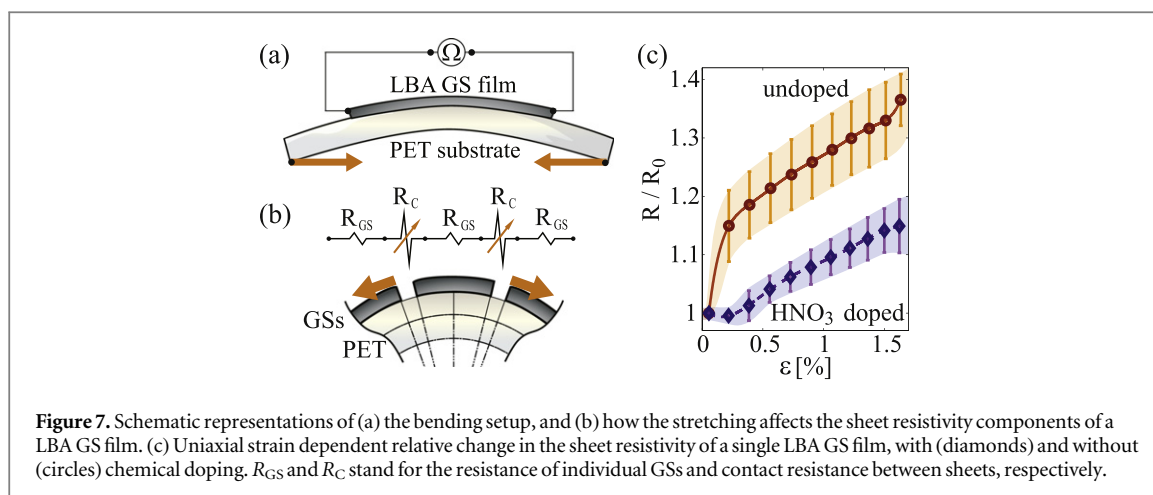
calibrating the AFM tip (details in supplementary information).

As a result, the work function values of (4.19 ± 0.05) eV and (4.95 ± 0.05) eV were obtained for the LBA GS films prior and after chemical doping, respectively. The results are presented in figure 6(c). Undoped films have much lower work function than HOPG, which is expected due to the presence of a large number of GS edges. Furthermore, this confirms that GSs are not functionalized, since in the case of reduced GO or surfactant assisted LPE much higher work functions of the resulting films are obtained [71].

Chemical doping with nitric acid increases the work function by as much as 0.75 eV, a 50% larger increase than in the case of a similar treatment of CVD graphene [17, 50]. An increase of the work function confirms that electrons migrate from GSs [72], resulting in further p-doping and a decrease of the Fermi level with the respect to Dirac point. Adsorption of NO₃⁻ groups at the sheet edges is also expected to strongly contribute to the increase of the work function.

3.10 Dependence of the sheet resistivity upon axial strain

In addition to chemical doping, the change of the sheet resistivity of LBA GS films on PET substrates was investigated under various bending conditions. The curvature of the substrate was controlled by a micrometer screw in steps of 150 μm , as schematically presented in figure 7(a). The amount of bending is expressed as an axial strain (ϵ) that LBA GS films suffer at the surface of a PET substrate upon bending. Bending radii down to 6 mm were used, giving values of axial strain up to 1.6%. Stretched LBA GS films have shown an increase in the sheet resistivity, significantly larger than in the CVD graphene [9]. Upon axial strain of about 1.5% LBA GS films on PET substrate show an increase of sheet resistivity by as much as 50%. Furthermore, Raman spectra of strained films (given in supplementary information figure S5) did not show any detectable shifts of graphene modes. This indicates that individual GSs are not exhibiting a significant amount of strain. The change in sheet resistivity is attributed to increased separation between individual



GSs, which increases the contact resistance between them, as schematically presented in figure 7(b). The relative change in sheet resistivity upon bending reaches 20% larger values in undoped films, as presented in figure 7(c). A large change of resistance upon axial strain opens up a possibility to use LBA GS films in sensing applications as strain gauges, pressure sensors, touch screens or e-skin [73].

Chemically doped samples show a significantly different change in sheet resistivity under small axial strain. For bending radii greater than 30 mm (axial strain less than 0.3%) chemically doped samples show a negligible change in the sheet resistivity. On the other hand, undoped samples show more than 10% change for the same bending conditions. Axial strain of 0.3% would correspond to the separation between individual sheets of 0.36 nm when an averaged sheet diameter of 120 nm is considered. Interestingly, this is well matched with a thermochemical radii of NO_3^- anions. This indicates that NO_3^- groups attached at the edges of GSs provide a contact between the sheets until a high enough axial strain is reached. Afterwards, the sheet resistivity of the doped samples follow a similar trend as the undoped ones. This opens up a possibility to use chemically doped LBA GS films for flexible TCEs, in the cases when small bending radii are not required.

4 Conclusion

In summary, we have shown how the LBA of multi-layer GSs produced from the dispersion in NMP and transferred on PET can be used to fabricate transparent and conductive films. An excellent adhesion of these films on PET enables for a straightforward chemical doping and stacking of multiple layers. In particular, p-type chemical doping with nitric acid has been used to reduce sheet resistivity and increase work function of these films, thus making them a more suitable low-cost alternative to CVD graphene for various TCE applications.

The sheet resistivity of deposited LBA GS layers on PET was found to be (70 ± 6) $k\Omega/\square$ with the transmittance of 78% at 650 nm wavelength. Upon a short exposure to nitric acid, sheet resistivity was reduced 5–6 fold, reaching the value of (12 ± 3) $k\Omega/\square$ with a minor reduction of the visible light transmittance. An increase of the LBA GS film work function by 0.75 eV was found upon chemical doping, yielding a value of 4.95 eV for the doped films. The work function measurements and the dependence of the sheet resistivity upon axial strain both indicate that a large reduction of the sheet resistivity occurs due to adsorption of NO_3^- groups at the edges of GSs. This reduces a contact resistance between the sheets, in addition to an increase of carrier concentration within the sheets.

Acknowledgments

This work is supported by the Serbian MPNTR through Projects ON 171005, III 45018, 451-03-2802-IP/1/167, by Qatar National Research Foundation through Project NPRP 7-665-1-125, and from the proof-of-concept project from the Office of Research and Graduate Studies of TAMUQ.

References

- [1] Novoselov K S, Falco V I, Colombo L, Gellert P R, Schwab M G and Kim K 2012 *Nature* **490** 192–200
- [2] Ferrari A C et al 2014 *Nanoscale* **7** 4598–810
- [3] Bonaccorso F, Colombo L, Yu G, Stoller M, Tozzini V, Ferrari A C, Ruoff R S and Pellegrini V 2015 *Science* **347** 1246501
- [4] Segal M 2009 *Nat. Nanotechnol.* **4** 612–4
- [5] Park S and Ruoff R S 2009 *Nat. Nanotechnol.* **4** 217–24
- [6] Britnell L et al 2013 *Science* **340** 1311–4
- [7] Bonaccorso F, Lombardo A, Hasan T, Sun Z, Colombo L and Ferrari A C 2012 *Mater. Today* **15** 564–89
- [8] De S and Coleman J N 2010 *ACS Nano* **4** 2713–20
- [9] Kim K S, Zhao Y, Jang H, Lee S Y, Kim J M, Kim K S, Ahn J-H, Kim P, Choi J-Y and Hong B H 2009 *Nature* **457** 706–10
- [10] Blake P et al 2008 *Nano Lett.* **8** 1704–08
- [11] Wang X, Zhi L and Mullen K 2008 *Nano Lett.* **8** 323–7
- [12] Wang H-X, Wang Q, Zhou K-G and Zhang H-L 2013 *Small* **9** 1266–83

- [13] Pang S, Hernandez Y, Feng X and Mullen K 2011 *Adv. Mater.* **23** 2779–95
- [14] Kratzer M, Bayer B C, Kidambi P R, Matković A, Gajić R, Cabrero-Vilatela A, Weatherup R S, Hofmann S and Teichert C 2015 *Appl. Phys. Lett.* **106** 103101
- [15] Chhikara M, Pavlica E, Matković A, Beltaos A, Gajić R and Bratina G 2014 *Carbon* **69** 162–8
- [16] Miao X, Tongay S, Petterson M K, Berke K, Rinzler A G, Appleton B R and Hebard A F 2012 *Nano Lett.* **12** 2745–50
- [17] Wu Y, Zhang X, Jie J, Xie C, Zhang X, Sun B, Wang Y and Gao P 2013 *J. Phys. Chem. C* **117** 11968–76
- [18] Park H, Chang S, Zhou X, Kong J, Palacios T and Gradecak S 2014 *Nano Lett.* **14** 5148–54
- [19] Bae S et al 2010 *Nat. Nanotechnol.* **5** 574–8
- [20] Wu J, Agrawal M, Becerril H A, Bao Z, Liu Z, Chen Y and Peumans P 2010 *ACS Nano* **4** 43–8
- [21] Han T-H, Lee Y, Choi M-R, Woo S-H, Bae S-H, Hong B H, Ahn J-H and Lee T-W 2012 *Nat. Photon.* **6** 105–10
- [22] Coraux J, N'Diaye A T, Busse C and Michely T 2008 *Nano Lett.* **8** 565–70
- [23] Reina A, Jia X, Ho J, Nezich D, Son H, Bulovic V, Dresselhaus M S and Kong J 2008 *Nano Lett.* **9** 30–5
- [24] Li X et al 2009 *Science* **324** 1312–4
- [25] Hao Y et al 2013 *Science* **342** 720–3
- [26] Zaretski A V and Lipomi D J 2015 *Nanoscale* **7** 9963–9
- [27] Li X, Zhu Y, Cai W, Borysiak M, Han B, Chen D, Piner R D, Colombo L and Ruoff R S 2009 *Nano Lett.* **9** 4359–63
- [28] Kasry A, Kuroda M A, Martyna G J, Tulevski G S and Bol A A 2010 *ACS Nano* **4** 3839–44
- [29] Stankovich S, Dikin D A, Dommett G H, Kohlhaas K M, Zimney E J, Stach E A, Piner R D, Nguyen S T and Ruoff R S 2006 *Nature* **442** 282–6
- [30] Stankovich S, Dikin D A, Piner R D, Kohlhaas K A, Kleinhammes A, Jia Y, Wu Y, Nguyen S T and Ruoff R S 2007 *Carbon* **45** 1558–65
- [31] Eda G, Fanchini G and Chhowalla M 2008 *Nat. Nanotechnol.* **3** 270–4
- [32] Hernandez Y et al 2008 *Nat. Nanotechnol.* **3** 563–8
- [33] Cai M, Thorpe D, Adamson D H and Schniepp H C 2012 *J. Mater. Chem.* **22** 24992–5002
- [34] Coleman J N et al 2011 *Science* **331** 568–71
- [35] Eda G, Yamaguchi H, Voiry D, Fujita T, Chen M and Chhowalla M 2011 *Nano Lett.* **11** 5111–6
- [36] Withers F et al 2014 *Nano Lett.* **14** 3987–92
- [37] Torrisi F et al 2012 *ACS Nano* **6** 2992–3006
- [38] Secor E B, Prabhurashi P L, Puntambekar K, Geier M L and Hersam M C 2013 *J. Phys. Chem. Lett.* **4** 1347–51
- [39] Del S K, Bornemann R, Bablich A, Schäfer-Eberwein H, Li J, Kowald T, Östling M, Bolivar P H and Lemme M C 2015 *2D Mater.* **2** 011003
- [40] Dikin D A, Stankovich S, Zimney E J, Piner R D, Dommett G H, Evmenenko G, Nguyen S T and Ruoff R S 2007 *Nature* **448** 457–60
- [41] Li X, Zhang G, Bai X, Sun X, Wang X, Wang E and Dai H 2008 *Nat. Nanotechnol.* **3** 538–42
- [42] Zhu Y, Cai W, Piner R D, Velamakanni A and Ruoff R S 2009 *Appl. Phys. Lett.* **95** 103104
- [43] Kim H, Mattevi C, Kim H J, Mittal A, Mkhoyan K A, Riman R E and Chhowalla M 2013 *Nanoscale* **5** 12365–74
- [44] Yang T, Yang J, Shi L, Mäder E and Zheng Q 2015 *RSC Adv.* **5** 23650–7
- [45] Biswas S and Drzal L T 2008 *Nano Lett.* **9** 167–72
- [46] Woltornist S J, Oyer A J, Carrillo J-M Y, Dobrynin A V and Adamson D H 2013 *ACS Nano* **7** 7062–6
- [47] Salvatierra R V, Domingues S H, Oliveira M M and Zarbin A J 2013 *Carbon* **57** 410–5
- [48] Geim A and Grigorieva I 2013 *Nature* **499** 419–25
- [49] Yang H, Withers F, Gebremedhn E, Lewis E, Britnell L, Felten A, Palermo V, Haigh S, Beljonne D and Casiraghi C 2014 *2D Mater.* **1** 011012
- [50] Lee S, Yeo J-S, Ji Y, Cho C, Kim D-Y, Na S-I, Lee B H and Lee T 2012 *Nanotechnology* **23** 344013
- [51] Wei D, Liu Y, Wang Y, Zhang H, Huang L and Yu G 2009 *Nano Lett.* **9** 1752–8
- [52] Das S, Sudhagar P, Ito E, Lee D-y, Nagarajan S, Lee S Y, Kang Y S and Choi W 2012 *J. Mater. Chem.* **22** 20490–7
- [53] Zheng Q, Ip W H, Lin X, Yousefi N, Yeung K K, Li Z and Kim J-K 2011 *ACS Nano* **5** 6039–51
- [54] Dresselhaus M S and Dresselhaus G 2002 *Adv. Phys.* **51** 1–86
- [55] Fillaux F, Menu S, Conard J, Fuzellier H, Parker S, Hanon A and Tomkinson J 1999 *Chem. Phys.* **242** 273–81
- [56] Lancellotti L, Bobeico E, Capasso A, Della Noce M, Dikonimos T, Lisi N and Delli Veneri P 2014 *2014 Fotonica AEIT Italian Conf. on Photonics Technologies* pp 1–3
- [57] Larsen L J, Shearer C J, Ellis A V and Shapter J G 2015 *RSC Adv.* **5** 38851–8
- [58] Wang J, Zhou M, Tan G, Chen S, Wu F, Lu J and Amine K 2015 *Nanoscale* **7** 8023–34
- [59] Xie X, Su D, Zhang J, Chen S, Mondal A K and Wang G 2015 *Nanoscale* **7** 3164–72
- [60] Liang X, Fu Z and Chou S Y 2007 *Nano Lett.* **7** 3840–4
- [61] Wu Y, Fang S and Jiang Y 1999 *Solid State Ion.* **120** 117–23
- [62] Kudin K N, Ozbas B, Schniepp H C, Prud'Homme R K, Aksay I A and Car R 2008 *Nano Lett.* **8** 36–41
- [63] Kravets V G, Grigorenko A N, Nair R R, Blake P, Anissimova S, Novoselov K S and Geim A K 2010 *Phys. Rev. B* **81** 155413
- [64] Mak K F, Shan J and Heinz T F 2011 *Phys. Rev. Lett.* **106** 046401
- [65] Chae D-H, Utikal T, Weisenburger S, Giessen H, Klitzing K v, Lippitz M and Smet J 2011 *Nano Lett.* **11** 1379–82
- [66] Matković A, Beltaos A, Milićević M, Ralević U, Vasić B, Jovanović D and Gajić R 2012 *J. Appl. Phys.* **112** 123523
- [67] Nair R R, Blake P, Grigorenko A N, Novoselov K S, Booth T J, Stauber T, Peres N M R and Geim A K 2008 *Science* **320** 1308
- [68] Khan U, O'Neill A, Lotya M, De S and Coleman J N 2010 *Small* **6** 864–71
- [69] Yu Y-J, Zhao Y, Ryu S, Brus L E, Kim K S and Kim P 2009 *Nano Lett.* **9** 3430–4
- [70] Takahashi T, Tokailin H and Sagawa T 1985 *Phys. Rev. B* **32** 8317
- [71] Bausi F, Schlierf A, Treossi E, Schwab M G, Palermo V and Cacialli F 2015 *Org. Electron.* **18** 53–60
- [72] Giovannetti G, Khomyakov P A, Brocks G, Karpan V M, van den Brink J and Kelly P J 2008 *Phys. Rev. Lett.* **101** 026803
- [73] Zang Y, Zhang F, Di C-a and Zhu D 2015 *Mater. Horiz.* **2** 140–56

Supplementary information

Aleksandar Matković¹, Ivana Milošević¹, Marijana Milićević¹, Tijana Tomašević-Ilić¹, Jelena Pešić¹, Milenko Musić¹, Marko Spasenović¹, Djordje Jovanović¹, Borislav Vasić¹, Christopher Deeks², Radmila Panajotović¹, Milivoj R. Belić³, and Radoš Gajić¹

¹ Center for Solid State Physics and New Materials, Institute of Physics, University of Belgrade, Pregrevica 118, 11080 Belgrade, Serbia

² Thermo Fisher Scientific, Unit 24, The Birches Industrial Estate, East Grinstead, RH19 1UB, UK.

³ Texas A&M University at Qatar, P.O. Box 23874 Doha, Qatar

E-mail: amatkovic@ipb.ac.rs

1. Direct Current Electrical Characteristics

Direct current (DC) electrical characteristic measurements were used to confirm the type of majority carriers and to estimate carrier mobility. The results are shown in Fig. 3 of the main text. Here are presented the details regarding device fabrication, measurements setup and confirmation of Ohmic contacts with gold electrodes.

In order to measure DC electrical characteristics, LBA GS films were deposited on a highly doped (0.001-0.01 Ω/cm) silicon wafer with a 300 nm thick SiO_2 layer. The substrates had pre defined gold electrodes with $\sim 150 \mu\text{m}$ channel length and $\sim 700 \mu\text{m}$ channel width, made by a shadow mask. LBA GS films were deposited in the same manner as described in the main text. It is worth mentioning that due to much lower adhesion between LBA GS film and SiO_2 surface compared with PET substrates, majority of the films are either washed out by the acid, or exhibited holes and cracks on the surface. Only films that had no visible damage (inspected under optical microscope) after chemical doping have been used in DC electrical characterization.

Figure S1(a) shows a schematic representation of the setup used for the measurements of total source-drain conductance (S_{sd}) as a function of back gate voltage (V_{bg}). $S_{sd}(V_{bg})$ measurements are given in Fig. 3 in the main text. A schematic representation of the setup used for the measurements of $I_{sd}(V_{sd})$ is shown in figure S1(b), and the I-V function for the undoped film is shown in figure S1(c). The linear dependence of $I_{sd}(V_{sd})$ confirms that contacts between the LBA GS layer and underlying gold electrodes are Ohmic.

Figure S1(d) shows a top view schematic representation of the sample geometry used for two-point probe resistivity measurements. Gold pads were defined by a shadow

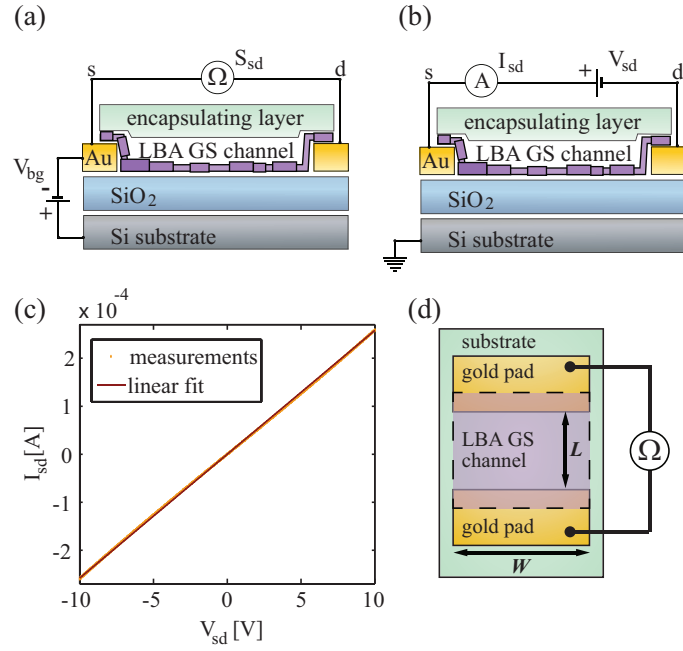


Figure S1. (a) and (b) schematic representations of the setups used for measuring $S_{sd}(V_{bg})$ and $I_{sd}(V_{sd})$, respectively. (c) The dependence of $I_{sd}(V_{sd})$ for an undoped LBA GS layer. (d) A top view schematic representation of the sample geometry used for two-point probe resistivity measurements. L and W stand for LBA GS channel length and width, respectively.

mask. The sheet resistivity was obtained by including the sample geometry factors L and W as: $\rho = R \cdot W/L$.

2. X-ray photoelectron spectroscopy

X-ray photoelectron spectroscopy (XPS) has been used to obtain elemental and chemical information of LBA GS films deposited on PET. High resolution scans of carbon 1s and oxygen 1s peaks are shown in Fig. 4 of the main text. Here, survey scans, high resolution scans of nitrogen 1s peak, relative depth plots, and the details regarding the estimate of residual NMP wt% in LBA GS films are given.

Figure S2(a,b) shows a survey scans of undoped and HNO_3 -treated LBA GS films on PET, respectively. Survey scans were obtained with a spot size of $400 \mu\text{m}$, thus averaging over a large amount of GSs. Using 1s core level intensities, atomic% of each detected element is calculated. The results are shown in a tabular insets of figure S2. Using angle resolved XPS (ARXPS) silicon was detected as a surface contamination. Considering that the LBA GS layer is 3-4 nm thick, the XPS spectra will have contributions both from the graphene layer and from the underlying PET substrate.

Figure S3(a,b) shows high resolution scans of nitrogen 1s peaks for undoped and HNO_3 -treated LBA GS films on PET. These spectra indicate that nitrogen is mostly present in a conjugated $\text{C}=\text{N}$ bond at the edges of GSs [1].

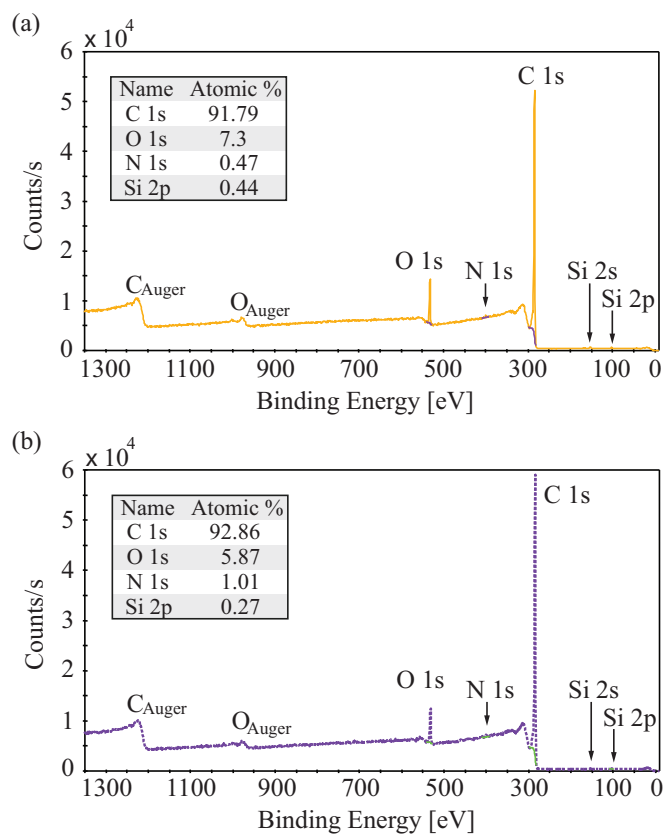


Figure S2. (a) and (b) survey scans of a LBA GS film on PET substrate prior and after chemical doping, respectively. Inset tables show atomic% of all elements detected in the scans.

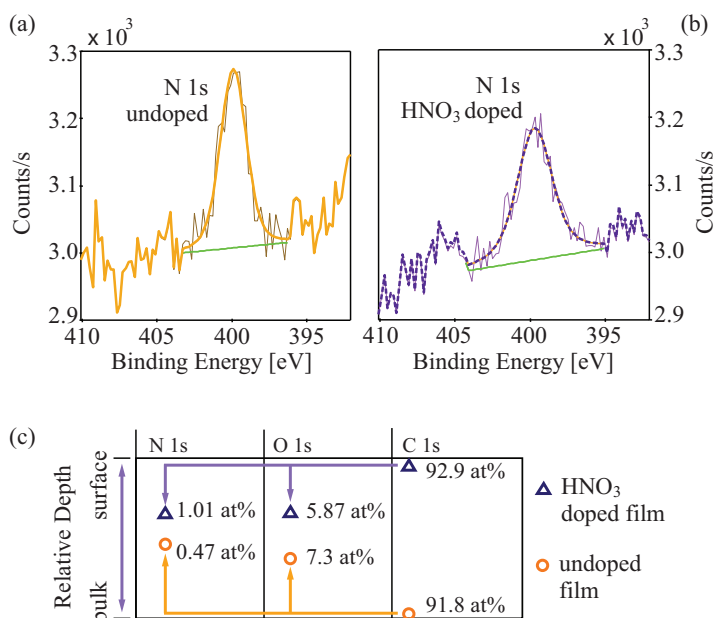


Figure S3. (a) and (b) high resolution scans of nitrogen 1s peak for undoped and HNO₃-treated LBA GS films on PET. (c) Relative depth plot obtained using ARXPS for undoped (circles) and chemically doped (triangles) LBA GS films on PET. Each point also indicates atomic% (at%) for that particular element in the sample.

ARXPS has been employed to obtain qualitative information on the depth ordering of the elements in LBA GS films prior and after chemical doping. ARXPS measurements were carried out under 16 separate angles between 20° and 80° by measuring high resolution spectra for each element with a $400\ \mu\text{m}$ spot. As a result relative depth plots are obtained. A comparison between relative depth plots of undoped (circles) and HNO_3 -treated (triangles) LBA GS films on PET is shown in figure S3(c). Each point in figure S3(c) represents an average depth of that particular species in the sample. Position of a C1s peak is associated with the position of a LBA GS layer. Relative positions of N1s and O1s peaks can then indicate where is the majority of nitrogen and oxygen atoms located in comparison with LBA GS layer. Interestingly, ARXPS suggests that prior to chemical doping both nitrogen and oxygen atoms are on average mostly located on the top of LBA GS layer, and after the doping both species are located under LBA GS layer. This implies a rearrangement of the LBA GS film upon exposure to nitric acid, as described in the main text.

3. KPFM Maps and Data Analysis

Kelvin probe force microscopy (KPFM) has been used to measure the work functions of LBA GS films prior and after chemical doping with nitric acid. The results are given in Fig. 5(c) of the main text. Here the details regarding the measurements, map analysis and the method used for obtaining the work functions are presented.

KPFM measurements were done using the two-pass technique [2, 3]. In the first pass, a topographic line was measured in the tapping mode. Figure S4(a) shows a typical $5 \times 5\ \mu\text{m}^2$ LBA GS film topography measured with 256×256 points. In the second pass, the tip was lifted by 30 nm and moved across the surface following the topographic profile, obtained from the first scan. During the second pass, a combination of an AC and DC voltage was applied between the tip and the sample. The frequency of the AC voltage was matched to the resonant frequency of the cantilever. The DC component was then adjusted to cancel an electrostatic force between the tip and the sample, resulting with a zero amplitude of the cantilever oscillations (near its resonant frequency). This procedure was repeated for every point of a selected area of the sample. Resulting KPFM maps show the applied DC component, *i.e.* the contact potential difference (CPD) between the sample and the tip. Figure S4(b) shows corresponding KPFM map to the sample topography (figure S4(a)). In order to determine CPD of the measured surface histograms of KPFM maps were used and fitted by Gaussian lines, as shown in figure S4(c).

CPD shows the difference in the work functions of the tip and the sample. In order to obtain the work function of the measured surface, the work function of the tip must be known. This was obtained by measuring several KPFM maps of freshly cleaved highly oriented pyrolytic graphite (HOPG). Work function of HOPG was considered to be 4.6 eV [2, 4].

Afterwards, several KPFM maps of LBA GS films were measured prior and after

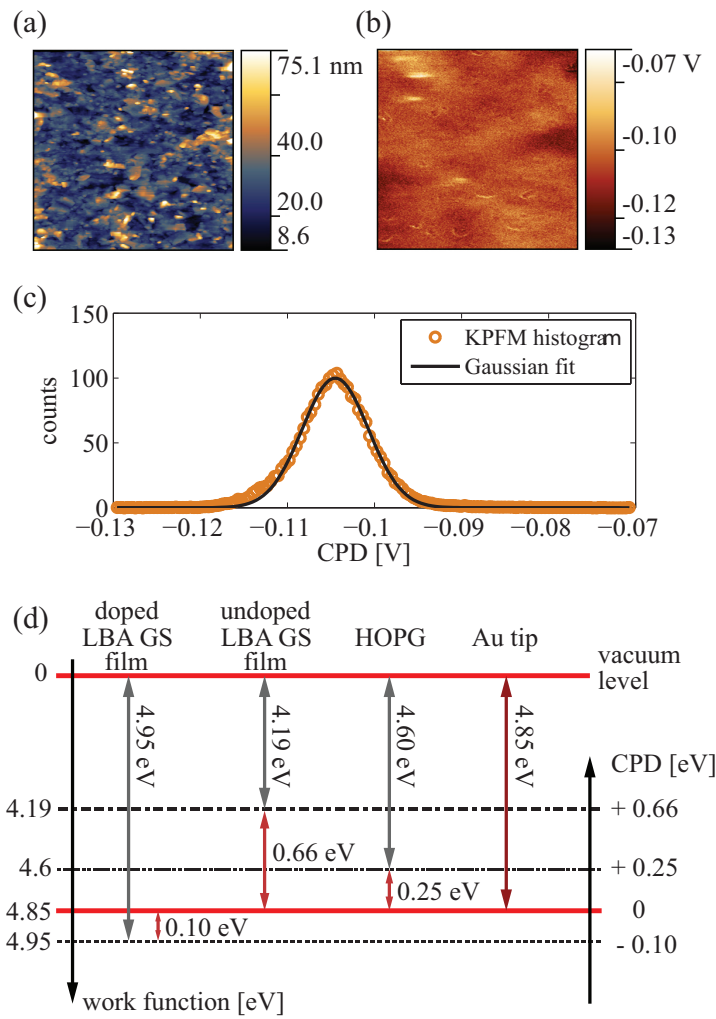


Figure S4. (a) $5 \times 5 \mu\text{m}^2$ topography image of a doped LBA GS film on PET. (b) Corresponding KPFM map of (a). (c) Histogram of (b) (circles) and Gaussian fit (solid line). (d) Schematic representation of the relation between measured CPDs and their corresponding work functions.

chemical doping. All of the obtained CPD histograms for each surface were added up, and an average CPD value was obtained from Gaussian fits as an average of the peak positions weighted by the height of the peaks. The work functions were related to their corresponding CPD measurements as illustrated by a diagram in figure S4(d).

4. Raman measurements of LBA GS films on PET

Raman spectra of LBA GS films on PET substrate prior (solid line) and after (dashed line) chemical doping are shown in figure S5(a), and are compared with a clean PET substrate (dotted line). Most of the observed Raman modes belong to PET. The only two detected modes of the LBA GS film in the measured spectral range are D ($\sim 1350\text{cm}^{-1}$) and G ($\sim 1580\text{cm}^{-1}$) modes of graphene (graphite), also shown in figure S5(b) and (c), respectively. Due to the low intensity from LBA GS layer, compared

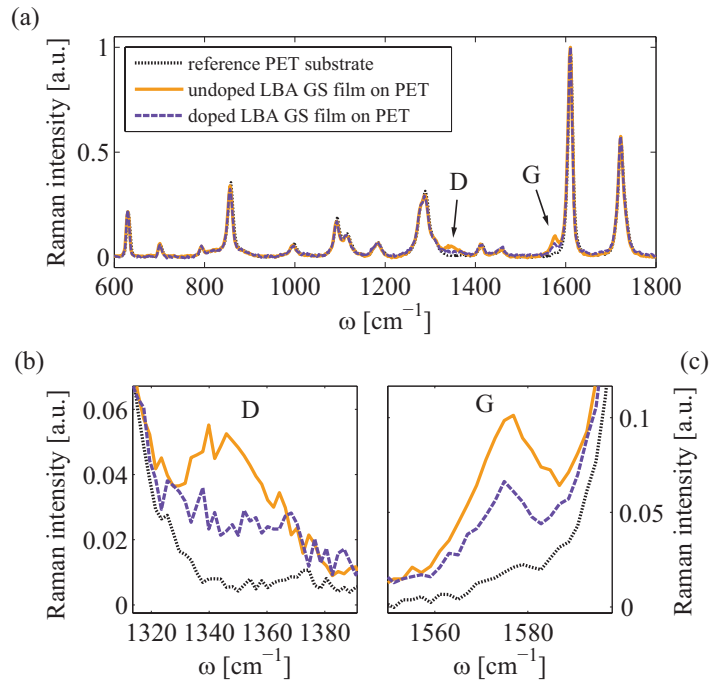


Figure S5. (a) Raman spectra of a single LBA GS film on a PET substrate, before (solid line) and after (dashed line) chemical doping, compared with a clean PET substrate (dotted line). (b) and (c) enlarged regions of graphene D and G modes, respectively.

to Raman intensity from PET substrate, graphite's 2D mode was barely resolved on PET. Relative intensity $I(D)/I(G)$ of both undoped and HNO₃-treated LBA GS films on PET are in agreement with the data obtained for the samples on glass substrates (figure 4(b) in the main text).

Additionally, no notable changes in any Raman modes of PET were detected after exposure of the sample to nitric acid. This indicates that nitric acid does not affect underlying PET substrate.

Raman spectra of LBA GS films under various bending conditions have also been examined. Figure S6(a) shows Raman spectra of a single LBA GS film on PET substrate upon axial strain of 0 % (solid line), 1.5 % (dashed line) and 3 % (dot-dashed line). Figure S6(b) shows enlarged region of G mode. Resistance of the samples was monitored during the measurements of Raman spectra. Sheet resistivity increased by ~50 % under axial strain of 1.5 %, and ~100 % under axial strain of 3 %. However, as can be seen from Raman spectra in figure S6 individual sheet do not exhibit axial strain, since there is no detectable shifts or broadenings of the G mode [5, 6].

References

- [1] Y. Wu, S. Fang and Y. Jiang, *Solid State Ionics*, 1999, **120**, 117–123
- [2] Y.-J. Yu, Y. Zhao, S. Ryu, L. E. Brus, K. S. Kim and P. Kim, *Nano Letters*, 2009, **9**, 3430–3434

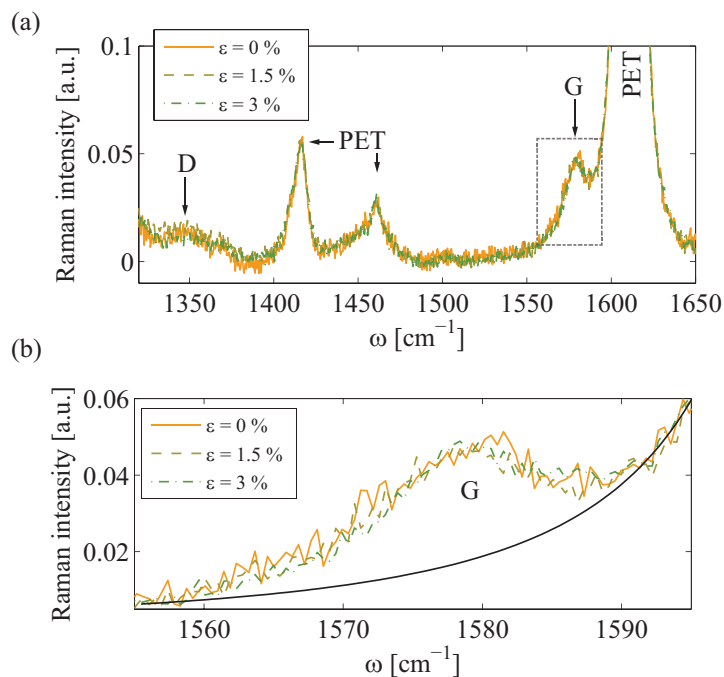


Figure S6. (a) Raman spectra of a single LBA GS film on a PET substrate upon axial strain of 0 % (solid line), 1.5 % (dashed line) and 3 % (dot-dashed line). (b) enlarged area of G mode.

- [3] A. Matković, M. Chhikara, M. Milićević, U. Ralević, B. Vasić, D. Jovanović, M. R. Belić, G. Bratina and R. Gajić, *Journal of Applied Physics*, 2015, **117**, 015305
- [4] T. Takahashi, H. Tokailin and T. Sagawa, *Physical Review B*, 1985, **32**, 8317
- [5] T. Mohiuddin, A. Lombardo, R. Nair, A. Bonetti, G. Savini, R. Jalil, N. Bonini, D. Basko, C. Galotis, N. Marzari *et al.*, *Physical Review B*, 2009, **79**, 205433
- [6] F. Ding, H. Ji, Y. Chen, A. Herklotz, K. Dorr, Y. Mei, A. Rastelli and O. G. Schmidt, *Nano Letters*, 2010, **10**, 3453–3458

Transparent and conductive films from liquid phase exfoliated graphene

Tijana Tomašević-Ilić¹ · Jelena Pešić¹ · Ivana Milošević¹ ·
Jasna Vujin¹ · Aleksandar Matković¹ · Marko Spasenović¹ ·
Radoš Gajić¹

Received: 5 November 2015 / Accepted: 6 May 2016 / Published online: 14 May 2016
© Springer Science+Business Media New York 2016

Abstract We describe transparent and conductive films of liquid-phase exfoliated graphene deposited with the Langmuir–Blodgett (LB) method. Graphene sheets (GS) were exfoliated from graphite by ultrasonic treatment in N-Methyl-2-pyrrolidone (NMP) and N, N-dimethylacetamide (DMA) solvents. For comparison, graphene sheets were also exfoliated in a water solution of surfactants. We confirm a higher exfoliation rate for surfactant-based processing compared to NMP and DMA. Furthermore, we demonstrate that our films exfoliated in NMP and DMA, deposited with LB and annealed have a higher optical transmittance and lower sheet resistance compared to films obtained with vacuum filtration, which is a necessary step for GS exfoliated in water solutions. The structural, optical and electrical properties of graphene layers were characterized with scanning electron microscopy, atomic force microscopy, UV/VIS spectrophotometry and sheet resistance measurements. Our facile and reproducible method results in high-quality transparent conductive films with potential applications in flexible and printed electronics and coating technology.

Keywords Graphene · LPE · Langmuir–Blodgett assembly

1 Introduction

Transparent conductors are an essential part of many optical devices. Many of the thin metallic or metal oxide films used as transparent conductors (Granqvist 2007) exhibit nonuniform absorption across the visible spectrum (Phillips et al. 1994), or they are

This article is part of the Topical Collection on Advances in the Science of Light.

Guest Edited by Jelena Radovanovic, Milutin Stepic, Mikhail Sumetsky, Mauro Pereira and Dragan Indjin.

✉ Tijana Tomašević-Ilić
ttijana@ipb.ac.rs

¹ Center for Solid State Physics and New Materials, Institute of Physics, University of Belgrade, Pregrevice 118, 11080 Belgrade, Serbia

chemically unstable, or both (Scott et al. 1996; Schlatmann et al. 1996). The experimental discovery of graphene (Novoselov et al. 2004) brought a new alternative to this field. Graphene is a material with high optical transparency, large carrier mobility, good chemical stability, and mechanical strength, making it an excellent choice for transparent electrodes in various optoelectronic devices (Blake et al. 2008).

Although graphene is a natural choice for transparent conductive films (Bonaccorso et al. 2010), the feasibility of its mass production is essential for applications. In order to produce large quantities of graphene Blake et al. (Blake et al. 2008) and Hernandez et al. (2008) developed a method of graphene production using solvent assisted exfoliation (or liquid phase exfoliation, LPE) of bulk graphite, which is simpler and less costly than chemical vapor deposition and returns a higher yield than mechanical exfoliation (Novoselov et al. 2004, 2005). LPE allows the possibility to scale up the synthesis of graphene making it economically available in a large amount, presenting a promising route for large-scale production (Paton et al. 2014).

Numerous research efforts followed up to increase the concentration and quality of the graphene flakes produced. One of the most promising synthesis routes for LPE graphene is non-covalent exfoliation using solvents that have surface energy values comparable to that of graphite (Hernandez et al. 2008). Typically ultrasound assists the separation of graphene flakes from graphite powder in solvent. Exfoliation conditions such as the initial concentration of graphite powder, sonication time (Khan et al. 2010), solvent type (O'Neill et al. 2011; Bourlinos et al. 2009; Hernandez et al. 2010; Lotya et al. 2009; Guardia et al. 2011), and possible filtration (Khan et al. 2011) were tuned in order to optimize the yield and quality of graphene dispersions. These graphene dispersions can be used to form films by various methods, for example spray coating (Blake et al. 2008), vacuum filtration (Hernandez et al. 2008; Lotya et al. 2009) or Langmuir–Blodgett assembly (LBA) (Cote 2009; Kim et al. 2013; Li et al. 2008).

In this study, graphene sheets (GS) were exfoliated from graphite by ultrasonic treatment in organic solvents with high boiling points, N-Methyl-2-pyrrolidone (NMP), N, N-dimethylacetamide (DMA), and for comparison, in a water solution of surfactant, sodium dodecylbenzenesulfonate (SDBS) and Pluronic P-123 (P-123). The graphene dispersions from NMP and DMA were used to form films by controlled deposition of few-layer graphene using the Langmuir–Blodgett (LB) method on a water–air interface. We confirm a higher exfoliation rate for surfactant-based processing, but demonstrate that our films exfoliated in organic solvents with high boiling points and deposited with LB have a higher optical transmittance and lower sheet resistance compared to films obtained with vacuum filtration, which is a necessary step for GS exfoliated in water solutions. The structural, optical and electrical properties of graphene layers were characterized with scanning electron microscopy, atomic force microscopy, UV/VIS spectrophotometry and sheet resistance measurements.

2 Experimental procedure

All chemicals used were purchased from Sigma Aldrich: graphite powder (product number 332461), N-Methyl-2-pyrrolidone (product number 328634), N, N-dimethylacetamide (product number 38840), sodium dodecylbenzenesulfonate (product number 289957) and Pluronic P-123 (product number 435467). The particular graphite powder product was chosen for its large initial flake size, which should result in the largest possible graphene

flakes after exfoliation. Stock solutions of SDBS and P-123 of different concentrations were prepared in deionized water (resistivity 18 M Ω) by stirring overnight. A range of graphene dispersions were prepared. A typical sample was prepared by dispersing graphite in the desired solvent using from 30 min to 14 h of sonication in a low power sonic bath. The resulting dispersion was centrifuged for 60 min at 3000 rpm in order to reduce the amount of unexfoliated graphite.

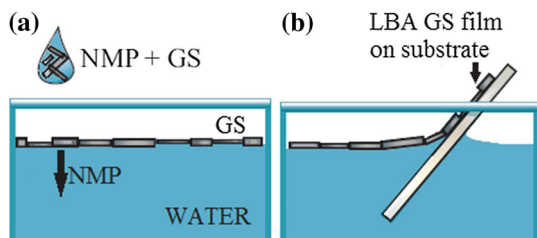
The graphene sheets exfoliated from graphite by ultrasonic treatment in NMP were used to form films at a water–air interface. Beakers filled with deionized water, 10 mL volume, were used for film formation. A 1.5–2 vol% of GS + NMP was added to the interface with a continuous flow rate of 5–10 mL/s (Fig. 1a). This set of parameters provides enough surface pressure for the film to be close-packed. After the film is formed, it is slowly scooped onto the targeted substrate (Fig. 1b), as shown in our previous work (Matković et al. 2016). PET and SiO₂/Si were used as substrates. As it has been shown that annealing decreases sheet resistance due to solvent evaporation (Hernandez et al. 2008; Lotya et al. 2009), some of these deposited films were annealed. Annealing was carried out in a tube furnace at 250 °C in an argon atmosphere for 2 h.

For optical characterization, UV–VIS spectra were taken using a SUPER SCAN Varian spectrophotometer with quartz cuvettes. The resistance of each sample was measured in a two-point probe configuration, and the sheet resistance was obtained by including the sample geometry factors. AFM measurements were taken with an atomic force microscope, NTEGRA Spectra, in tapping mode. SiO₂/Si was chosen as a substrate for AFM due to its low surface roughness. The lateral profile of graphene flakes was analyzed with a Tescan MIRA3 field-emission gun SEM.

3 Results and discussion

We optimized for high graphene concentration and large flake size, tuning exfoliation conditions such as initial graphite concentration, sonication time and solvent type. The Lambert–Beer law was applied to UV–VIS absorption spectra to find graphene concentration. The concentration was estimated from the absorbance at 660 nm by using the extinction coefficient of graphene ($\alpha = 13.90 \text{ mL mg}^{-1} \text{ m}^{-1}$) previously determined in surfactant/water solutions (Hernandez et al. 2008; Lotya et al. 2009; Guardia et al. 2011) and ($\alpha = 24.60 \text{ mL mg}^{-1} \text{ m}^{-1}$) in NMP and DMA solutions (Hernandez et al. 2008). Figure 2a depicts a higher final concentration for surfactant-based processing for all initial concentrations of graphite powder, from 0.5 to 18 mg mL⁻¹. The most commonly used deposition technique for LPE GS is vacuum filtration. This is a necessary step for GS exfoliated in water solutions. For GS films formed by evaporation of a high boiling point

Fig. 1 Schematic representations of **a** LBA GS film formation, **b** scooping of the film onto a targeted substrate



solvent, one of the biggest problems is that graphene flakes aggregate during evaporation (O'Neill et al. 2011) hindering fine control over the film thickness (Hernandez et al. 2008). This can be avoided by depositing with LB, which allows reliable and reproducible thickness control and prevents further agglomeration of graphene flakes during drying (Kim et al. 2013). We chose the dispersion in NMP with the highest graphene concentration (Fig. 2b) for experiments on LB films.

A single LB deposition resulted in films with an average thickness 3.3 nm, as measured with AFM, indicating an average GS thickness of 10 layers (Fig. 3).

Figure 4 shows optical transmittance versus sheet resistance for varying number of LB depositions on PET, compared to graphene film obtained with vacuum filtration of GS exfoliated from the same graphite precursor using the same experimental procedure (Hernandez et al. 2008; Lotya et al. 2009) before and after annealing. The highest transparency for a single LB film deposition prior to annealing was found to be about 83 %, which is between 20 and 40 % higher than the transmittance that can be accomplished with vacuum-filtration. The sheet resistance of one LB film deposition is between 70 and 250 k Ω /sq, 2–5 times lower than sheet resistance achieved with vacuum filtration without annealing. Increasing the graphene film thickness with additional LB depositions led to consistent increases in conductivity, but a decrease in transparency. Our graphene films for three LB depositions prior to annealing have comparable sheet resistance but higher optical transmittance compared to vacuum-filtered films after annealing.

The electrical conductivity is affected by the size and connectivity of the flakes as well as the thickness of the films. Our average GS diameter was is 120 nm, as measured with SEM (Fig. 5). SEM also revealed the presence of pinholes between flakes for a single LB deposition, which probably results in parasitic sheet resistance (Fig. 5a). In order to remove the residual solvent between the overlapping flakes, which may affect transport, we employed thermal annealing. Annealing does not repair the holes and other irreversible defects (Fig. 5b), but it can remove residual solvents, improving the coupling between graphene flakes and hence decreasing sheet resistance. For a single LB deposition, annealing reduced sheet resistance by about six times, without considerably decreasing transparency (Fig. 4). The sheet resistance of a singly deposited film after annealing was found to be between 10 and 20 k Ω /sq, a significant improvement over other published data. After annealing we performed a second LB deposition and achieved sheet resistance of

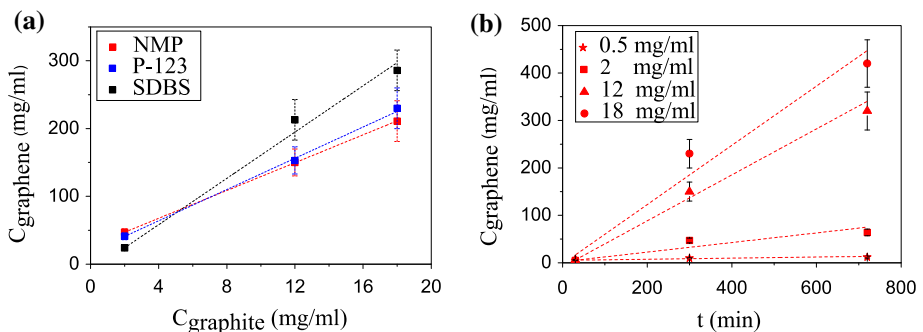


Fig. 2 Concentration of dispersed graphene: **a** in different solutions for different initial graphite concentration and sonication time of 5 h, **b** in NMP for different sonication time and different initial graphite concentration

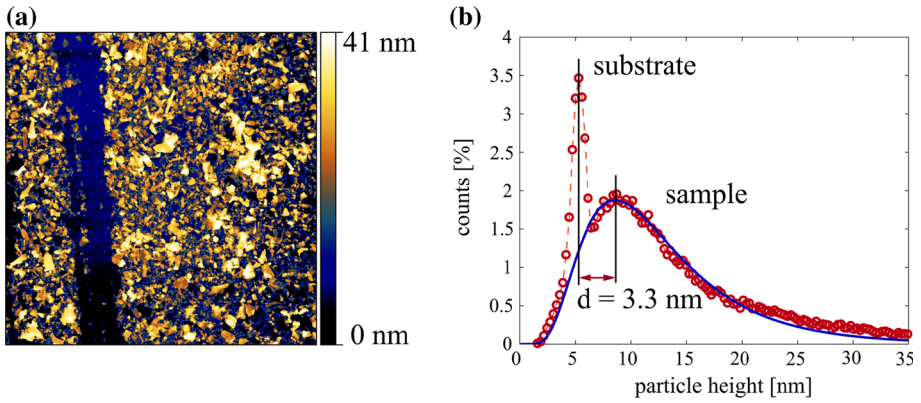


Fig. 3 **a** AFM image of a LB graphene film on a SiO₂/Si substrate, **b** an LB GS film/substrate height histogram fitted with a log-normal curve

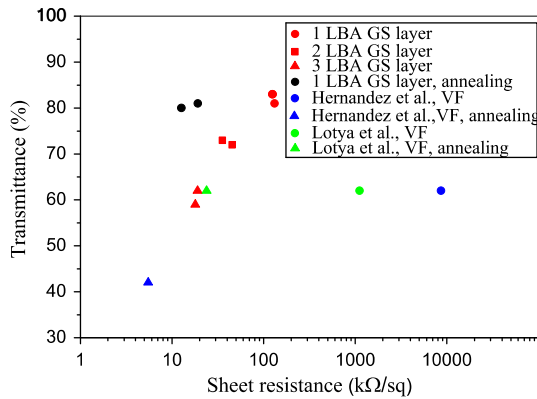


Fig. 4 Optical transmittance versus sheet resistance for varying number of LB deposition of graphene sheets on PET exfoliated in NMP before (*red*) and after annealing (*black*), compared to graphene films obtained with vacuum filtration in the same solvent (*blue*) (Hernandez et al. 2008) and graphene films obtained with vacuum filtration in surfactant/water solutions (*green*) (Lotya et al. 2009) before and after annealing. (Color figure online)

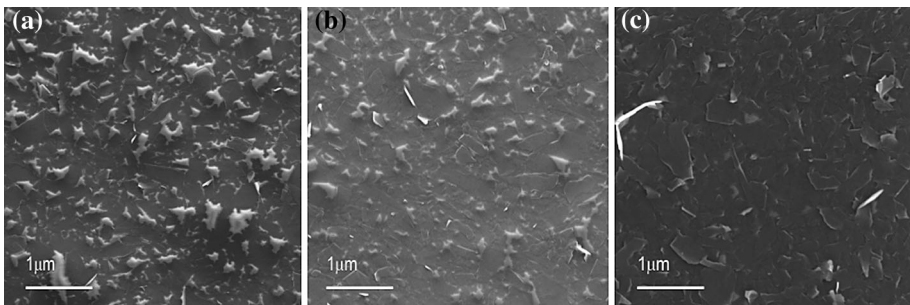


Fig. 5 SEM images of: **a** singly deposited LB film on a glass substrate, **b** the same film after annealing, **c** two LB depositions with an annealing step in between

3 k Ω /sq and a transparency of more than 70 %. Decreased resistance is the result of reduced density of pinholes (Fig. 5c) as well as increased film thickness.

4 Conclusion

In summary, we have shown that Langmuir–Blodgett assembly of multi-layer graphene sheets produced from liquid phase exfoliation of graphite powder in solvents can be used to fabricate transparent and conductive films. The sheet resistance of deposited LBA GS layers was found to be between 15 and 250 k Ω /sq, with transmittance between 60 and 85 %, depending on the number of deposited LBA graphene layers. The conductivity of these LBA films can be further increased by about six times with annealing, without considerably decreasing transparency. Optoelectronic properties of these films are much better compared to graphene films obtained with vacuum filtration of GS exfoliated with the same experimental procedure, which is the most commonly used deposition technique for LPE GS. Ours is a facile, reproducible and low-cost technique for transparent conductive films with potential applications in coating technology.

Acknowledgments This work was funded by the Serbian MPNTR through Projects OI 171005 and Innovation Project 451-03-2802-IP/1/167 and by Qatar National Research Foundation through Projects NPRP 7-665-1-125. The authors would like to express their gratitude to S. Novkovic for technical support with annealing.

References

- Blake, P., et al.: Graphene-based liquid crystal device. *Nano Lett.* **8**, 1704–1708 (2008)
- Bonaccorso, F., et al.: Graphene photonics and optoelectronics. *Nat. Photonics* **4**, 611–622 (2010)
- Bourlinos, A.B., et al.: Liquid-phase exfoliation of graphite towards solubilized graphenes. *Small* **5**, 1841–1845 (2009)
- Cote, L.J.: Langmuir–Blodgett assembly of graphite oxide single layers. *J. Am. Chem. Soc.* **131**, 1043–1049 (2009)
- Granqvist, C.G.: Transparent conductors as solar energy materials: a panoramic review. *Sol. Energy Mater. Sol. Cells* **91**, 1529–1598 (2007)
- Guardia, L., et al.: High-throughput production of pristine graphene in an aqueous dispersion assisted by non-ionic surfactants. *Carbon* **49**, 1653–1662 (2011)
- Hernandez, Y., et al.: High-yield production of graphene by liquid-phase exfoliation of graphite. *Nat. Nanotechnol.* **3**, 563–568 (2008)
- Hernandez, Y., et al.: Measurement of multicomponent solubility parameters for graphene facilitates solvent discovery. *Langmuir* **26**, 3208–3213 (2010)
- Khan, U., et al.: High-concentration solvent exfoliation of graphene. *Small* **6**, 864–871 (2010)
- Khan, U., et al.: Solvent-exfoliated graphene at extremely high concentration. *Langmuir* **27**, 9077–9082 (2011)
- Kim, H.K., et al.: Optoelectronic properties of graphene thin films deposited by a Langmuir–Blodgett assembly. *Nanoscale* **5**, 12365–12374 (2013)
- Li, X., et al.: Highly conducting graphene sheets and Langmuir–Blodgett films. *Nat. Nanotechnol.* **3**, 538–542 (2008)
- Lotya, M., et al.: Liquid phase production of graphene by exfoliation of graphite in surfactant/water solutions. *J. Am. Chem. Soc.* **131**, 3611–3620 (2009)
- Matković, A., et al.: Enhanced sheet conductivity of Langmuir-Blodgett assembled graphene thin films by chemical doping. *2D Mater.* **3**(1), 015002 (2016)
- Novoselov, K.S., et al.: Electric field effect in atomically thin carbon. *Science* **306**, 666–669 (2004)
- Novoselov, K.S., et al.: Two-dimensional atomic crystals. *Natl. Acad. Sci. U.S.A.* **102**, 10451–10453 (2005)
- O'Neill, A., et al.: Graphene dispersion and exfoliation in low boiling point solvents. *J. Phys. Chem. C* **115**, 5422–5428 (2011)

- Paton, K.R., et al.: Scalable production of large quantities of defect-free few-layer graphene by shear exfoliation in liquids. *Nat. Mater.* **13**, 624–630 (2014)
- Phillips, J.M., et al.: Transparent conducting thin films of GaInO₃. *Appl. Phys. Lett.* **65**, 115–117 (1994)
- Schlatmann, A.R., et al.: Indium contamination from the indium–tin–oxide electrode in polymer light emitting diodes. *Appl. Phys. Lett.* **69**, 1764–1766 (1996)
- Scott, J.C., et al.: Degradation and failure of MEH-PPV light-emitting diodes. *J. Appl. Phys.* **79**, 2745–2751 (1996)



OPEN

Single-step fabrication and work function engineering of Langmuir-Blodgett assembled few-layer graphene films with Li and Au salts

Ivana R. Milošević¹✉, Borislav Vasić¹, Aleksandar Matković²✉, Jasna Vujin¹, Sonja Aškrić³, Markus Kratzer², Thomas Griesser⁴, Christian Teichert² & Radoš Gajić¹

To implement large-area solution-processed graphene films in low-cost transparent conductor applications, it is necessary to have the control over the work function (WF) of the film. In this study we demonstrate a straightforward single-step chemical approach for modulating the work function of graphene films. In our approach, chemical doping of the film is introduced at the moment of its formation. The films are self-assembled from liquid-phase exfoliated few-layer graphene sheet dispersions by Langmuir-Blodgett technique at the water-air interfaces. To achieve a single-step chemical doping, metal standard solutions are introduced instead of water. Li standard solutions (LiCl, LiNO₃, Li₂CO₃) were used as n-dopant, and gold standard solution, H(AuCl₄), as p-dopant. Li based salts decrease the work function, while Au based salts increase the work function of the entire film. The maximal doping in both directions yields a significant range of around 0.7 eV for the work function modulation. In all cases when Li-based salts are introduced, electrical properties of the film deteriorate. Further, lithium nitrate (LiNO₃) was selected as the best choice for n-type doping since it provides the largest work function modulation (by 400 meV), and the least influence on the electrical properties of the film.

Graphene, consisting of a single layer carbon arranged in a hexagonal lattice, has attracted extensive interest because of the excellent mechanical and electrical properties associated with its two dimensional structure^{1–4}. Chemical vapor deposition (CVD) method has become the most common method for production of large-area graphene films⁵. Still, simple and low-cost methods are needed for mass production especially when considering the cases where high-quality films are not needed for the desired functionality, as in low-power lighting, sensors, transparent heating, and de-icing applications⁶. In that context, liquid-phase exfoliation (LPE) is a perspective way of obtaining large quantities of exfoliated graphite in solution. LPE of graphite results in a dispersion of few-layer graphene sheets (GSs) in the solvent. However, in order to access the full potential of LPE-processed graphene, thin-films needs to be controllably fabricated utilizing techniques capable to introduce self-ordering of GSs⁷. One such example is Langmuir-Blodgett assembly (LBA). Based on surface-tension induced self-assembly of nanoplatelets at the liquid-air interface or the interface of two liquids, LBA is a good method for production of large-scale, highly transparent, thin solution-processed graphene films^{8–11}.

Excellent electrical conductivity, flexibility and transparency in the visible domain make graphene a natural choice for ultrathin, flexible and transparent electrodes in electronic devices^{10,12–19}. Still, a significant work function difference between graphene and frequently employed active layers of photovoltaic and light-emitting diode (LED) devices gives rise to a high contact resistance. Contact resistance can have a significant impact on overall efficiency and performance of the devices²⁰. This is of a particular technological relevance considering that any realistic application of graphene based transparent electrode must compete against those based on indium tin

¹Laboratory for Graphene, other 2D Materials and Ordered Nanostructures of Center for Solid State Physics and New Materials, Institute of Physics, University of Belgrade, Pregrevica 118, 11080, Belgrade, Serbia. ²Institute of Physics, Montanuniversität Leoben, Franz Josef Str. 18, 8700, Leoben, Austria. ³Nanostructured Matter Laboratory of Center for Solid State Physics and New Materials, Institute of Physics, University of Belgrade, Pregrevica 118, 11080, Belgrade, Serbia. ⁴Institute of Chemistry of Polymeric Materials, Montanuniversität Leoben, Otto-Gloeckel-Strasse 2, 8700, Leoben, Austria. ✉e-mail: novovic@ipb.ac.rs; aleksandar.matkovic@unileoben.ac.at

oxide (ITO) or fluorine-doped tin oxide (FTO), which have already gone through decades of interfacial optimization in order to deliver today's performance^{21–23}. Therefore, the understanding of the efficient ways for modulation of the graphene work function is crucial for improving device performances^{21,22,24}. In order to enhance the charge injection, the work function of the graphene electrode should be optimized to better match WF of the adjacent layer in order to form an ohmic contact²⁴.

Recently, the chemical doping has been reported to be an effective method for doping of CVD graphene and tuning its work function by charge transfer between the graphene sheet and metal salts, organic dopants, or metal oxide layers^{12,14,21–28}. Such surface charge transfer induced by chemical doping is expected to efficiently control the Fermi level of graphene sheets without introducing substitutional impurities or basal plane reactions, thus, preventing any damage to the carbon networks and not introducing scattering centres that would lower carrier mobility²¹. Kwon *et al.* reported n-type chemical doping of CVD graphene with alkali metal carbonates by soaking in appropriate solutions²³ and alkali metal chlorides by spin-coating of appropriate solutions on the transferred graphene substrates²⁵. So far, doping of Langmuir-Blodgett graphene films prepared from LPE dispersions has been done with nitric acid and ozone after the film was formed using the drop-casting method and UV/ozone treatment^{9,29}. Chemical doping is especially attractive for LPE-based graphene films since many exposed edges of GSs are expected to enable very efficient functionalization through charge transfer doping. However, the chemical doping with metal salt solutions has not been used to control the work function of LBA graphene films so far. In this work LBA graphene films obtained from LPE dispersion were doped during the process of film formation. Therefore, the formation and doping of the LBA graphene films in our work represent a single-step process. This is a significant improvement compared to previous works where the chemical doping was applied only after the graphene fabrication.

In the present work, we systematically investigated single-step work function modulation (increase and decrease) of the LPE GS films achieved by chemical doping. In particular, using Li standard solutions (LiCl, LiNO₃ and Li₂CO₃) as n-dopant, and gold standard solution H(AuCl₄) as p-dopant was investigated. In contrast to previous methods for chemical doping of CVD graphene which can be applied only after the graphene films fabrication, here we described the method for the production and doping of LPE graphene films in a single-step. Single-step work function modulation means doping of the film at the moment of its formation from the LPE graphene dispersion by LBA technique at the air-metal standard solution interface. We have demonstrated tunability of the WF in the range of almost 1 eV, making these metal-salt treated LPE-based graphene electrodes suitable candidates for both electron and hole injection interfaces.

Results and discussion

Morphology of LPE GS films. Fabrication and doping of the GS films is schematically represented in Fig. 1(a): air-metal standard solution interface, introduction of LPE dispersion and formation of the LPE GS film at the interface, scooping of the doped film on the target substrate and finally, obtained doped LPE GS film which is further investigated with different techniques.

Morphology of LPE GS films is depicted in Fig. 1 consisting of both optical (Fig. 1(b1–f1)) and Atomic Force Microscopy (AFM) topographic images (Fig. 1(b2–f2)) for both undoped and metal doped LPE GS films. As can be seen from AFM images, the doping process does not change morphology of LPE films, except that the doped films contain more agglomerates (visible as bright particle-like domains). The following values for the surface roughness were obtained by AFM measurements averaged on ten 50 × 50 μm² areas: (a) 11.9 ± 1.5 nm for undoped LPE GS film, (b) 11.5 ± 3.5 nm for Li₂CO₃ doped, (c) 13.3 ± 2 nm for H(AuCl₄) doped, (d) 13.7 ± 1.6 nm for LiCl doped, and (e) 13.8 ± 1.2 nm for LiNO₃ doped LPE GS films. Therefore, the surface roughness slightly increases by around 2 nm after the doping, while for Li₂CO₃ doped LPE GS film is practically the same as for the undoped film. Still, optical images recorded on larger scale depict formation of agglomerates in doped films which could degraded their optical (leading to an increased scattering and/or absorption of incoming lights on these clusters) and electrical properties (due to enhanced scattering of charge carriers).

The observed formation of the agglomerates is most likely not an inherent property of the particular metal-salt doping. Overcoming this would likely require further optimization of the LBA process. However, as a benchmark the LBA process in this study was optimized for an undoped film and was left unchanged for all of the metal-salt doped films.

Transmittance measurements. Using the different doping metal standard solution during LBA of graphene films was found to result in different transparency. In the UV region, the transmittance of graphene is dominated by an exciton-shifted van Hove peak in absorption^{9,30}. Transmittance at 550 nm was 82% for undoped and 80%, 76%, 74%, 68% for H(AuCl₄), LiCl, LiNO₃, Li₂CO₃ doped LPE GS films, respectively (Fig. 2). It can be seen that transmittance decreases for doped LPE GS films. Metal salts decrease the transmittance of the graphene films regardless the type of the present metal (gold or lithium). The degree of the transmittance decrease was related to not only the metal cations but also the anions. Different lithium salts decrease transmittance in different amounts. Transmittance decrease of 14% was the highest for the LPE GS film doped with lithium carbonate (Li₂CO₃). Similar results of the transmittance decrease for metal doped CVD graphene films were obtained in studies of Kwon *et al.*^{22,23,25}. Transmittance decrease could be a consequence of the metal particles adsorption and agglomeration on doped films after the solvent evaporation process. Changes in the thickness of LPE GS films with doping could not be excluded because LBA process in this study was optimized for an undoped film and was left unchanged for all of the metal-salt doped films.

Raman measurements. Raman spectra for undoped and H(AuCl₄), LiCl, LiNO₃, Li₂CO₃ doped LPE GS films are given in Fig. 3(a). The four basic graphene/graphite peaks D (~1348 cm⁻¹), G (~1579 cm⁻¹), D' (1614

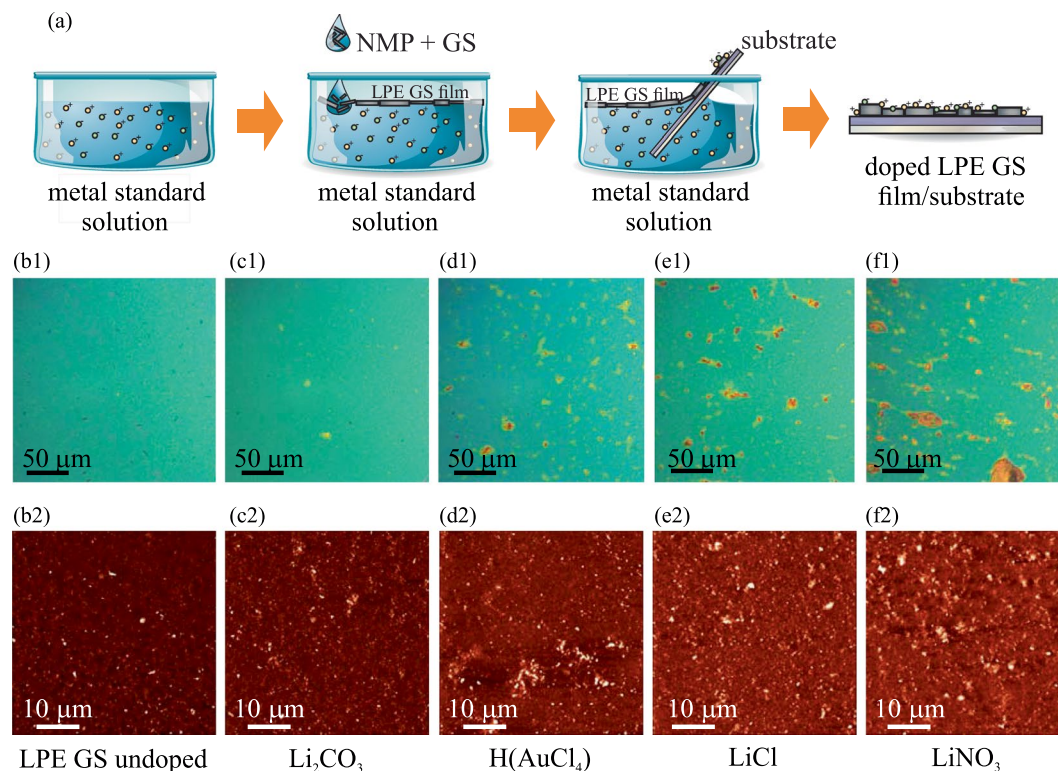


Figure 1. (a) Schematic representation of the LPE GS film formation and its doping in the single-step process. (b1–f1) Optical images are shown in the top row, whereas (b2–f2) AFM topographic images are shown in the bottom row for the following cases: (b) undoped LPE GS film, and (c) Li_2CO_3 , (d) $\text{H}(\text{AuCl}_4)$, (e) LiCl , (f) LiNO_3 doped LPE GS films. z-scale in all AFM images is 100 nm.

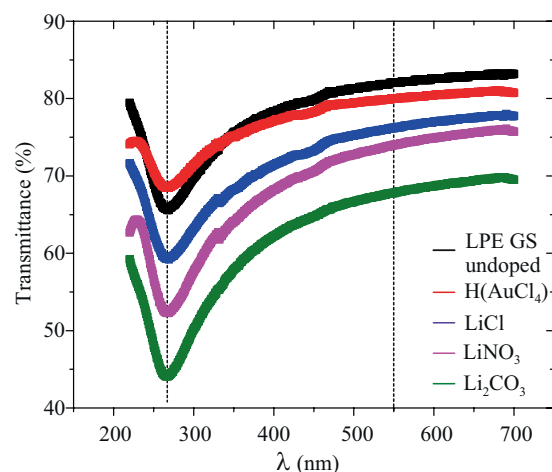


Figure 2. Transmittance spectra of undoped and $\text{H}(\text{AuCl}_4)$, LiCl , LiNO_3 , Li_2CO_3 doped LPE GS films.

cm^{-1}) and 2D (2700 cm^{-1}) are observed for all the samples. No significant shifts of any characteristic Raman peaks of graphene were detected after chemical doping (Fig. 3(a)).

The change of the full width at half-maximum (FWHM) of the Raman spectra after doping with metal standard solutions was negligible Fig. 3(b). The only notable change of the Raman spectra was the increase of the intensity ratio of D to G peaks, $I(\text{D})/I(\text{G})$ (Fig. 3(c)). The quantity of defects has been shown to be related to the ratio between the D and G peaks, $I(\text{D})/I(\text{G})$; the larger the ratio, the larger the defect density³¹. We observe increase of the defect density with $\text{H}(\text{AuCl}_4)$, LiCl , LiNO_3 , Li_2CO_3 doping in relation to the undoped film and the amount of the increase expressed in percent was 37%, 24%, 29% and 21%, respectively.

All self-assembled films suffer from a large defect density that often leads to a high sheet resistance of deposited film. Therefore, the nature and density of defects in any thin film transparent conductor is important, especially when chemical treatment was used to enhance films' performance. The intensity ratio between the D and

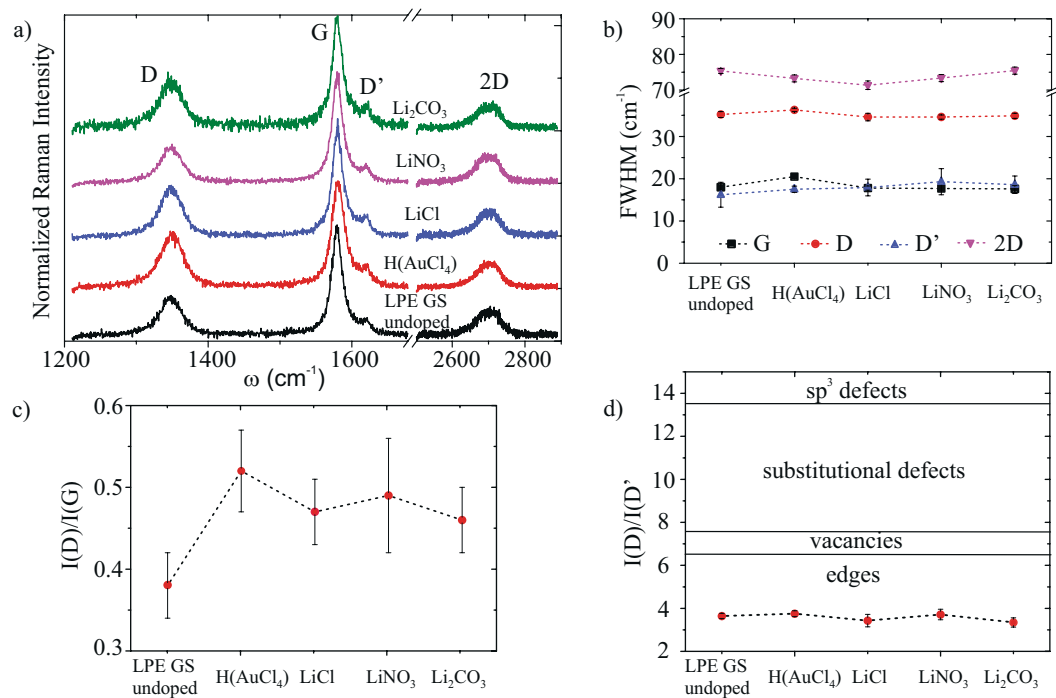


Figure 3. (a) Raman spectra of the undoped LPE GS film and films doped with Li and Au salts, (b) FWHM of the four basic Raman peaks (c) The intensity ratio of D to G peak for different doping metal salts, $I(D)/I(G)$, (d) The intensity ratio of D to D' peak, $I(D)/I(D')$, for different doping metal salts. We refer to peak intensity as the height of the peaks as proposed by Eckmann *et al.*³²

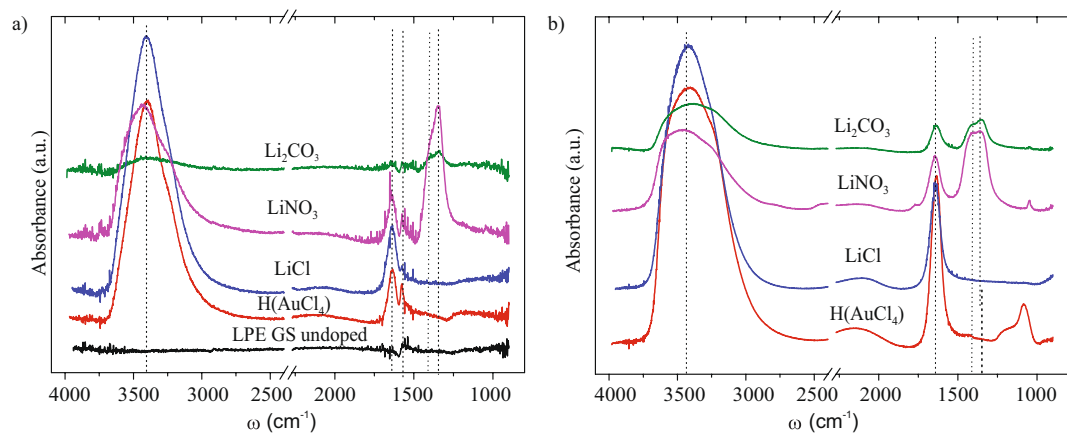


Figure 4. FT-IR spectra of (a) undoped and H(AuCl₄), LiCl, LiNO₃, Li₂CO₃ LPE GS doped films, (b) metal standard solutions (0.1 mg/mL) used for doping processes.

D' peak can be used to get information on the nature of defects in graphene^{32,33}. $I(D)/I(D')$ was calculated, and the obtained results were presented in Fig. 3(d). Topological defects (like pentagon-heptagon pairs), boundaries, vacancies, substitutional impurities and sp^3 defects are possible defects in graphene³¹. Studies reporting a ratio of 3.5 for boundaries, 7 for vacancies, 13 for sp^3 and values in-between those for vacancies and sp^3 for substitutional impurities can be found in the literature^{31,32,34}. From Fig. 3(d) it can be observed that the D to D' intensity peak ratio is nearly constant in our samples regardless of the doping solution, and the value of the ratio indicates that the edges are the dominant type of defects in our LPE GS films.

Fourier transform infrared absorbance (FT-IR) measurements. FT-IR spectra of undoped and LiCl, LiNO₃, Li₂CO₃, H(AuCl₄) doped LPE GS films, as well as FT-IR spectra of corresponding metal standard solutions are shown in Fig. 4.

For the undoped LPE GS film FT-IR spectra is simple. It can be seen only a small peak assignable to C=C skeletal vibration^{35–37} of the graphene basal planes at $\sim 1560\text{ cm}^{-1}$. This peak can also be seen in FT-IR spectra for

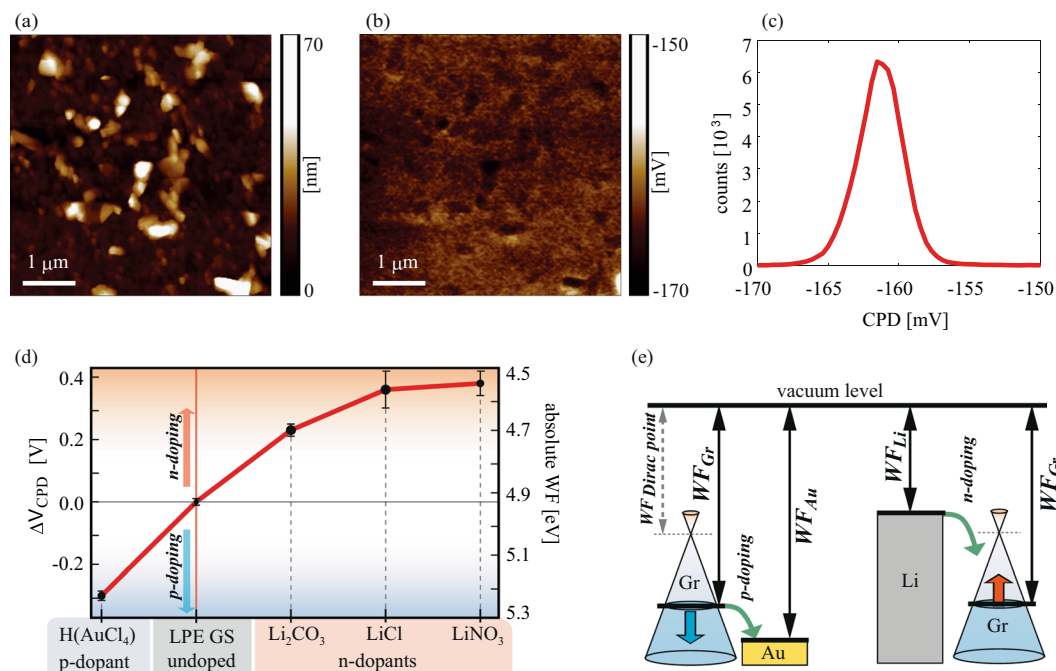


Figure 5. (a) AFM topography, (b) CPD map measured by KPFM, and (c) histogram of (b) shown for H(AuCl₄) doped LPE GS film as an example. (d) Change in WF for doped LPE GS films for different dopants, in comparison to the undoped LPE GS film. Solid red line in (d) is only a guide for the eye. (e) Schematic representation of the work functions prior to the interaction (equal vacuum levels) for Au-based salt/graphene and Li-based salt/graphene. The green arrows indicate direction of electron flow showing that in the case of Li (Au) based salts, electrons are transferred to (from) graphene.

all investigated doped films at the same wavenumber indicating that graphene basal planes were not interrupted by doping. The strong peak at around $\sim 3400\text{ cm}^{-1}$ and another, smaller one, near $\sim 1630\text{ cm}^{-1}$ can be seen in all doped LPE GS films (Fig. 4(a)) and corresponding metal standard solutions (Fig. 4(b)). They are attributed to the water molecules and are assignable to the O-H stretching vibrations ($\sim 3400\text{ cm}^{-1}$) and H-O-H bending mode ($\sim 1630\text{ cm}^{-1}$)^{38,39}. In the case of FT-IR spectra for LPE GS film doped with LiNO₃ the peak at $\sim 1340\text{ cm}^{-1}$ and $\sim 1390\text{ cm}^{-1}$ are assignable to the vibration mode of the NO₃⁻ ions and asymmetric stretch of O-NO₂, respectively^{38,40}. Similar vibration modes can be observed in the case of FT-IR spectra for LPE GS film doped with Li₂CO₃ and can be assigned to the vibration mode of the CO₃⁻ ions (1340 cm^{-1}) and asymmetric stretch of O-CO₂ ($\sim 1390\text{ cm}^{-1}$)⁴¹. The same vibrational modes could be seen for LiNO₃ and Li₂CO₃ standard solutions (Fig. 4(b)).

From the observed FT-IR results (Fig. 4(a)) it is clear that additional peaks appear with LPE GS film chemical doping. These additional peaks match with vibrational modes of the anions in solution (Fig. 4(b)). Considering that no new peaks are visible in the given spectra (which would indicate the formation of chemical bonds) the present peaks could be a consequence of the metal salts adsorption to the graphene lattice during the doping. In order to understand Li and Au doping mechanisms XPS measurements were performed and they are presented in separate section.

Work function modulation. Results for the work function dependent on the different metal standard solution used in the LBA process are summarized in Fig. 5. The top row depicts an example with the topography (Fig. 5(a)), corresponding contact potential difference (CPD) map measured by Kelvin probe force Microscopy-KPFM (Fig. 5(b)), and the histogram of the CPD distribution measured on H(AuCl₄) doped graphene film (Fig. 5(c)). The histogram is characterized with a single peak, which is used for the averaging and calculation of the absolute value of work function. The same procedure was done for all considered films. More details about the measurements of CPD and WF calculations are given in Supplementary information in Supplementary Figs. S3-S5. As a result, the values of the absolute work function are presented in Fig. 5(d) for both, doped and undoped LPE GS films. As can be seen, n-doping of graphene films is achieved by Li-based salts, whereas Au-based salt leads to p-doping.

The change of the WF due to the doping can be explained according to the schematic presentation in Fig. 5(e), illustrating that Li (Au) as a lower (higher) work function material compared to GS films. Therefore, presence of Li-based salts into the graphene film results in a reduction of the work function of the entire film. This behavior can be interpreted as an increase in the Fermi level of GSs – compared to the value for the undoped films – indicating predominantly a charge transfer from Li-based salts to graphene (n-doping), as expected when considering that Li has lower WF than graphene (graphite). In contrast to Li-based salts, the Au-based salt shows an opposite trend for the relative change of the work function. This indicates charge transfer from graphene to

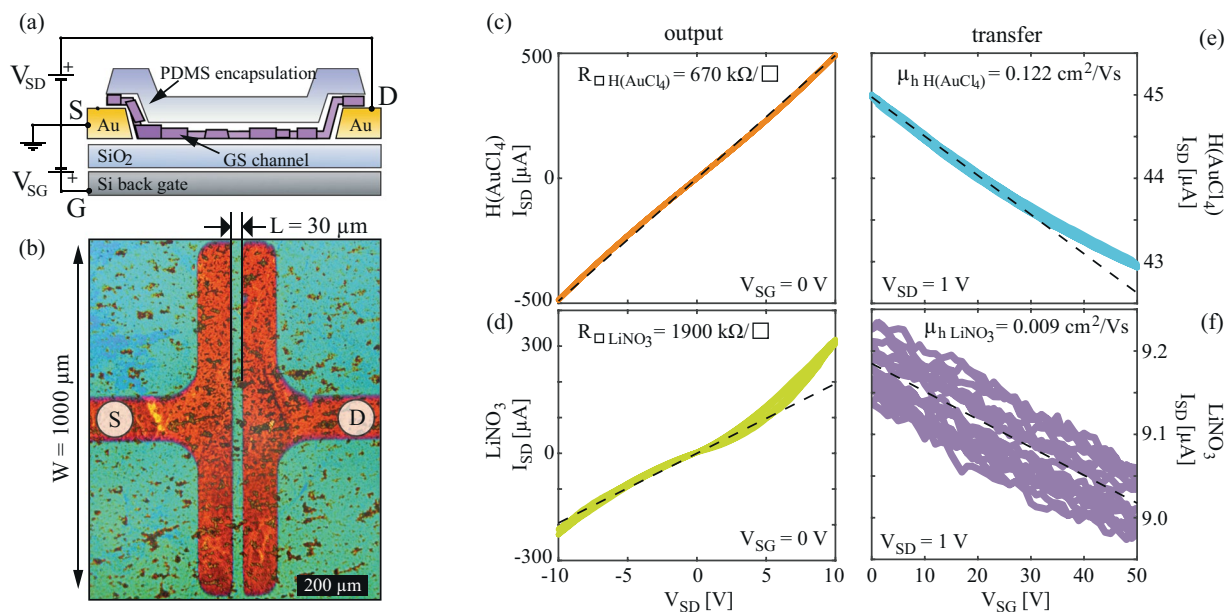


Figure 6. (a) Schematic cross-section of the bottom-contacted back-gated FET devices, also indicating electrical connections. (b) Optical microscopy image of one of the devices, without PDMS capping (for clarity). LBA GS film covers the entire sample surface. (c,d) Output curves of H(AuCl₄) and LiNO₃ doped samples, and (e,f) transfer curves of H(AuCl₄) and LiNO₃ doped samples, respectively. Dashed lines represent least squares linear fits (to selected regions) that were used to extract sheet resistance and linear mobility.

Au-based salt and a relative reduction of the Fermi level in GSs (p-doping). It is also worth mentioning that poly-crystalline nature of LPE based GS films, large amount of sheet edges and presence of the residual solvent (NMP) results in p-doped films⁹, as was also observed in the electrical measurements presented in the following subsection. Therefore, WF values are lower for the LPE-based films by at least 200 meV, than for the pristine exfoliated single-crystals⁴². p-type doping is also reflected on the WF of the reference samples (undoped LPE GS), and therefore on the whole accessible range for the WF modulation by this method. This was also highlighted in Fig. 5(e), where the $WF_{Dirac\ point}$ depicts the case of undoped graphene⁴².

According to Fig. 5(d), the maximal doping in both directions is similar, around 0.3–0.4 eV, finally providing a significant range of around 0.7 eV for the work function modulation of LPE GS films. The achieved range was obtained for 0.1 mg/mL concentration of dopants. For smaller concentrations (one order of magnitude lower, 0.01 mg/mL), the observed changes in CPD were in the order of 10 mV. On the other hand, for higher concentrations (for one order of magnitude higher, 1 mg/mL) gave rise to the problems related to the formation of continuous, large-area LPE GS films, and were therefore excluded from this study. The reported shift of the Fermi level is very similar to the other (comparable) systems in the literature. WF values change of 0.3 eV in our experiment (chemical doping by Au ions) are the same order of magnitude as in Kwon *et al.* manuscripts for gold-chloride (WF change of 0.6 eV²¹, 0.6 eV²², 0.4 eV²⁵). Compared with Kwon *et al.* alkali carbonate²³ and chloride²⁵ graphene chemical doping data (0.4 eV and 0.3–0.4 eV, respectively) WF values change for Li in our manuscript (0.2 eV and 0.4 eV) are in the same order of magnitude. Compared with literature data the same effect can be achieved but advantages of our approach is fast and simple solution-based method for one-step fabrication and WF control of large-area graphene films.

Sheet resistance. The schematic cross-section of the devices used for the electrical characterization is shown in Fig. 6(a), also indicating electrical connections. An optical microscopy image for one of the devices without PDMS encapsulation (for clarity) is shown in Fig. 6(b) illustrating source (S) and drain (D) contact geometries. One characteristic set of transport and output curves for H(AuCl₄) and LiNO₃ doped film is presented in Fig. 6(c–f). Here linear fits were used to extract sheet resistances and apparent linear hole mobilities. Transfer curves for all four salt-treatments and for the reference LPE GS film are presented in the Supplementary information (Supplementary Fig. S1).

In the cases of a reference (undoped) and H(AuCl₄) doped LPE GS samples, output curves barely deviate from a perfect linear behavior in a rather large bias range, indicating that the contact resistance is negligible in comparison to the channel. This is in contrast to all samples doped with Li-based salts, where a significant deviation from the linear output curves were observed at higher bias, indicating non-negligible contact resistance. This can be attributed to large WF differences with Au bottom contacts in the case of Li-based salt doping of the films. Furthermore, while H(AuCl₄) doping enhances electrical performance of the films, a significant increase of the resistivity and reduction of the mobility was observed in the case of all Li-based salt dopings.

The slope of the transfer curves indicates that holes are the majority carriers for all samples, including both the undoped (reference) and all metal salt doped films. Linear fits to the transfer curves were used to estimate

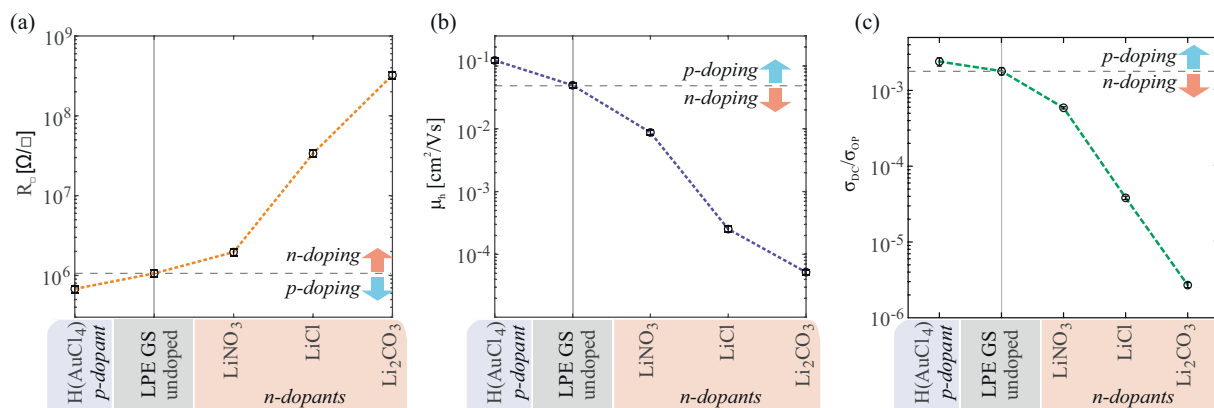


Figure 7. The dependence of the electrical properties of LBA graphene films on the type of metal standard solution based doping; (a) sheet resistance, and (b) apparent linear hole mobility, and (c) direct current conductivity to optical conductivity ratio (σ_{DC}/σ_{OP}). Dashed lines in (a–c) serve only as a guide for the eye.

apparent hole mobility of the devices. While the type of majority carriers was not affected by the doping, a significant (over one order of magnitude) suppression of the field-effect was observed for Li salt dopings of the films.

Figure 7 summarizes electrical properties obtained for all of the measured devices as a function of the different metal based doping.

The results indicate that anions also play a significant role. In the case of Li-based salts, a large variation of the electrical properties was obtained by the different choice of the anion species. Nonetheless, the experiments point out that metal cations dictate the direction of the WF shift (see Fig. 5), as is apparent in the case of H(AuCl₄) and LiCl where only cation species is varied. Our results of metal based doping of LPE graphene films demonstrate a tradeoff between enhancement of the electrical performance and modulation of the WF. Similar results were obtained for CVD doping with Li and Au salts^{23,25}. Of a particular technological relevance is large reduction of the WF of graphene. While many methods for chemical modulation of graphene result in p-type doping^{43–46}, stable and simple n-type doping is much harder to achieve^{47–49}. For an efficient electron injection, a significant reduction of graphene's WF is required. As pointed out by WF measurements and electrical characterization, LiNO₃ is the best choice from the tested Li-based salts with respect to both the largest WF reduction (by 400 meV) and least deterioration of the electrical properties of the films with ~2–3 times increase in sheet resistance compared to the reference (undoped LPE GS).

In contrast, doping of LPE GS films by HNO₃ vapor results in an increase of the apparent mobility⁹. However, using a LiNO₃ solution reduces the mobility by one order of magnitude. Therefore, Li⁺ cations – and not anions – are likely responsible for the deterioration of the electrical properties upon n-doping. An increase of sheet resistance was observed in doping of CVD graphene with alkali metal carbonates and chlorides^{23,25}. There, a significant increase in the sheet resistance was related to the combination of carbon atoms and dopant metals because electron donation occurred^{23,25}. Also, Chen *et al.* observed that the mobility of the charge carriers decreases with the increase of the potassium doping concentration which they attributed to additional scattering caused by ionized potassium atoms^{49,50}. It is most likely that Li⁺ cations are acting as scattering centers for the carriers, or provide traps at the boundaries between neighbouring GSs and effectively increase contact resistance between the overlapping GSs.

Finally, considering that the main potential application of these LPE GS films lies in transparent electrodes, direct current conductivity to optical conductivity ratio (σ_{DC}/σ_{OP}) is presented in Fig. 7(c) for all metal standard solution doping cases and for the reference (undoped). σ_{DC}/σ_{OP} is a parameter frequently reported in order to characterize the relative performance of the films in terms of transparency and sheet resistance^{11,33,51}. The higher the ratio the better the quality of transparent electrodes³³. Compared to the changes in the electrical properties (Fig. 7(a)) the changes in the optical properties (Fig. 2) are minor. Therefore, the dependence of the σ_{DC}/σ_{OP} on the type of the metal-ion doping clearly follows the trend set by $1/R_{\square}$.

X-ray Photoemission Spectroscopy (XPS) measurements. In order to understand Au and Li ion doping mechanisms XPS measurements were performed. C 1s, Au 4f and Li 1s core-level XPS spectra are shown in Fig. 8. N 1s, Cl 2p and O 1s spectra are presented as Supplementary Fig. S2. The C 1s peak of undoped and LiCl, LiNO₃, Li₂CO₃, H(AuCl₄) doped LPE GS films is shown on Fig. 8(a). The C 1s peak is deconvoluted using Gaussian profile into 4 components for undoped and doped films: C=C/C–C in aromatic rings (284.5 eV); C–C sp³ (285.4 eV); C–O (286.6 eV) and C=O (289 eV)^{23,52}. In the case of Li₂CO₃ we can see a small additional peak at 289.2–291.0 eV⁵³ which can be assigned to carbonate. Detected oxygen peak (C=O) is likely due to the residual of NMP and oxygen functionalized edges (C–O) on graphene^{54,55}. The C=C/C–C peak was shifted to a lower binding energy by about 0.16, 0.48, 0.10 and 0.83 eV for H(AuCl₄), LiCl, LiNO₃ and Li₂CO₃ doping process, respectively. The C=C/C–C peak shifts in present work are a consequence of doping by different metal standard solutions. Kwon *et al.* have shown that degree of doping was related to the electronegativity of the anion in the Au complex where anions with a high electronegativity and high bond strength are adequate for use as a p-type

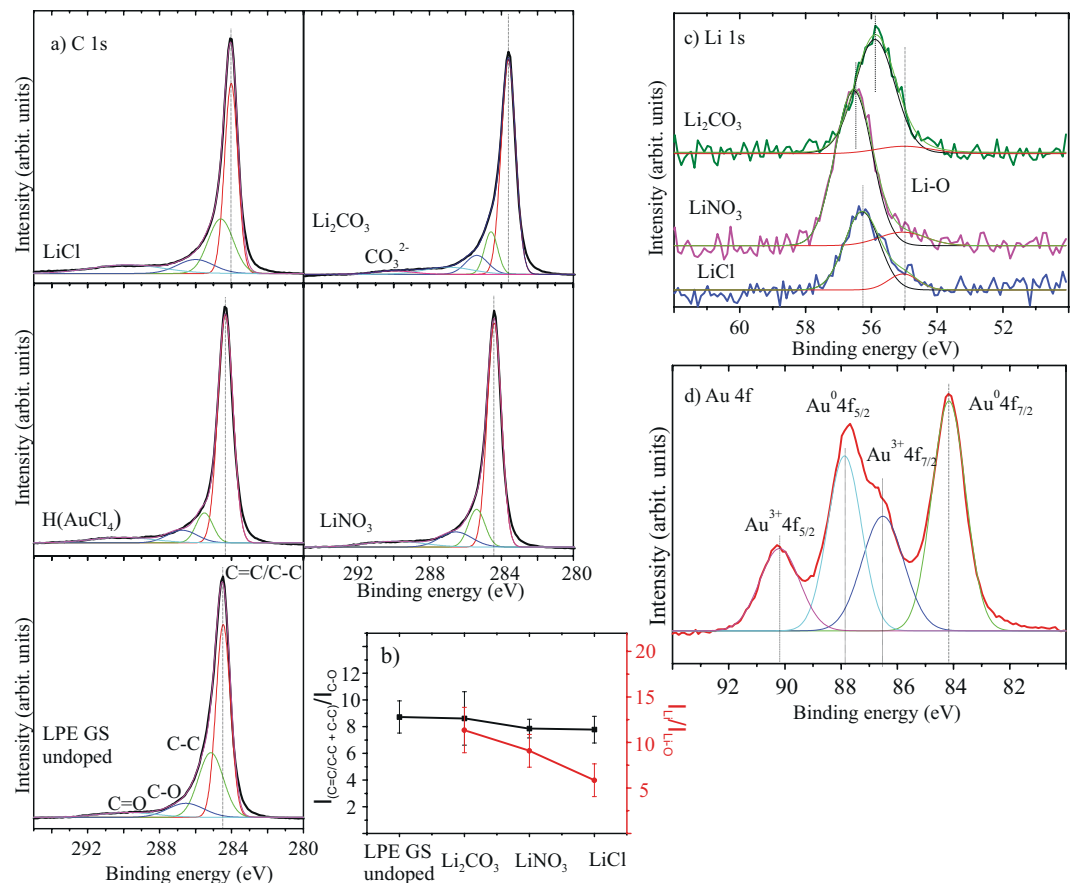


Figure 8. (a) XPS C 1s spectra of undoped and H(AuCl₄), LiCl, LiNO₃, Li₂CO₃ doped LPE GS films. C=C/C-C in aromatic rings (284.5 eV); C-C sp³ (285.4 eV); C-O (286.6 eV) and C=O (289 eV) were considered. For Li₂CO₃ a small additional peak at 289.2–291.0 eV can be assigned to carbonate. (b) Peak intensity ratio for the sum of C=C/C-C and C-C peaks intensities, and the intensity of C-O, $I_{(C=C/C-C+C-C)}/I_{(C-O)}$ (black line) and the ratio of Li 1s intensity from Li salts to Li-O intensity, I_{Li}/I_{Li-O} (red line). (c) XPS Li 1s spectra for different Li compounds and for Li-O. (d) The Au 4f peak in the XPS data of H(AuCl₄).

dopant in graphene²¹. Thus, different shifts of C=C/C-C peak for different metal-salt doping materials could be also a consequence of anions influence on graphene films.

Figure 8(c) show the Li 1s core-level XPS spectra. Literature values for Li 1s core-level for different Li compounds are: LiCl (56.2 eV), Li₂CO₃ (55.5 eV) and LiNO₃ (55.8 eV)⁵⁶ and they correspond well to the values obtained in this work. Li 1s peak at 55.0 eV is assigned to Li-O bond⁵⁷. Vijayakumar and Jianzhi have shown that lithium ion tends to bind with the oxygen rather than the carbon on graphene surface, and interacts by forming Li-O ionic bond⁵⁸. Also Kwon *et al.* have proposed that C-O-X complexes can be formed during doping treatment and can act as an additional dipole to further reduce the value of WF^{23–25,59}. The intensity ratio between sum of the intensities of C=C/C-C and C-C peaks, and the intensity of C-O ($I_{(C=C/C-C+C-C)}/I_{(C-O)}$) is shown in Fig. 8(b). Also, the ratio of Li 1s intensity from Li salts to Li-O intensity (I_{Li}/I_{Li-O}) can be seen in Fig. 8(b). In both cases, intensity ratios decrease for Li₂CO₃, LiNO₃, LiCl, respectively and this implies increased formation of C-O and Li-O bonds. Increased number of Li-O bonds follow the increasing trend of C-O bonds, which is in correlation with the WF change (Fig. 5(d)). The above mentioned results strongly suggest that the mechanism of n-type doped LPE GS films with lithium-salts could be explained with formation of Li complexes (C-O-Li).

Figure 8(d) show the Au 4f peak of gold-chloride doped LPE GS film. The peak is composed of metal (Au⁰) and metal ion (Au³⁺). The peaks at 84.2 eV and 87.9 eV are assigned to neutral Au (Au⁰ 4f_{7/2} and Au⁰ 4f_{5/2}, respectively), and the peaks at 86.5 eV and 90.2 eV are assigned to Au ion (Au³⁺ 4f_{7/2} and Au³⁺ 4f_{5/2}, respectively). Au ions (Au³⁺) have positive reduction potential and have tendency to spontaneously accept charges from other materials (graphene) and reduce to Au⁰^{21,22,25,60}. Therefore, the mechanism of p-doped LPE GS film can be explained as spontaneous electron transfer from graphene film to Au³⁺, resulting in depletion of electrons in the graphene networks, thus increasing the WF of doped graphene.

Conclusion

We demonstrate a straightforward single-step method for forming and doping of LPE GS films by metal standard solutions through charge transfer processes. Chemical doping of graphene allows to modulate its WF in a very large range, and therefore potentially enables to use the same electrode material for both, the injection and for the extraction of the electrons. n-doping of graphene films is achieved by Li-based salts, whereas Au-based salt leads

to p-doping. Furthermore, solution-processed graphene films are in particular suited for the chemical modulations, since a large number of the sheet edges opens up many adsorption sites and enhances the doping effects when compared to many other types of graphene.

The morphology of the LPE GS films does not change with the doping process, except that doped films contain agglomerates. FT-IR measurements point out that graphene basal planes stay chemically unchanged with metal doping and the charge transfer process is enabled with adsorption of the metal salts. Li-based salts decrease the WF, while Au-based salts increase the WF of the entire film. The maximal doping in both directions gives a significant range of around 0.7 eV for the work function modulation. Changing the dopant (Au or Li based salts) significantly affects the electrical properties of the films. In the case of the Li-based salts doping of the film, a significant suppression of the field-effect mobility and the increase of the sheet resistance was observed. This indicates that adsorbed Li-anions act as scattering centers for the charges. XPS data indicated that different mechanisms exist in the case of Au and Li doping. For Au ions spontaneous charge transfer occurred from graphene, thus increasing WF. In the case of Li doping, potential adsorption sites are a large number of the sheet edges where C-O bonds are preferential sites for lithium ions and for forming of C-O-Li complexes. In all cases graphene films are p-type, which is in accordance with KPFM measurements. Also, tradeoff between Li complex which reduce the value of WF and anion which increase the value of WF could be a reason of such a doping.

Metal salts charge transfer doping – which happens with this single-step method – provides a facile and effective method to tune the WF of LPE graphene therefore extending the potential use of these materials in low-cost transparent electrode applications.

Methods

Preparation of GS dispersion and doping solutions. A dispersion of GS in N-methyl-2-pyrrolidone (NMP, Sigma Aldrich, product no. 328634) has been used. GS dispersion was prepared from graphite powder (Sigma Aldrich, product no. 332461) of initial concentration 18 mg/mL. The solution was sonicated in a low-power ultrasonic bath for 14 h. The resulting dispersion was centrifuged for 60 min at 3000 rpm immediately after the sonication.

Stock standard solutions used in our work for n-doping are 1 mg/mL LiCl, LiNO₃ and Li₂CO₃ and for p-doping is 1 mg/mL gold standard solution (Merck, H(AuCl₄), product no. 170216). Lithium standard solutions were prepared from originated Li salts (LiCl, LiNO₃ and Li₂CO₃, Merck, product no. 105679, 105653 and 105680, respectively). By appropriate dilution of the stock solution with deionized water we obtained 0.1 mg/mL metal water solution which is then used in doping process.

Deposition on a substrate and doping of LPE GS films. GS dispersion in NMP was used to fabricate transparent and conductive films by LBA technique at a water-air interface, like in our previous work^{9,29,61}. A small amount of GS dispersion was added to the water-air interface and after the film was formed it was slowly scooped onto the target substrate. Applying the same process of fabricating the GS films and using the appropriate metal standard solution instead of water, chemical doping was achieved. As substrates SiO₂/Si wafer were used for electrical and WF measurements, while quartz and CaF₂ substrates were chosen for optical and FT-IR spectroscopy, respectively.

Characterization of undoped and doped LPE GS films. The Morphology of LPE GS films was studied by optical and atomic force microscopy (AFM). Topographic AFM measurements were done by NTEGRA Prima AFM system and NSG01 probes with a typical tip radius of around 10 nm. The surface roughness of LPE GS films was calculated as a root-mean square of the height distribution and averaged on ten 50 × 50 μm² areas.

Kelvin probe force microscopy (KPFM) – established almost three decades ago⁶² and in the meantime frequently applied to graphene^{42,63–65} – was employed in order to characterize changes in the electrical surface potential and corresponding Fermi level shifts due to doping. For this purpose, we measured the contact potential difference (CPD) between AFM tip and the sample surface⁶⁶ by using Pt covered NSG01/Pt probes with a typical tip curvature radius of 35 nm. In the first pass of KPFM, the sample topography was measured in tapping AFM mode. In the second pass, the probe was lifted by 20 nm, and moved along the trajectory measured in the first pass. Simultaneously, the sum of AC and DC voltage was applied between the sample and the probe. The AC voltage excites AFM probe oscillations during its movement, while the CPD between AFM tip and the sample surface in every point is then equal to the value of variable DC voltage which cancels the AFM probe oscillations. For all samples, the CPD was measured on five 5 × 5 μm² areas, and then averaged. In order to obtain the absolute value of the work function, the following procedure was applied⁴². The CPD is equal to the work function difference between AFM tip (WF_t) and sample (WF_s), CPD = WF_t - WF_s. The calibration of the WF_t was done by a standard procedure consisting of KPFM measurements on a freshly cleaved HOPG with a well known work function of 4.6 eV⁴². Finally, the sample work function was calculated as WF_s = WF_t - CPD, where CPD is measured by KPFM for all, undoped and doped LPE GS films.

The effect of chemical doping on optical properties of LBA GS films was investigated with measurements of optical transmittance, using UV-VIS spectrophotometer (Beckman Coulter DU 720 UV-VIS Spectrophotometer).

Electrical measurements were performed under ambient conditions in a standard field-effect device configuration with Si substrate acting as a back gate electrode, using Keithley 2636 A SYSTEM SourceMeter. Devices were based on bottom-contact gold pads defined by a shadow mask with L/W = 30 μm/1000 μm, and SiO₂ as a gate dielectric with thickness of 285 nm. Graphene films were deposited using the same LBA method as described above. The top surface of the devices was encapsulated by polydimethylsiloxane (PDMS) films (GelPak X4) to ensure stable performance and minimize any adsorption/desorption during electrical measurements that could occur from the surroundings (e.g. water vapor). Electrical characterization was performed on several devices of each doping with metal standard solution, and for undoped films as a reference. For each device ten subsequent forward and

backward transfer and output curves were measured, using low sweeping rate ($\sim 0.005\text{--}1$ Hz per point in a voltage sweep) to minimize parasitic capacitance. Sheet resistance and apparent linear field-effect mobility were extracted using fits to output and transfer curves, respectively. For the output measurements source-drain bias was varied in a range between -10 V and $+10$ V, with the gate electrode grounded. For transfer measurements, the gate voltage was varied between 0 V and 50 V, with source-drain bias at 1 V in all cases except for Li_2CO_3 where due to a very weak field-effect (very low mobility) 10 V bias was used.

The room-temperature micro-Raman spectra of undoped and metal salt doped LPE GS films were collected using Tri Vista 557 triple spectrometer coupled to the liquid nitrogen-cooled CCD detector. Nd:YAG laser line of 532 nm was used for the excitation and 50 magnification objective was used for focusing the beam onto the sample. Low laser power (less than 1 mW) was applied to prevent the thermal degradation of the sample. Each LPE GS film sample was measured at eight different positions.

Fourier transform infrared absorbance spectra (FT-IR spectra) of undoped and metal salt doped LPE GS films were measured over a range of $400\text{--}4000$ cm^{-1} with Nicolet Nexus 470 FT-IR spectrometer. Standard solutions which were used for the preparation of doped films were measured too and they were prepared by drop casting method on the CaF_2 substrate.

XPS spectra were recorded using a Thermo Scientific instrument (K-Alpha spectrometer, Thermo Fisher Scientific, Waltham, USA) equipped with a monochromatic Al $K\alpha$ X-ray source (1486.6 eV). High-resolution scans were performed with a pass energy of 50 eV and a step size of 0.1 eV. All analyses were performed at room temperature.

Data availability

The datasets obtained and analysed during the current study that are not included in this article are available from the corresponding authors on reasonable request.

Received: 17 June 2019; Accepted: 28 April 2020;

Published online: 21 May 2020

References

- Geim, A. K. Graphene: Status and prospects. *Science* **324**, 1530–1534 (2009).
- Geim, A. K. & Novoselov, K. S. The rise of graphene. *Nat. Mater.* **6**, 183–191 (2007).
- Novoselov, K. S. *et al.* Room-temperature quantum hall effect in graphene. *Science* **315**, 1379–1379 (2007).
- Bonaccorso, F., Sun, Z., Hasan, T. & Ferrari, A. C. Graphene photonics and optoelectronics. *Nat. Photonics* **4**, 611–622 (2010).
- Kwon, K. C., Kim, B. J., Lee, J. L. & Kim, S. Y. Role of ionic chlorine in the thermal degradation of metal chloride-doped graphene sheets. *J. Mater. Chem. C* **1**, 253–259 (2013).
- Ferrari, A. C. *et al.* Science and technology roadmap for graphene, related two-dimensional crystals, and hybrid systems. *Nanoscale* **7**, 4598–4810 (2015).
- Backes, C. *et al.* Guidelines for exfoliation, characterization and processing of layered materials produced by liquid exfoliation. *Chem. Mater.* **29**, 243–255 (2017).
- Li, X. *et al.* Highly conducting graphene sheets and Langmuir-Blodgett films. *Nat. Nanotechnol.* **3**, 538–542 (2008).
- Matković, A. *et al.* Enhanced sheet conductivity of Langmuir-Blodgett assembled graphene thin films by chemical doping. *2D Mater.* **3**, 015002 (2016).
- Lee, S. K. *et al.* All graphene-based thin film transistors on flexible plastic substrates. *Nano Lett.* **12**, 3472–3476 (2012).
- Zheng, Q. *et al.* Transparent conductive films consisting of ultralarge graphene sheets produced by Langmuir-Blodgett assembly. *ACS Nano* **5**, 6039–6051 (2011).
- Park, J. *et al.* Work-function engineering of graphene electrodes by self-assembled monolayers for high-performance organic field-effect transistors. *J. Phys. Chem. Lett.* **2**, 841–845 (2011).
- Tong, S. W., Wang, Y., Zheng, Y., Ng, M. F. & Loh, K. P. Graphene intermediate layer in tandem organic photovoltaic cells. *Adv. Funct. Mater.* **21**, 4430–4435 (2011).
- Wang, Y., Tong, S. W., Xu, X. F., Özyilmaz, B. & Loh, K. P. Interface engineering of layer-by-layer stacked graphene anodes for high-performance organic solar cells. *Adv. Mater.* **23**, 1514–1518 (2011).
- Wu, J. *et al.* Organic light-emitting diodes on solution-processed graphene transparent electrodes. *ACS Nano* **4**, 43–48 (2010).
- Wang, X., Zhi, L. & Mullen, K. Transparent, conductive graphene electrodes for dye-sensitized solar cells. *Nano Lett.* **8**, 323–327 (2008).
- Alfano, B. *et al.* Modulating the sensing properties of graphene through an eco-friendly metal-decoration process. *Sensors Actuators, B Chem.* **222**, 1032–1042 (2016).
- Lynch, P., Khan, U., Harvey, A., Ahmed, I. & Coleman, J. N. Graphene-MoS₂ nanosheet composites as electrodes for dye sensitised solar cells. *Mater. Res. Express* **3**, 035007 (2016).
- Mosciatti, T. *et al.* A multifunctional polymer-graphene thin-film transistor with tunable transport regimes. *ACS Nano* **9**, 2357–2367 (2015).
- Giubileo, F. & Di Bartolomeo, A. The role of contact resistance in graphene field-effect devices. *Prog. Surf. Sci.* **92**, 143–175 (2017).
- Kwon, K. C., Kim, B. J., Lee, J. L. & Kim, S. Y. Effect of anions in Au complexes on doping and degradation of graphene. *J. Mater. Chem. C* **1**, 2463–2469 (2013).
- Kwon, K. C., Choi, K. S. & Kim, S. Y. Increased work function in few-layer graphene sheets via metal chloride doping. *Adv. Funct. Mater.* **22**, 4724–4731 (2012).
- Kwon, K. C., Choi, K. S., Kim, B. J., Lee, J. L. & Kim, S. Y. Work-function decrease of graphene sheet using alkali metal carbonates. *J. Phys. Chem. C* **116**, 26586–26591 (2012).
- Huang, J. H., Fang, J. H., Liu, C. C. & Chu, C. W. Effective work function modulation of graphene/carbon nanotube composite films as transparent cathodes for organic optoelectronics. *ACS Nano* **5**, 6262–6271 (2011).
- Kwon, K. C., Choi, K. S., Kim, C. & Kim, S. Y. Role of metal cations in alkali metal chloride doped graphene. *J. Phys. Chem. C* **118**, 8187–8193 (2014).
- Wang, X., Xu, J. B., Xie, W. & Du, J. Quantitative analysis of graphene doping by organic molecular charge transfer. *J. Phys. Chem. C* **115**, 7596–7602 (2011).
- Shin, H. J. *et al.* Control of electronic structure of graphene by various dopants and their effects on a nanogenerator. *J. Am. Chem. Soc.* **132**, 15603–15609 (2010).
- Shi, Y. *et al.* Work function engineering of graphene electrode via chemical doping. *ACS Nano* **4**, 2689–2694 (2010).

29. Tomašević-Ilić, T. *et al.* Reducing sheet resistance of self-assembled transparent graphene films by defect patching and doping with UV/ozone treatment. *Appl. Surf. Sci.* **458**, 446–453 (2018).
30. Matković, A. *et al.* Spectroscopic imaging ellipsometry and Fano resonance modeling of graphene. *J. Appl. Phys.* **112**, 123523 (2012).
31. Bracamonte, M. V., Lacconi, G. I., Urreta, S. E. & Foa Torres, L. E. F. F. On the nature of defects in liquid-phase exfoliated graphene. *J. Phys. Chem. C* **118**, 15455–15459 (2014).
32. Eckmann, A. *et al.* Probing the nature of defects in graphene by Raman spectroscopy. *Nano Lett.* **12**, 3925–3930 (2012).
33. Rytel, K. *et al.* Ultrasonication-induced sp³ hybridization defects in Langmuir-Schaefer layers of turbostratic graphene. *Phys. Chem. Chem. Phys.* **20**, 12777–12784 (2018).
34. Eckmann, A., Felten, A., Verzhbitskiy, I., Davey, R. & Casiraghi, C. Raman study on defective graphene: Effect of the excitation energy, type, and amount of defects. *Phys. Rev. B - Condens. Matter Mater. Phys.* **88**, 035426 (2013).
35. Drewniak, S. *et al.* Studies of reduced graphene oxide and graphite oxide in the aspect of their possible application in gas sensors. *Sensors* **16**, 103 (2016).
36. Kim, W. J., Basavaraja, C., Thinh, P. X. & Huh, D. S. Structural characterization and DC conductivity of honeycomb-patterned poly(ϵ -caprolactone)/gold nanoparticle-reduced graphite oxide composite films. *Mater. Lett.* **90**, 14–18 (2013).
37. Țucureanu, V., Matei, A. & Avram, A. M. FTIR spectroscopy for carbon family study. *Crit. Rev. Anal. Chem.* **46**, 502–520 (2016).
38. Wu, X. *et al.* One-step freezing temperature crystallization of layered rare-earth hydroxide (Ln₂(OH)₅NO₃·nH₂O) nanosheets for a wide spectrum of Ln (Ln = Pr-Er, and Y), anion exchange with fluorine and sulfate, and microscopic coordination probed via photoluminescence. *J. Mater. Chem. C* **3**, 3428–3437 (2015).
39. Nakamoto, K. *Infrared and Raman Spectra of Inorganic and Coordination Compounds. Part A: Theory and Applications in Inorganic Chemistry; Part B: Application in Coordination, Organometallic, and Bioinorganic Chemistry*, 5th Edition (Nakamoto, Kazuo). *John Wiley and Sons* (John Wiley and Sons, 2009).
40. Geng, F. *et al.* New layered rare-earth hydroxides with anion-exchange properties. *Chem. Eur. J.* **14**, 9255–9260 (2008).
41. Lefèvre, G. *In situ* Fourier-transform infrared spectroscopy studies of inorganic ions adsorption on metal oxides and hydroxides. *Adv. Colloid Interface Sci.* **107**, 109–123 (2004).
42. Yu, Y. *et al.* Tuning the graphene work function by electric field effect. *Nano Lett.* **9**, 3430–3434 (2009).
43. Levesque, P. L. *et al.* Probing charge transfer at surfaces using graphene transistors. *Nano Lett.* **11**, 132–137 (2011).
44. Kuruvila, A. *et al.* Organic light emitting diodes with environmentally and thermally stable doped graphene electrodes. *J. Mater. Chem. C* **2**, 6940–6945 (2014).
45. Meyer, J. *et al.* Metal oxide induced charge transfer doping and band alignment of graphene electrodes for efficient organic light emitting diodes. *Sci. Rep.* **4**, 5380 (2014).
46. Matković, A. *et al.* Probing charge transfer between molecular semiconductors and graphene. *Sci. Rep.* **7**, 9544 (2017).
47. Sanders, S. *et al.* Engineering high charge transfer n-doping of graphene electrodes and its application to organic electronics. *Nanoscale* **7**, 13135–13142 (2015).
48. Han, K. S. *et al.* A non-destructive n-doping method for graphene with precise control of electronic properties via atomic layer deposition. *Nanoscale* **8**, 5000–5005 (2016).
49. Chen, J. H. *et al.* Charged-impurity scattering in graphene. *Nat. Phys.* **4**, 377–381 (2008).
50. Pinto, H. & Markevich, A. Electronic and electrochemical doping of graphene by surface adsorbates. *Beilstein J. Nanotechnol.* **5**, 1842–1848 (2014).
51. De, S. & Coleman, J. N. Are there fundamental limitations on the sheet resistance and transmittance of thin graphene films? *ACS Nano* **4**, 2713–2720 (2010).
52. Benayad, A. *et al.* Controlling work function of reduced graphite oxide with Au-ion concentration. *Chem. Phys. Lett.* **475**, 91–95 (2009).
53. López, G. P., Castner, D. G. & Ratner, B. D. XPS O 1s binding energies for polymers containing hydroxyl, ether, ketone and ester groups. *Surf. Interface Anal.* **17**, 267–272 (1991).
54. Hernandez, Y. *et al.* High-yield production of graphene by liquid-phase exfoliation of graphite. *Nat. Nanotechnol.* **3**, 563–568 (2008).
55. Kim, H. *et al.* Optoelectronic properties of graphene thin films deposited by a Langmuir-Blodgett assembly. *Nanoscale* **5**, 12365–12374 (2013).
56. Naumkin, A. V., Kraut-Vass, A., Gaarenstroom, S. W. & Powell, C. J. NIST X-ray photoelectron spectroscopy database. Available at: https://srdata.nist.gov/xps/EngElmSrChQuery.aspx?EType=PE&CSOpt=Retri_ex_dat&Elm=Li. (2019).
57. Moulder, J. F., Stickle, W. F., Sobol, P. E. & Bomben, K. D. *Handbook of X-ray photoelectron spectroscopy. Reference book of standard spectra for identification and interpretation of XPS data* (Perkin-Elmer Corporation, Physical Electronic division, 1992).
58. Vijayakumar, M. & Jianzhi, H. Exploring the interaction between lithium ion and defective graphene surface using dispersion corrected DFT studies. *ECS Trans* **53**, 23–32 (2013).
59. Pickett, W. E. Negative electron affinity and low work function surface: Cesium on oxygenated diamond (100). *Phys. Rev. Lett.* **73**, 1664–1667 (1994).
60. Syu, J. Y. *et al.* Wide-range work-function tuning of active graphene transparent electrodes via hole doping. *RSC Adv.* **6**, 32746–32756 (2016).
61. Tomašević-Ilić, T. *et al.* Transparent and conductive films from liquid phase exfoliated graphene. *Opt. Quantum Electron.* **48**, 319 (2016).
62. Nonnenmacher, M., O'Boyle, M. P. & Wickramasinghe, H. K. Kelvin probe force microscopy. *Appl. Phys. Lett.* **58**, 2921–2923 (1991).
63. Vasić, B. *et al.* Atomic force microscopy based manipulation of graphene using dynamic plowing lithography. *Nanotechnology* **24**, 015303 (2013).
64. Vasić, B. *et al.* Low-friction, wear-resistant, and electrically homogeneous multilayer graphene grown by chemical vapor deposition on molybdenum. *Appl. Surf. Sci.* **509**, 144792 (2020).
65. Panchal, V., Pearce, R., Yakimova, R., Tzalenchuk, A. & Kazakova, O. Standardization of surface potential measurements of graphene domains. *Sci. Rep.* **3**, 2597 (2013).
66. Udum, Y. *et al.* Inverted bulk-heterojunction solar cell with cross-linked hole-blocking layer. *Org. Electron.* **15**, 997–1001 (2014).

Acknowledgements

This work has been supported from the Serbian MPNTR through projects OI 171005, OI 171032, 451-03-02141/2017-09/32 and with support from the Lise Meitner fellowship by Austrian Science Fund (FWF): M 2323-N36. We further acknowledge support by the Austrian Academic Exchange Service (OeAD) via the project SRB 13/2018.

Author contributions

I.M. devised the concept of LPE GS films doping with metal standard solutions in the single-step method. I.M. and J.V. prepared LPE dispersions and fabricated undoped and doped LPE GS films on different substrates. B.V. did AFM and KPFM measurements, A.M. performed electrical measurements, I.M. and J.V. did FTIR measurements, S.A. and I.M. performed Raman measurements and I.M., T.G., M.K., S.A. and J.V. performed and

processed XPS measurements. C.T. and R.G. oversaw the study. I.M., A.M. and B.V. wrote the manuscript. All authors discussed and analysed the results and reviewed the manuscript.

Competing interests

The authors declare no competing interests.

Additional information

Supplementary information is available for this paper at <https://doi.org/10.1038/s41598-020-65379-1>.

Correspondence and requests for materials should be addressed to I.R.M. or A.M.

Reprints and permissions information is available at www.nature.com/reprints.

Publisher's note Springer Nature remains neutral with regard to jurisdictional claims in published maps and institutional affiliations.



Open Access This article is licensed under a Creative Commons Attribution 4.0 International License, which permits use, sharing, adaptation, distribution and reproduction in any medium or format, as long as you give appropriate credit to the original author(s) and the source, provide a link to the Creative Commons license, and indicate if changes were made. The images or other third party material in this article are included in the article's Creative Commons license, unless indicated otherwise in a credit line to the material. If material is not included in the article's Creative Commons license and your intended use is not permitted by statutory regulation or exceeds the permitted use, you will need to obtain permission directly from the copyright holder. To view a copy of this license, visit <http://creativecommons.org/licenses/by/4.0/>.

© The Author(s) 2020

Single-step fabrication and work function engineering of Langmuir-Blodgett assembled few-layer graphene films with Li and Au salts

Ivana R. Milošević^{1,*}, Borislav Vasić¹, Aleksandar Matković^{2,*}, Jasna Vujin¹, Sonja Aškračić³, Markus Kratzer², Thomas Griesser⁴, Christian Teichert² and Radoš Gajić¹

¹Laboratory for Graphene, other 2D Materials and Ordered Nanostructures of Center for Solid State Physics and New Materials, Institute of Physics, University of Belgrade, Pregrevica 118, 11080 Belgrade, Serbia

²Institute of Physics, Montanuniversität Leoben, Franz Josef Str. 18, 8700 Leoben, Austria

³Nanostructured Matter Laboratory of Center for Solid State Physics and New Materials, Institute of Physics, University of Belgrade, Pregrevica 118, 11080 Belgrade, Serbia

⁴Institute of Chemistry of Polymeric Materials, Montanuniversitaet Leoben, Otto-Gloeckel-Straße 2, 8700 Leoben, Austria

*novovic@ipb.ac.rs

*aleksandar.matkovic@unileoben.ac.at

S1: Transfer characteristics

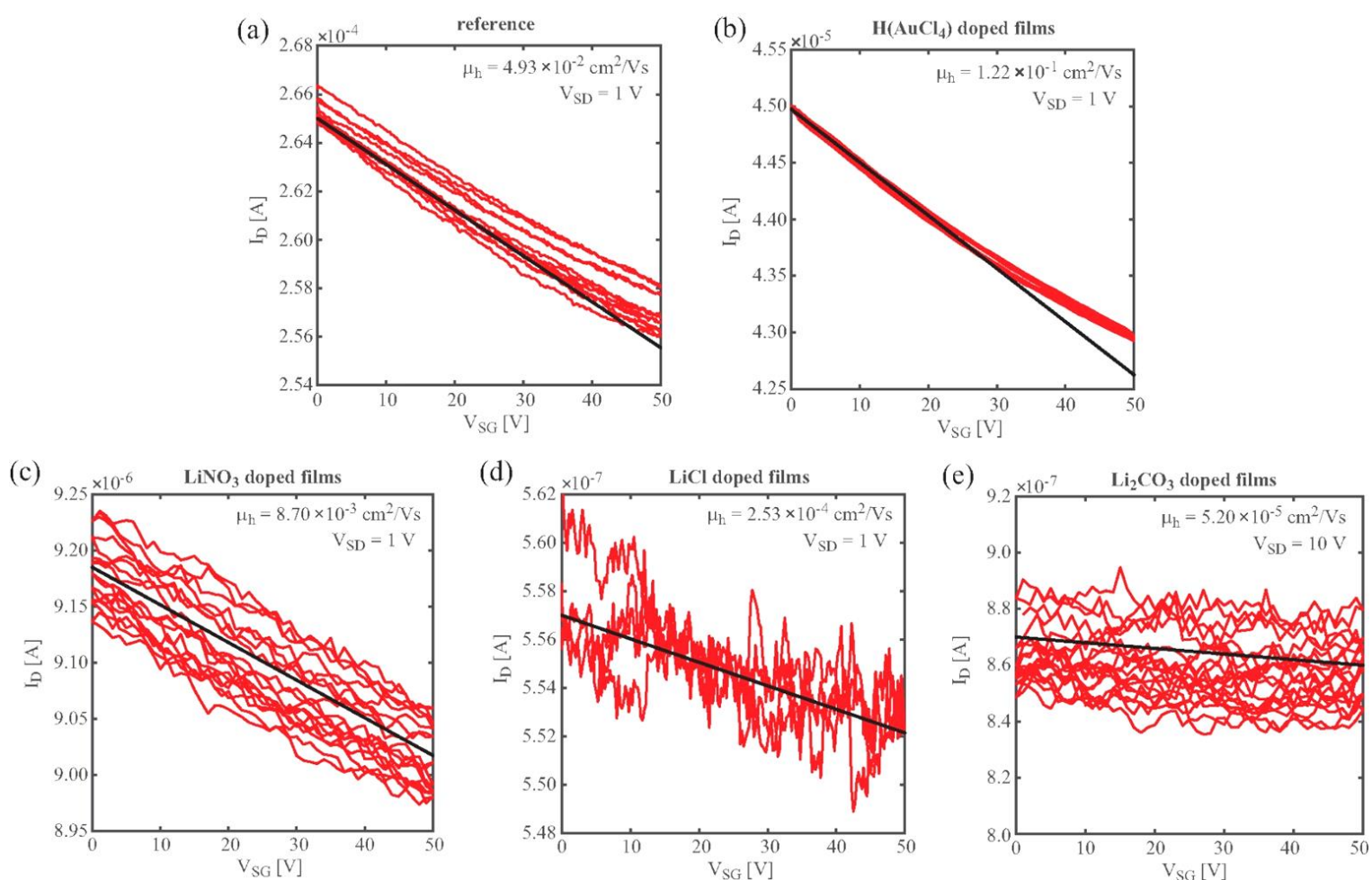


Figure S1: Transfer characteristics. (a) Reference LBA GS film, formed at the interface DI water-air without introduction of salts. (b-e) H(AuCl₄), LiNO₃, LiCl, and Li₂CO₃ doped LBA GS films. Red lines represent five subsequent forward and backward sweeps. Black lines are linear fits used to estimate apparent hole mobility of the FETs. Source-drain bias (V_{SD}) was set to 1 V in all cases, except for Li₂CO₃-doping where due to low conductivity of the films $V_{SD} = 10$ V. The slopes of the curves indicate that within the accessible range of source-gate bias (V_{SG}), holes are majority carriers. Charge neutrality point was not reached within the available V_{SG} range (limited by SiO₂ dielectric breakdown). The gate leakage current was in all cases below 1 nA.

S2: X-ray Photoemission Spectroscopy core-level spectra for O 1s, N 1s and Cl 2p

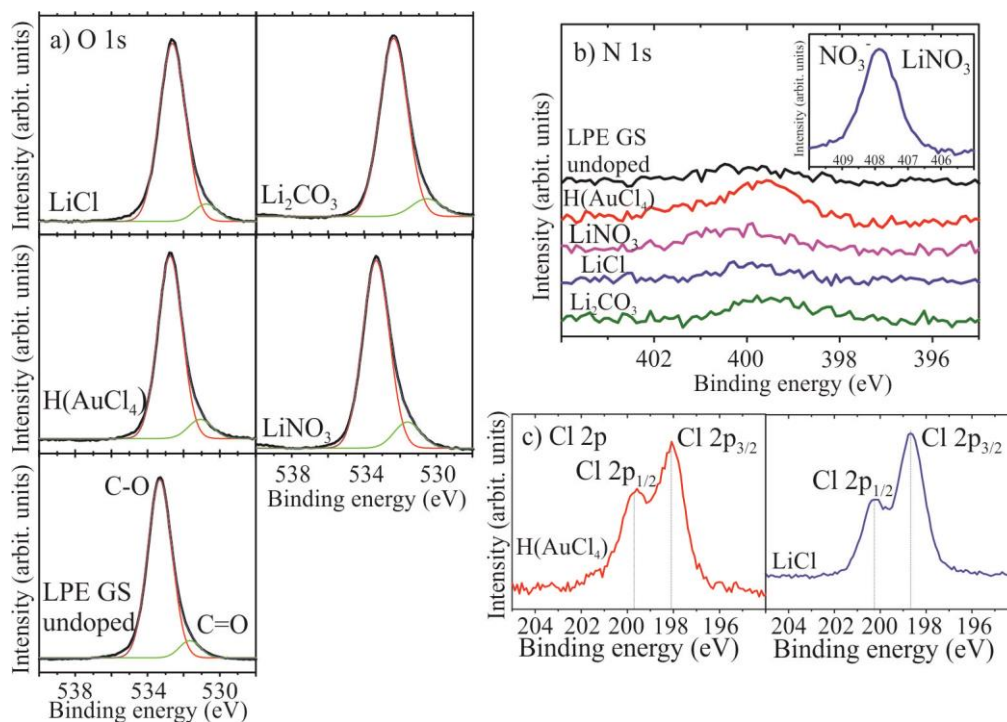


Figure S2: (a) The O 1s core-level XPS spectra for LPE GS undoped and H(AuCl₄), LiNO₃, LiCl and Li₂CO₃ doped films. The O 1s spectra can be deconvoluted in 2 components: C-O (533.6 eV) and C=O (532 eV)¹. (b) The XPS N 1s spectra (400.0 eV) indicating nitrogen^{2,3} presence in undoped and metal-doped films likely due to the residual of NMP/Nitrate peak⁴ for LiNO₃ doped graphene films at 407.3 eV (inset). (c) The XPS Cl 2p spectra for H(AuCl₄) and LiCl doped LBA GS films. Literature data for Cl 2p_{3/2} and Cl 2p_{1/2} in the case of H(AuCl₄) are 198.4 eV⁴ and 199.8 eV⁵ and for LiCl are 198.8 eV⁴ and 200.4 eV, respectively.

1. Matković, A. *et al.* Enhanced sheet conductivity of Langmuir-Blodgett assembled graphene thin films by chemical doping. *2D Mater.* **3**, 015002 (2016).
2. Sun, H. *et al.* Binder-free graphene as an advanced anode for lithium batteries. *J. Mater. Chem. A* **4**, 6886–6895 (2016).
3. Thodkar, K. *et al.* Restoring the Electrical Properties of CVD Graphene via Physisorption of Molecular Adsorbates. *ACS Appl. Mater. Interfaces* **9**, 25014–25022 (2017).
4. Naumkin, A. V., Kraut-Vass, A., Gaarenstroom, S. W. & Powell, C. J. NIST X-ray photoelectron spectroscopy database. Available at: https://srdata.nist.gov/xps/EngElmSrchQuery.aspx?EType=PE&CSOpt=Retri_ex_dat&Elm=Li (2019).
5. Syu, J. Y. *et al.* Wide-range work-function tuning of active graphene transparent electrodes via hole doping. *RSC Adv.* **6**, 32746–32756 (2016).

S3: KPFM measurements

CPD of investigated samples was measured by KPFM. It is very convenient technique for investigations of inhomogeneous samples in order to resolve spatial variations of electrical properties at micro- and nano-scale, which is not possible by other techniques. We did KPFM measurements on several (5-6) different $5 \times 5 \mu\text{m}^2$ areas on every sample and then averaged them. We observed that the CPD is quite homogeneous and constant despite of inhomogeneity of sample morphology.

Typical example is given in Fig. S3 which depicts topography (left column), CPD maps (middle column) and corresponding CPD histograms (right column) for six different $5 \times 5 \mu\text{m}^2$ areas of the LPE graphene film doped with H(AuCl₄). As can be seen, the morphology is quite inhomogeneous. On the other hand, all CPD histograms are characterized with single and well defined peaks positioned at -187 mV, -181 mV, -157 mV, -179 mV, -168 mV, and -162 mV. The average CPD is -172 ± 15 mV. All CPD histograms are shown together in Fig. S4 for clarity. The peaks do not shift appreciably while the deviation is only 15 mV which is less than 10%. Similar procedure was repeated for all investigated samples and the results are summarized in Fig. S5. It depicts measured distributions of CPD for doped LPE GS films for different dopants, with respect to the undoped LPE GS film taken as a reference. Shifting of CPD peaks is clearly resolved demonstrating efficiency of KPFM for studying doping of LPE graphene films.

KPFM was used to calibrate the WF of AFM tips as well. This was done by KPFM measurements on a freshly cleaved HOPG with a well-known work function of 4.6 eV. The average CPD measured on HOPG with Pt covered NSG01/Pt probes was 460 mV. Therefore, the calculated tip work function was $WF_t = WF_{\text{HOPG}} + \text{CPD}(\text{HOPG}) = 5.06$ eV. Finally, the sample work function was calculated as $WF_s = WF_t - \text{CPD}$, where CPD is measured by KPFM on LPE GS films. In the case of the LPE graphene film doped with H(AuCl₄), the measured WF was 5.232 eV and this is the value presented in Fig. 5(d) of the main manuscript for H(AuCl₄). The same calculations for WF were done for other samples as well.

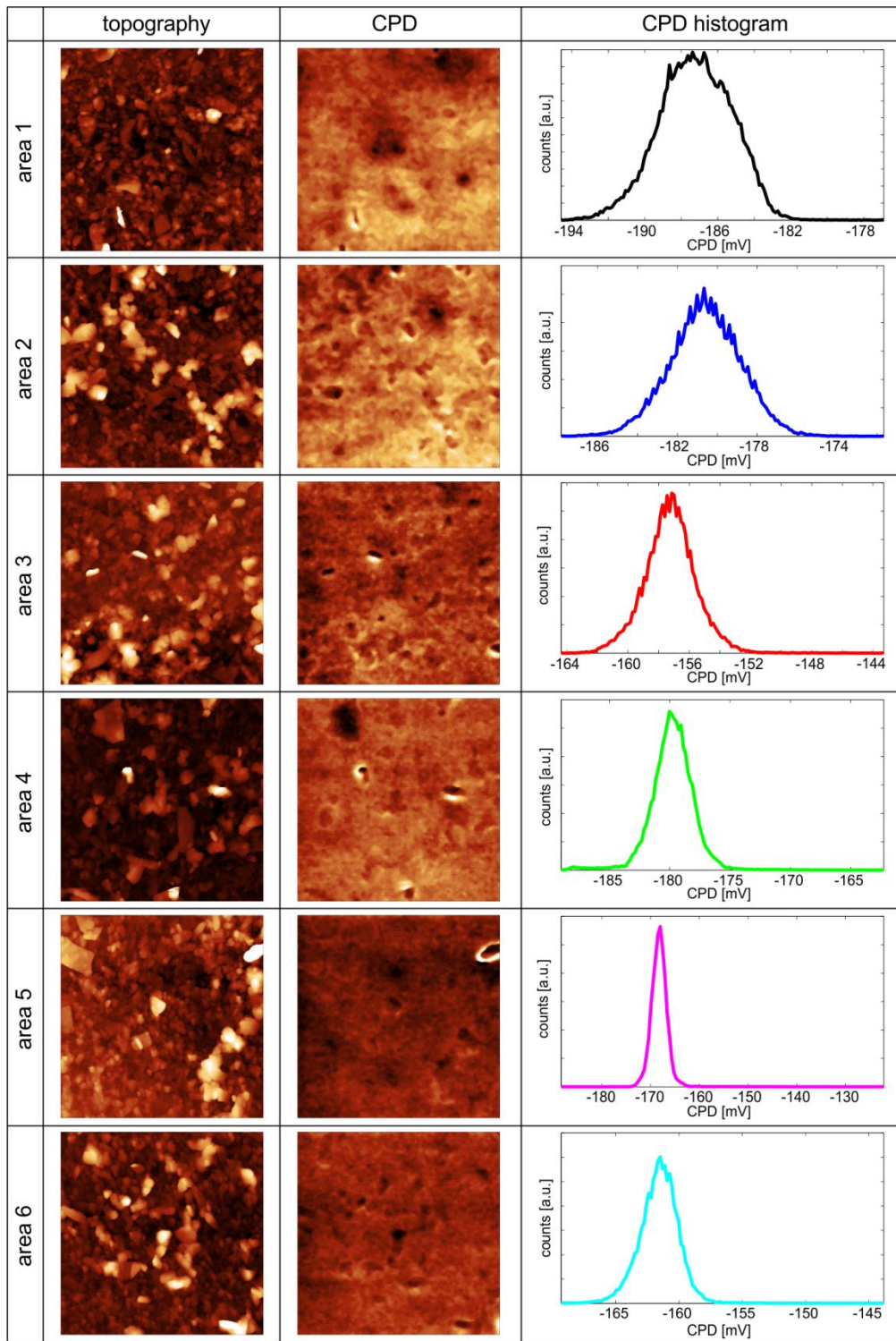


Figure S3: Topography, CPD maps and corresponding CPD histograms for six different $5 \times 5 \mu\text{m}^2$ areas of the LPE graphene film doped with $\text{H}(\text{AuCl}_4)$.

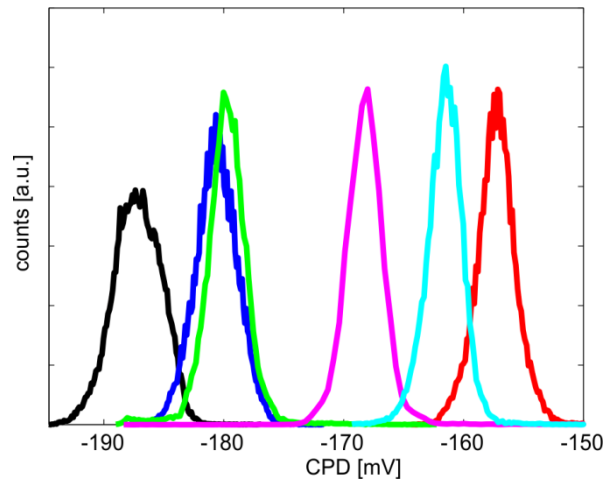


Figure S4: CPD histograms for six different $5 \times 5 \mu\text{m}^2$ areas of the LPE graphene film doped with $\text{H}(\text{AuCl}_4)$ from Figure S3.

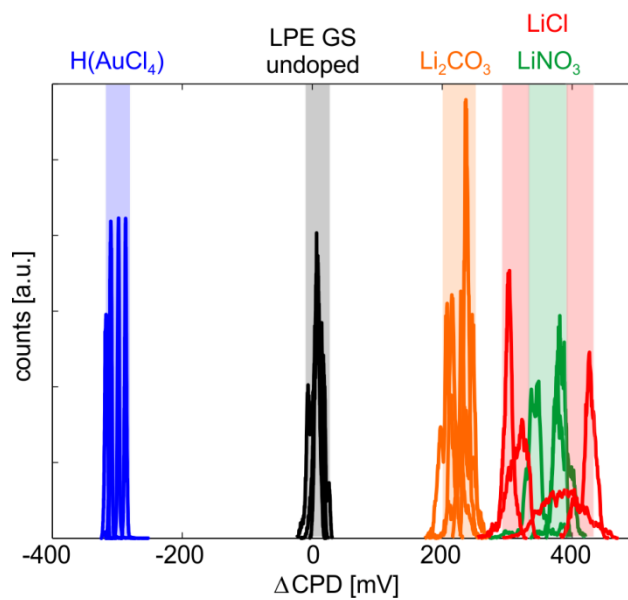


Figure S5: Measured distributions of CPD for doped LPE GS films for different dopants, with respect to the undoped LPE GS film taken as a reference



Article

Quiet Ionospheric D-Region (QIonDR) Model Based on VLF/LF Observations

Aleksandra Nina ^{1,*}, Giovanni Nico ^{2,3}, Srđan T. Mitrović ⁴, Vladimir M. Čadež ⁵, Ivana R. Milošević ¹, Milan Radovanović ^{6,7} and Luka Č. Popović ^{5,8,9}

- ¹ Institute of Physics Belgrade, University of Belgrade, 11080 Belgrade, Serbia; novovic@ipb.ac.rs
 - ² Istituto per le Applicazioni del Calcolo (IAC), Consiglio Nazionale delle Ricerche (CNR), 70126 Bari, Italy; g.nico@ba.iac.cnr.it
 - ³ Department of Cartography and Geoinformatics, Institute of Earth Sciences, Saint Petersburg State University (SPSU), 199034 Saint Petersburg, Russia; g.nico@spbu.ru
 - ⁴ Novelic, 11000 Belgrade, Serbia; mitar027@beotel.net
 - ⁵ Astronomical Observatory, 11060 Belgrade, Serbia; vcadez@aob.rs (V.M.Č.); lpopovic@aob.rs (L.Č.P.)
 - ⁶ Geographical Institute "Jovan Cvijić" SASA, 11000 Belgrade, Serbia; m.radovanovic@gi.sanu.ac.rs
 - ⁷ Institute of Sports, Tourism and Service, South Ural State University, 454080 Chelyabinsk, Russia; milan.georgaf@gmail.com
 - ⁸ Department of Astronomy, Faculty of Mathematics, University of Belgrade, 11000 Belgrade, Serbia; lpopovic@matf.bg.ac.rs
 - ⁹ Faculty of Science, University of Banja Luka, 78000 Banja Luka, Bosnia and Herzegovina; luka.popovic@pmg.unibl.org
- * Correspondence: sandrast@ipb.ac.rs



Citation: Nina, A.; Nico, G.; Mitrović, S.T.; Čadež, V.M.; Milošević, I.R.; Radovanović, M.; Popović, L.Č. Quiet Ionospheric D-Region (QIonDR) Model Based on VLF/LF Observations. *Remote Sens.* **2021**, *13*, 483. <https://doi.org/10.3390/rs13030483>

Academic Editor: Benedikt Soja
Received: 2 December 2020
Accepted: 26 January 2021
Published: 29 January 2021

Publisher's Note: MDPI stays neutral with regard to jurisdictional claims in published maps and institutional affiliations.



Copyright: © 2021 by the authors. Licensee MDPI, Basel, Switzerland. This article is an open access article distributed under the terms and conditions of the Creative Commons Attribution (CC BY) license (<https://creativecommons.org/licenses/by/4.0/>).

Abstract: The ionospheric D-region affects propagation of electromagnetic waves including ground-based signals and satellite signals during its intensive disturbances. Consequently, the modeling of electromagnetic propagation in the D-region is important in many technological domains. One of sources of uncertainty in the modeling of the disturbed D-region is the poor knowledge of its parameters in the quiet state at the considered location and time period. We present the Quiet Ionospheric D-Region (QIonDR) model based on data collected in the ionospheric D-region remote sensing by very low/low frequency (VLF/LF) signals and the Long-Wave Propagation Capability (LWPC) numerical model. The QIonDR model provides both Wait's parameters and the electron density in the D-region area of interest at a given daytime interval. The proposed model consists of two steps. In the first step, Wait's parameters are modeled during the quiet midday periods as a function of the daily sunspot number, related to the long-term variations during solar cycle, and the seasonal parameter, providing the seasonal variations. In the second step, the output of the first step is used to model Wait's parameters during the whole daytime. The proposed model is applied to VLF data acquired in Serbia and related to the DHO and ICV signals emitted in Germany and Italy, respectively. As a result, the proposed methodology provides a numerical tool to model the daytime Wait's parameters over the middle and low latitudes and an analytical expression valid over a part of Europe for midday parameters.

Keywords: ionosphere; D-region; VLF/LF signals; remote sensing; quiet conditions; modeling

1. Introduction

The ionosphere is the upper atmospheric layer that, due to its electrical properties, affects the propagation of electromagnetic waves [1,2]. This property is of high significance in many fields that include application of data obtained by different kinds of microwave signals (like the Global Navigation Satellite System (GNSS) [3–8] and Synthetic aperture radar (SAR) interferometry meteorology [9]), and both signal and ionospheric characteristics have influence on changes in signal propagation within this medium. For example, telecommunication signals emitted from the ground are affected by the ionosphere below

the signal reflection height, while satellite signals are primarily affected by the F-region due to the largest values of electron density in the altitude domain located in this region.

Research of ionospheric properties is a very complex task because of permanent influences coming from outer space and different terrestrial layers. For this reason, it is of crucial importance to include as many observational data as possible in their modeling. For example, although the unperturbed D-region has not visible influences on satellite signal propagation, the recent results presented in Reference [10] show the importance of inclusion of its effects during intensive disturbances that are not considered in existing models (see, for example, Reference [11–13]).

Application of the specific technique for remote sensing of the ionosphere depends on the altitude domain. In addition, the choice of a particular analysis methodology depends on temporal and spatial characteristics of the collected data. The remote sensing of the lower ionosphere based on the propagation of very low/low frequency (VLF/LF) radio signals is an effective means to collect continuous observations the covering areas. These signals can propagate several thousand kilometres within the Earth-ionosphere waveguide, and the global observational setup is based on numerous worldwide located transmitters, and receivers. The VLF/LF receivers have the possibility of simultaneous monitoring of several signals coming from different directions with time sampling shorter than 1 s. For this reason, the databases collected by a particular receiver contain information that can be used in analyses of local and global, short and long-term variations. Because of these properties, this type of remote sensing is used in studies of how many terrestrial and extraterrestrial phenomena influence the lower ionosphere and, consequently, the propagation of electromagnetic waves which can significantly be affected by the disturbed D-region [14–21].

There are several models for modeling the VLF/LF propagation in the Earth ionosphere waveguide, such as the Long-Wave Propagation Capability (LWPC) program [22], finite-difference time-domain (FDTD) method [23], coupled beams and effective complex impedance model [24], and Modfinder [25]. These models are used in many studies for determination of ionospheric parameters where characteristics of the considered area, the ionospheric state and properties of the analyzed disturbances affect the possibility of applying certain approximations. For example, during quiet conditions or during disturbances that do not affect the horizontal uniformity of the observed D-region it is possible to assume only altitude variations of the ionospheric plasma parameters, while, in the case of local disturbances caused by for example day-night transitions along the propagation path and lightnings, it is necessary to take into account both the vertical and horizontal variations of these parameters. The horizontal uniform ionosphere is analyzed in many papers using the LWPC and Modfinder models [10,26–31]. As an example, some localized perturbations of the ionosphere are considered in Reference [32]. FDTD method was used to model the day-night transitions along the propagation path (see, for example, Reference [23]). Effects of the geomagnetic field and its variations which can induce the need to include gyrotropy and anisotropy into account are most important in analyses of the high-latitude lower ionosphere, while, in the mid-latitude areas, effects of variations in the geomagnetic field should be taken into account during large geophysical disturbances of the Lithosphere-Atmosphere-Ionosphere-Magnetosphere system caused by large magnetic storms, hurricanes, etc. [24]. In this paper, we present a model of the daytime D-region parameters under quiet conditions which is based on data recorded in ionospheric remote sensing by VLF/LF signals and LWPC program that simulates their propagation. The chosen time period, in absence of local intensive geophysical disturbances (induced by, for example, solar terminator, lightnings, and hurricanes) which are followed by significant anisotropy, allows us to assume a horizontally uniform ionosphere. In addition, we consider mid- and low-latitude domains where influence of the magnetic field variations on the considered signals (the presented model is relevant for not too long propagation paths of VLF/LF signals which are reflected at altitudes below 76 km) is not significant under quiet conditions. To calculate the quiet D-region parameters, we also include into

the consideration the analysis of disturbances induced by solar X-ray flares during the mid-day period when the indicated approximations are also justified and already used in many previous studies [10,26–31]. This is possible because solar X-ray flares do not cause local disturbances and induce practically horizontally uniform perturbations, especially within not too large areas, during the mid-day period.

Modeling of the solar X-ray flare perturbed D-region based on data obtained in its remote sensing by the VLF/LF signals assumes two approximations: (1) the lower ionosphere is usually considered as a horizontal uniform medium, and (2) the parameters in quiet conditions are considered as known quantity in which values are determined in previous statistical studies that, generally, do not represent the considered periods and areas. As we already said, the first approximation is good for a not too long propagation path of the considered signal and for daytime periods of a few hours around midday (this period depends on the season) in absence of intensive local disturbances. However, the second approximation can significantly affect the modeling, and this task was a subject of several studies which focused attention on the electron density and Wait's parameters (the "sharpness" and signal reflection height). There are several methodologies used in these studies. They are based on the broad-band detection of radio atmospheric in periods of lightning activities and detection of the narrow-band VLF signals. A technique to measure the local mid-latitude daytime D-region parameters from the Earth-ionosphere waveguide mode interference pattern in spectra of radio atmospheric launched by lightning discharges, presented in Reference [33], is limited to periods of lightning activities. In the cases based on the analysis of narrow-band VLF signals, properties of modeling and necessary approximations which affect certainty of its applications strongly depend on geographical location of the considered transmitters and receivers. Namely, if the propagation path of the considered VLF signal is very long, as, for example, in the case of studies based on data recorded by receiver located in New Zealand from which transmitters are more than 10,000 km away [34–36], it is necessary to include changes in Wait's parameters along the length of the path [34,35]. These changes provide additional possibilities for errors in modeling due to necessary approximations and changes in the ionosphere due to periodical and sudden events. Of course, increasing the propagation path length induces more effects of local disturbances which also affect the model certainty. Analyses of more receivers and transmitters can reduce these problems. A procedure for these ionospheric parameters modeling is given in Reference [37], where data for three signals recorded by six receivers are considered. In the mentioned studies, related to the considered areas, there are presented dependencies of the daytime Wait's parameters on zenith angle during the solar maximum and minimum [34,35], on both zenith angle and local time [33], and dependencies of the signal reflection height on zenith angle for different seasons [35]. Expressions which provide dependencies of Wait's parameters on more variables (zenith angle, season, smoothed sunspot number, latitude, and geomagnetic field) is presented in Reference [38]. However, the equations related to calculation of the signal reflection height cannot be applied to the newer sunspot datasets because one of these equations includes the Zürich sunspot number which refers to production of the sunspot number before 1981.

All these problems and the importance of determination of the quiet D-region parameters for many technologies motivate us to develop a model of the D-region which can be applied to shorter signal paths which significantly reduces disadvantages induced by the long distance signal propagation, and that includes the influences of:

- long-term variations (about 11 years) in solar radiations during solar cycle;
- seasonal variations (due to Earth's revolution);
- daytime periodical changes; and
- sudden mid- and short-term influences

on the D-region properties. In other words, the aim of this study is to develop a procedure that will make it possible to take advantage of densely spaced VLF/LF transmitters and receivers, like those in Europe, to accurately model the D-region parameters in the area of interest and for the considered time period.

In this paper, we present the Quiet Ionospheric D-Region (QIonDR) model which provides a procedure for the determination of the D-region plasma parameters in quiet conditions using the VLF/LF observational data for the considered area in mid- and low-latitude domains, and the considered time period. The QIonDR model provides an analysis of the Wait's parameters "sharpness" and signal reflection height. Determination of these parameters is important because knowing them allows computation of the D-region electron density N and, consequently, many other parameters, using different models [28,31,33,34,39,40]. As a result, in this study we also show the modeled electron density. To visualize the QIonDR model output, we apply it to data for the DHO and ICV signals emitted in Germany and Italy, respectively, and recorded in Serbia.

The article is organized as follows. The proposed methodology is presented in Section 2, while the analyses of observations and events are given in Section 3. Application of the QIonDR model on the DHO and ICV signals recorded in Belgrade is shown in Section 4, and conclusions of this study are given in Section 5.

2. Methodology

In this section, we describe a methodology for modeling Wait's parameters β_0 and H'_0 and the electron density N_{e0} in the quiet ionospheric D-region. This methodology is based on data obtained by the VLF/LF remote sensing of this atmospheric layer, using two VLF/LF signals, and the satellite X-ray flux data needed to determine the periods of ionospheric disturbances induced by solar X-ray flares.

To model propagation of the VLF/LF signal, we use the LWPC program. It models characteristics of the chosen signal considering its propagation in the Earth-ionosphere waveguide. Properties of the bottom boundary are based on the Westinghouse Geophysics Laboratory conductivity map [41], while the upper boundary is characterized by a conductivity that may be specified by the user. In this paper, we used Wait's model of the ionosphere [42] which describes the horizontally homogeneous exponential conductivity profile by conductivity parameter ω_r :

$$\omega_r(h) = \omega_0^2(h)/\nu(h), \quad (1)$$

where $\omega_0(h)$ and $\nu(h)$ are the electron plasma frequency and effective electron-neutral collision frequency, respectively. The first parameter can be obtained from the electron density N_e ($\omega_0^2(h) \approx 3180N_e$), while dependency of the collision frequency ν on the altitude h is given by an approximative equation based on experimental data presented in Reference [43,44]:

$$\nu(h) = 1.82 \times 10^{11} e^{-0.15h}, \quad (2)$$

Finally, according to the obtained vertical profiles of ω_r shown in Reference [42], an approximative equation for this parameter is given in the following form:

$$\omega_r(h) = 2.5 \times 10^5 e^{\beta(h-H')}, \quad (3)$$

where the parameters β and H' are known as Wait's parameters and called "sharpness" and signal reflection height, respectively. These parameters are input parameters in the LWPC program. ω_r is used for calculation of the reflection coefficient (the phase of the reflection coefficient is referred to the level where $\omega_r = 2.5 \times 10^5 \text{ s}^{-1}$) which is also dependent on the magnetic field. In Reference [42], it is assumed that the geomagnetic field is purely transverse. This approximation is possible because, for arbitrary directions of propagations, it has been indicated that transverse component of the geomagnetic field is most important for reflection of VLF radio waves at highly oblique incidence. Finally, the reflection coefficient is used in a mode theory calculations, which are described in Reference [42]. The output of LWPC program are the modeled amplitude and phase for input parameters and observed signal. Detailed descriptions of the LWPC and Wait's

models are given in Reference [22,42], while their application in the QIonDR model is described in detail in this Section.

Figure 1 shows the work-logic of the proposed methodology. It is split in the following two procedures related to the time period of the analysis of ionospheric parameters: (1) the Midday procedure (MDP), and (2) the Daytime procedure (DTP), detailed in Sections 2.1 and 2.2, respectively.

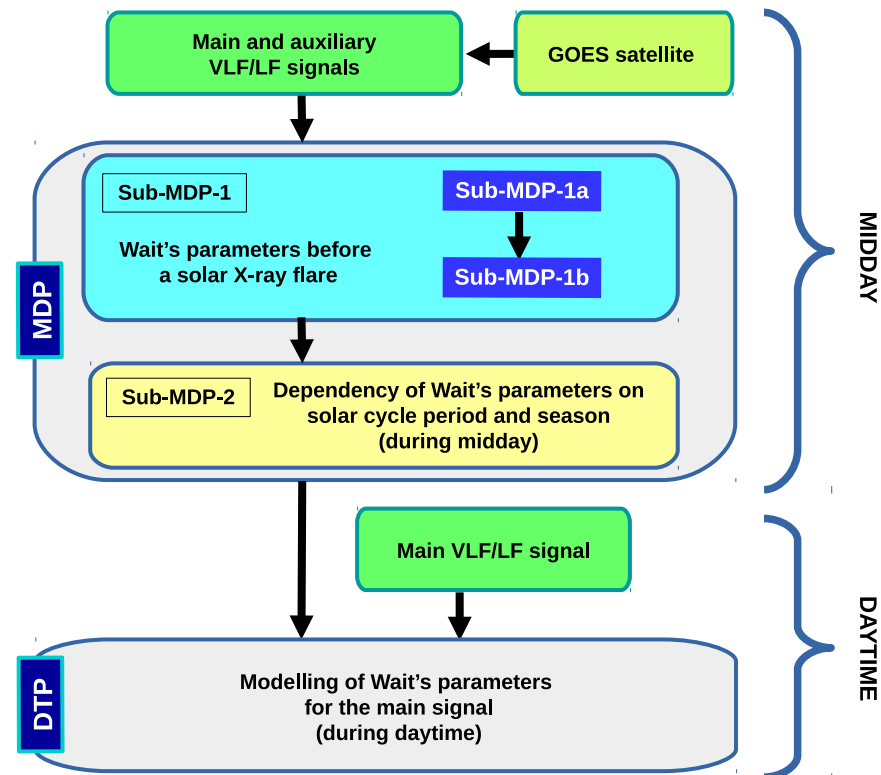


Figure 1. Diagram of the proposed methodology. It consists of two procedures, Midday procedure (MDP) and Daytime procedure (DTP), which are used for the midday and daytime periods. The VLF/LF signals and GOES data are given in input to MDP, which is split in two sub-procedures Sub-MDP-1, to estimate Wait's parameters before a solar X-ray flare, and Sub-MDP-2 to model the dependency of these parameters on the solar cycle period and season at midday. To a finer detail, Sub-MDP-1 is further split in Sub-MDP-1a and Sub-MDP-1b, corresponding to the analyses of a signal s and a disturbed state i of an X-ray flare XF, and determination of Wait's parameters in quiet conditions before a solar X-ray flare XF, respectively. DTP requires as input both the output of MDP and VLF/LF signals to model the daytime evolution of Wait's parameters.

2.1. Midday Periods

First, we analyze the changes in the midday ionospheric parameters induced by solar X-ray flares detected by the GOES satellite which occurred in midday periods. We process the recorded amplitudes and phases of both main and auxiliary VLF/LF signals in order to determine changes of these values at two different times during the solar X-ray flare influence with respect to their values before the disturbance (see Section 2.1.1). These changes are further used as input parameters in MDP (Section 2.1.2) which consists of two sub-procedures, first to determine Wait's parameters before a solar X-ray flare, and second to estimate the dependency of these parameters on the solar cycle period and season at the midday. The first sub-procedure is further split in Sub-MDP-1a and Sub-MDP-1b, corresponding to the analyses of a signal s and a disturbed state i of an X-ray flare XF (XF in general is notation for particular flare; as an example see Table 1), and the determination of Wait's parameters in the quiet conditions before a solar X-ray flare XF, respectively. The output of Sub-MDP-1 consists of Wait's parameters for all considered X-ray flares.

Their values are further fitted in Sub-MDP-2 which provides two functions describing the dependencies of Wait's parameters on the solar sunspot number and season. These two analytical expressions are the output of MDP, and they are used to model the daytime evolution of Wait's parameters in DTP using the amplitude and phase of VLF/LF signals (Section 2.2).

2.1.1. VLF/LF Signal Processing

When an X-ray flare occurs, the main and auxiliary VLF/LF signals are processed, taking both the amplitude and phase, in order to detect changes with respect to their values in quiet conditions before an X-ray flare. Figure 2 shows an example of temporal evolutions of signals' amplitude and phase, where their values in quiet and perturbed conditions are emphasized. These amplitude and phase values are needed in processing steps described in the following:

1. **Determination of the amplitude $A_0^{XF_s}$ of signal s in a quiet state before an X-ray flare XF.** To find this value for both VLF/LF signals, we consider three time bins of length Δt_{bin} (in our processing we use $\Delta t_{bin} = 20$ s) within a time window of a few minutes before the signal perturbation. The amplitude $A_0^{XF_s}$ is defined as the minimum of median values of recorded amplitudes in each bin, while the maximal absolute deviation of the recorded amplitudes in the considered bins from the median value is used as a figure for its absolute error $dA_0^{XF_s}$. In the following, we use "d" for the absolute error and " Δ " to denote the difference between the amplitudes at two different times during the disturbance and quiet state.
2. **Determination of the reference phase $P_{ref}^{XF_s}$ of a signal s during an X-ray flare XF.** The recorded phase of a VLF/LF signal represents the phase deviation of the considered signal with respect to the phase generated at the receiver. For this reason, the recorded phase has a component of constant slope that should be removed. A linear fit is performed through five points, three before the signal perturbation and two at the end of the considered observation interval, is performed. Phase values at these points are determined in the same way as in the procedure for amplitude estimation as described in point 1). For each time bin Δt , we compute the median value of phase samples. Furthermore, the largest deviation of phase values within each bin is used to estimate the absolute error $dP_{ref}^{XF_s}$ of the reference phase.
It is worth noting that disturbances induced by a solar X-ray flare can last from several tenth of minutes to over one hour. For this reason, quiet conditions can be different before and after disturbances. In addition, it is possible that some sudden events or some technical problem affect at least one signal in a time interval starting after the one used in this study. For instance, in Figure 2, we show a visible increase in the "quiet" visible increase in the "quiet" phase of about 15° and 5° for the DHO and ICV signals, respectively.
3. **Determination of differences in the amplitude $\Delta A^{XF_{si}}$ and phase $\Delta P^{XF_{si}}$ of the signal s during a disturbance induced by a solar X-ray flare XF in state i with respect to quiet conditions.** To avoid any dependence of results on the selection of time, we perform twice the analysis of changes in the signal parameters with respect to the initial, unperturbed state, by selecting two different times which are emphasized by vertical dashed and dotted lines in right panels in Figure 2 displaying time evolutions of the amplitude ($\Delta A^{XF_{si}} = A^{XF_s}(t_i) - A_0^{XF_s}$) and phase ($\Delta P^{XF_{si}} = P^{XF_s}(t_i) - P_{ref}^{XF_s}(t)$) changes for both signals during the disturbance induced by the solar X-ray flare occurred on 17 September 2015.
The absolute errors $dA^{XF_{s1}}$ and absolute errors $dA^{XF_{s2}}$ of amplitudes $A^{XF_{s1}}$ and $A^{XF_{s2}}$, and $dP^{XF_{s1}}$ and $dP^{XF_{s2}}$ of phases $P^{XF_{s1}}$ and $P^{XF_{s2}}$, respectively, are determined as for the quiet state, i.e.: (1) we calculate $A^{XF_{s1}}$, $A^{XF_{s2}}$, $P^{XF_{s1}}$ and $P^{XF_{s2}}$ as median values in two bins of width $\Delta t_{bin} = 20$ s around times t_1 and t_2 ; (2) we define absolute errors $dA^{XF_{s1}}$ and $dA^{XF_{s2}}$, and $dP^{XF_{s1}}$ and $dP^{XF_{s2}}$ in terms of maximal absolute deviations

of the corresponding quantities within the bins. The total absolute errors are obtained as follows:

$$d(\Delta A^{XFsi}) = dA_0^{XFsi} + dA^{XFsi}, \quad (4)$$

$$d(\Delta P^{XFsi}) = dP_{ref}^{XFsi} + dP^{XFsi}. \quad (5)$$

where $i = \{1, 2\}$.

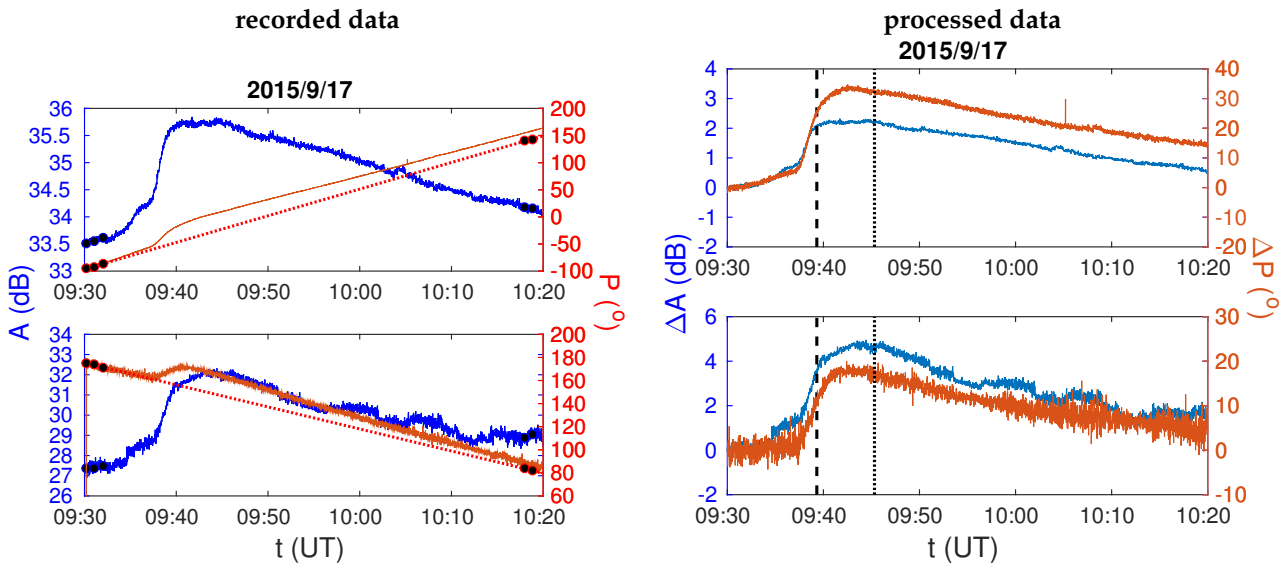


Figure 2. Time evolutions of the recorded amplitude and phase of DHO and ICV signals during the disturbance induced by the solar X-ray flare occurred on 17 September 2015 (left panels), and their deviations from the corresponding values in quiet conditions before the disturbance (right panels). The upper panels refer to the DHO signal, while the ICV signal data are shown in the bottom panels.

As a result of the above processing, the changes in amplitude and phase at the two times during the disturbance are obtained with respect to their values in quiet conditions.

2.1.2. Modeling

As shown in Figure 1, the procedure for modeling Wait's parameters describing the quiet conditions in midday periods (denoted with MDP in Figure 1) is split into two sub-procedures that provides estimations of: (1) their values for a particular event, and (2) their dependencies on the solar cycle period, described in terms of smoothed daily sunspot number σ , and season parameter $\chi = \text{DOY}/365$, where DOY is the day of year. Here, we approximate the tropical year lasting 365 days (instead 365.24255 days).

Sub-MDP-1: Estimation of Wait's parameters in quiet conditions before a solar X-ray flare.

As can be seen in Figure 1 this procedure consists of two following sub-procedures:

- **Sub-MDP-1a.** This sub-procedure provides values of Wait's parameters in the quiet ionosphere for which the amplitude ΔA_{mod}^{sqd} and phase ΔP_{mod}^{sqd} changes are similar to the corresponding recorded values, ΔA^{XFsi} and ΔP^{XFsi} , respectively. It is based on determination of changes in two sets of the modeled amplitude $\Delta A_{mod}^{sqd} = A_{mod}^{sd} - A_{mod}^{sq}$ and phase $\Delta P_{mod}^{sqd} = P_{mod}^{sd} - P_{mod}^{sq}$ of the signal s , and their deviations from the corresponding recorded values ΔA^{XFsi} and ΔP^{XFsi} for the signal s and disturbed state i . These sets, representing the modeled quiet and disturbed states, q and d , respectively, are performed in simulations of the considered VLF/LF signal propagation using LWPC numerical model developed by the Space and Naval Warfare Systems Center, San Diego, CA,

USA [22]. The input parameters of this numerical model are Wait’s parameters “sharpness” and signal reflection height, while the modeled amplitude and phase are its output (see the diagram in Figure 3).

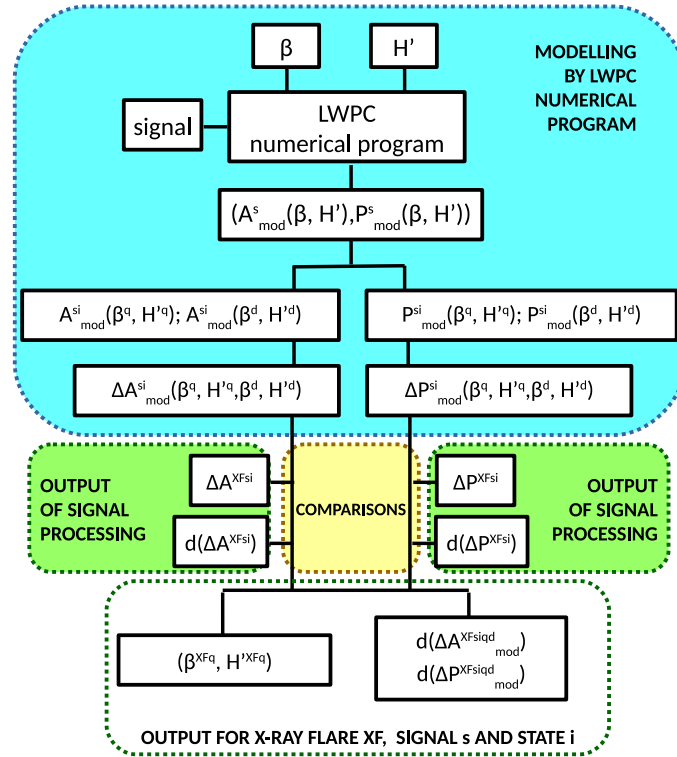


Figure 3. Diagram of sub-procedure MDP-1a.

According to the results presented in literature (see Reference [26,27,31,33–35]), Wait’s parameters can be considered within intervals 0.2 km^{-1} – 0.6 km^{-1} for β , and 55 km – 76 km for H' , where the quiet conditions can be described within intervals 0.2 km^{-1} – 0.45 km^{-1} for β^q , and 68 km – 76 km for H'^q . To model the parameter values representing a disturbed state d , β^d and H'^d , given those describing a quiet state q , we use conditions $\beta^q < \beta^d$ and $H'^q > H'^d$ which are based on many studies [26,27,31]. In the following, we use these intervals with steps of 0.01 km^{-1} and 0.1 km , respectively, as input in the LWPC numerical program.

The first output of the Sub-MDP-1a are the pairs of Wait’s parameters referring to the quiet state before a solar X-ray flare XF (β^{XFq}, H'^{XFq}) for which the LWPC model can calculate the amplitude and phase differences for both main (m) and auxiliary (a) signals ($s = m, a$) and for both disturbed state ($i = 1, 2$) that satisfy the conditions:

$$d(\Delta A_{\text{mod}}^{\text{XFsiqd}}) = \text{abs}(\Delta A_{\text{mod}}^{\text{sqd}} - \Delta A^{\text{XFsi}}) < d(\Delta A^{\text{XFsi}}), \quad \text{and} \quad (6)$$

$$d(\Delta P_{\text{mod}}^{\text{XFsiqd}}) = \text{abs}(\Delta P_{\text{mod}}^{\text{sqd}} - \Delta P^{\text{XFsi}}) < d(\Delta P^{\text{XFsi}}), \quad (7)$$

where $d(\Delta A^{\text{XFsi}})$ and $d(\Delta P^{\text{XFsi}})$ are the absolute errors in the recorded signal characteristics.

The second output of Sub-MDP-1a are errors in modeling, e.g., the absolute deviations of the modeled changes in the amplitude and phase from their recorded values: $d(\Delta A_{\text{mod}}^{\text{XFsiqd}})$ and $d(\Delta P_{\text{mod}}^{\text{XFsiqd}})$. Both outputs are used in Sub-MDP-1b.

- Sub-MDP-1b.** The goal of this sub-procedure is to find the pair of Wait’s parameters $(\beta_0^{XFmidday}, H_0^{XFmidday})$, from those (β^{XFq}, H^{XFq}) extracted in Sub-MDP-1a, which provides the best agreement between the modeled and measured amplitude and phase changes of the VLF/LF signals. To do that, we analyze both the observation and modeling absolute errors, i.e., $d(\Delta A^{XFsi})$ and $d(\Delta P^{XFsi})$, for observations and $d(\Delta A_{mod}^{XFsiqd})$ and $d(\Delta P_{mod}^{XFsiqd})$ for modeling. These values are used to quantify the observed w_{obs}^{XF} and modeled w_{mod}^{XFq} weights for each extracted pair of Wait’s parameters. Details about the estimations of these weights are provided in Appendix A, while an example of representation of the extracted pairs in the 2D Wait’s parameter space is shown in the left panel of Figure 4. Each pair of Wait’s parameters is represented as a point. The color of points describes their observation and modeling precisions. To find points (i.e., pairs of Wait’s parameters) which best model the amplitude and phase changes, the region around each candidate point is analyzed as follows. The weight of each point, describing the overall observation and modeling precisions, is computed as the product of observed and modeled weights, i.e., $w_{obs}^{XF} w_{mod}^{XFq}$.

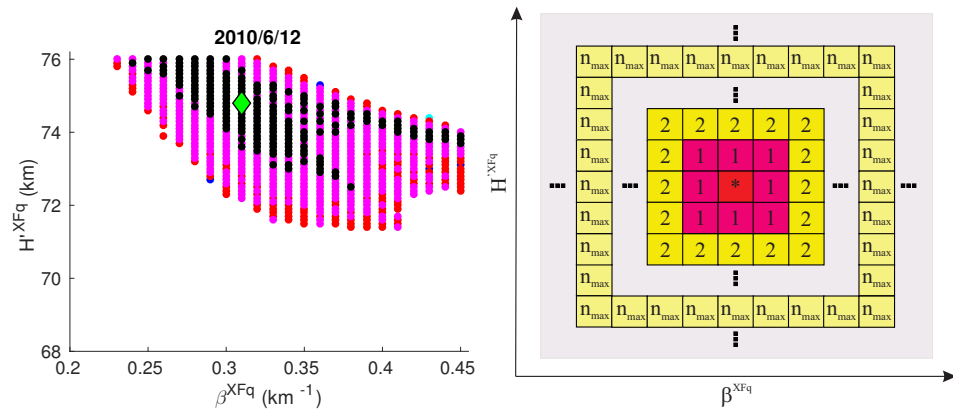


Figure 4. Left panel: Visualization of pairs of Wait’s parameters “sharpness” and signal reflection height (β^{XFq}, H^{XFq}) in quiet state q that satisfy conditions given by Equations (6) and (7) for an X-ray flare XF occurred on 12 June, 2010. The color of each point denotes the category of the corresponding pair. Each category includes pairs having all the four relative errors lower than $c \cdot 10\%$ (see Equation (A1)). Colors black, magenta, red, blue and cyan indicate the c -values increasing from 1 to 5 in steps of 1. The green diamond indicates the pair $(\beta_0^{XFmidday}, H_0^{XFmidday})$ which provides the best agreement of modeled and recorded amplitude and phase changes for the considered X-ray flare. Right panel: Region of Wait’s parameter space around the point “*” with the visualization of the neighbor system. The first neighbors ($n = 1$) are colored pink, the second ones ($n = 2$) orange, and the most distant neighbors considered in the procedure ($n = n_{max}$) are colored yellow.

Furthermore, the weight w_n^{XFq} is introduced to quantify the influence of each point within the region around the candidate point. This weight is defined as

$$w_n^{XFq} = \sum_k \left\{ \frac{1}{n^{qk}} w_{obs}^{XFk} w_{mod}^{XFk} \right\}, \tag{8}$$

where n^{qk} is the distance between the quiet states q and k which refer to pairs (β^{XFq}, H^{XFq}) and (β^{XFk}, H^{XFk}) , respectively.

The total weight w_{tot}^{XFq} for the pair (β^{XFq}, H^{XFq}) is computed as:

$$w_{tot}^{XFq} = w_{obs}^{XFq} w_{mod}^{XFq} + w_n^{XFq}. \tag{9}$$

Finally, the pair of Wait’s parameters $(\beta_0^{XFmidday}, H_0^{XFmidday})$ describing the quiet D-region before a solar X-ray flare XF, which provides the best agree-

ment of the considered modeled and observed amplitude and phase changes, is obtained as the pair with the largest total weight $W_{\text{tot}}^{\text{XF}} = \max_q \{w_{\text{tot}}^{\text{XFq}}\}$. The estimation errors $[e\beta_{0-}^{\text{XF}}, e\beta_{0+}^{\text{XF}}]$ and $[eH'_{0-}^{\text{XF}}, eH'_{0+}^{\text{XF}}]$ of these parameters are obtained from distribution of pairs $(\beta^{\text{XFq}}, H'^{\text{XFq}})$ which satisfy conditions (6) and (7). For instance, the error for $\beta_0^{\text{XFmidday}}$ are computed as follows. For the pair $(\beta_0^{\text{XFmidday}}, H'_0{}^{\text{XFmidday}})$ represented by green diamonds in Figure 4, the interval $[e\beta_{0-}^{\text{XF}}, e\beta_{0+}^{\text{XF}}]$ is estimated by taking the smaller and larger values of β^{XFq} estimates, for the given $H'_0{}^{\text{XFmidday}}$. In the same way, we estimate the error for $H'_0{}^{\text{XFmidday}}$.

Sub-MDP-2: Modeling of Wait's parameters in terms of sunspot number and season.

The aim of this subroutine is to model the behaviour of Wait's parameters by fitting the $(\beta_0^{\text{XFmidday}}, H'_0{}^{\text{XFmidday}})$ pair. This requires a deeper understanding of the X-ray influences on the D-region. During quiet conditions, the solar hydrogen Ly α radiation has a dominant influence on ionization processes in the ionospheric D-region (see, for example, Reference [45]). The intensity of this radiation varies periodically during the solar cycle and its variation depends on the sunspot number. Because of that, we use the smoothed daily sunspot number σ to represent the intensity of the incoming solar radiation in the Earth's atmosphere. The intensity of this radiation decreases with the solar zenith angle due to larger attenuations in the atmosphere above the considered locations. Generally, the zenith angle changes are due to seasonal and daily variations. However, this study focuses on time intervals around middays which allows us to assume that the seasonal changes represent the zenith angle variations. We introduce the seasonal parameter $\chi = \text{DOY}/365$ where DOY is the day of year. This parameter has values between 0 and 1. Some authors report on possible influences of the geomagnetic field on the Wait's parameter [38,46]. However, this is more pronounced at polar and near polar areas due to shapes of geomagnetic lines that allows charge particle influences on the ionospheric properties. As this study is focused on the low and mid latitude ionosphere, we neglect these effects.

Dependencies of Wait's parameters at midday on solar cycle and seasonal variations can be given as functions:

$$\beta_0^{\text{midday}} = f(\sigma, \chi) \quad (10)$$

and

$$H'_0{}^{\text{midday}} = g(\sigma, \chi). \quad (11)$$

These relations are not general and have yet to be determined for the location of interest and the time to which the recorded data refer to.

The knowledge of these functions allow us to calculate the vertical distribution of the Wait's horizontally uniform ionosphere, $N_{e0}(h, \sigma, \chi)$, using the equation given in Reference [34] for different values of σ and χ :

$$N_{e0}^{\text{midday}}(\sigma, \chi, h) = 1.43 \cdot 10^{13} e^{-\beta^{\text{midday}}(\sigma, \chi) H'^{\text{midday}}(\sigma, \chi)} e^{[\beta^{\text{midday}}(\sigma, \chi) - 0.15]h}, \quad (12)$$

where N_{e0}^{midday} and β^{midday} are given in m^{-3} and km^{-1} , respectively, and H'^{midday} and altitude h are given in km. This equation was used to determine the temporal $(H'_0(t, h))$ and energy $(H'_0(\epsilon, h))$ distributions of the D-region electron density perturbed by a solar X-ray flare (see, for example, Reference [31,47,48]).

2.2. Daytime Variations of Ionospheric Parameters

The determination of the daytime variation of Wait's parameters and electron density is based on the comparison of observational and modeling data as for the analysis of midday variations. However, the DTP procedure considers only one VLF/LF signal, e.g.,

the main one. The reason for that is that the approximation of a horizontally uniform ionosphere during the entire daytime period (far from the sunrise and sunset) can be used when the size of the observed area corresponds to a relatively short propagation path of the signal.

2.2.1. VLF/LF Signal Processing

The goal of this procedure is to find the amplitude and phase variations relative to their values in the midday period. We consider data recorded during the daytime period, far from the sunrise and sunset. The midday period is estimated from tendency of the amplitude time evolution $A(t)$. Namely, it rises until the midday and decreases afterwards which allows us to assume the period around the amplitude maximum as the midday period. The duration of this period is a few minutes and it depends on the season and possible existence of unperiodical disturbances which should be excluded from the analysis.

To exclude the short-term amplitude picks that do not represent periodic daily variations, the midday amplitude A^{midday} is estimated as the median amplitude value in the midday period.

Similarly to the analysis in Section 2.1.1, the time evolution of the phase is determined by estimating the linear phase trend obtained by interpolation of phase values estimated within time bins in quiet conditions. The midday phase P^{midday} is estimated from the obtained phase evolution $P(t)$ in the same way like for the midday amplitude.

The final step of this processing is the calculation of amplitude and phase deviations from their reference values, i.e., $\Delta A = A - A^{\text{midday}}$ and $\Delta P = P - P^{\text{midday}}$.

2.2.2. Modeling

The modeling of daytime temporal evolution of Wait's parameters is based on comparison of deviation of observational and modeled changes with respect to their midday values. The modeled midday values $A_{\text{mod}}^{\text{midday}}$ and $P_{\text{mod}}^{\text{midday}}$ are obtained from β_0^{midday} and H_0^{midday} , while the modeled amplitude A_{mod} and phase P_{mod} are outputs of the LWPC program for the given pair of Wait's parameters. Wait's parameters ($\beta(t)$, $H'(t)$) at time t are estimated as those that best satisfy the conditions

$$A - A^{\text{midday}} = A_{\text{mod}} - A_{\text{mod}}^{\text{midday}} \quad (13)$$

and

$$P - P^{\text{midday}} = P_{\text{mod}} - P_{\text{mod}}^{\text{midday}}. \quad (14)$$

Finally, the electron density $N_{e0}(t, \sigma, \chi)$ is obtained from Equation (15):

$$N_{e0}(t, h, \sigma, \chi) = 1.43 \cdot 10^{13} e^{-\beta(t, \sigma, \chi) H'(t, \sigma, \chi)} e^{(\beta(t, \sigma, \chi) - 0.15)h}, \quad (15)$$

where the parameters are given in the same units as in Equation (12).

3. Studied Area and Considered Events

To give an example of this model application, we apply it to data recorded in Belgrade in the lower ionosphere observations by the VLF signals emitted in Germany and Italy, while the information of the X-ray flares occurrences was taken from the website https://hesperia.gsfc.nasa.gov/goes/goes_event_listings/. For a better understanding of the presented procedure, we will first describe observations and then (in Section 4) we present the application of the model to the observed data.

3.1. Remote Sensing of Lower Ionosphere

The lower ionosphere observations are performed by two VLF signals of frequencies 23.4 kHz and 20.27 kHz emitted by the DHO transmitter in Germany (Rhauderfehn, 53.08 N, 7.61 E) and the ICV transmitter in Italy (Isola di Tavolara, 40.92 N, 9.73 E), respectively.

Amplitudes and phases of these signals are recorded by the AWESOME (Atmospheric Weather Electromagnetic System for Observation Modeling and Education) receiver [49] located in Belgrade, Serbia, which was a part of the Stanford/AWESOME Collaboration for Global VLF Research (<http://waldo.world/narrowband-data/>). The locations of the considered transmitters and receiver, as well as the propagation paths, are shown in Figure 5.

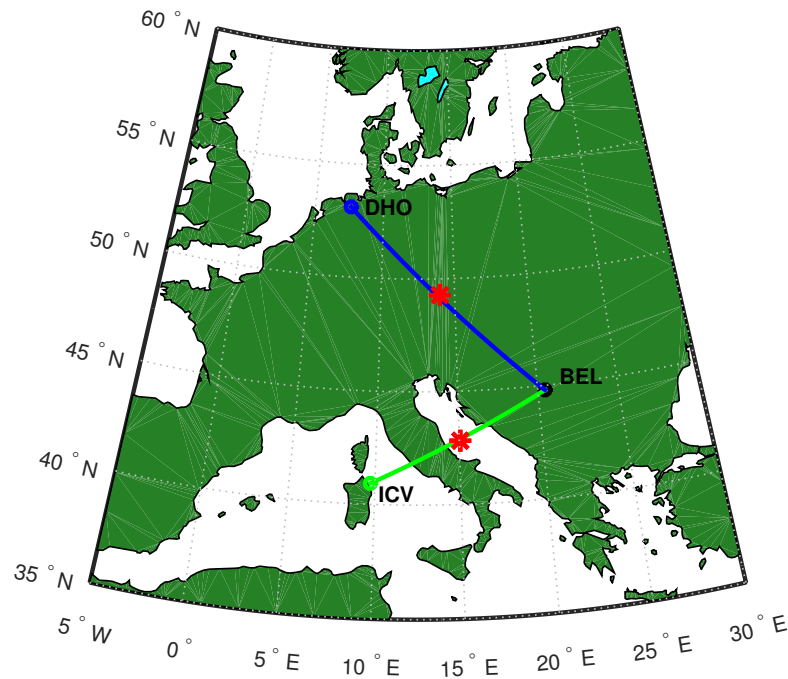


Figure 5. Propagation paths of the main and auxiliary VLF signals emitted by the DHO (Germany) and ICV (Italy) transmitters, respectively, and received in Belgrade (BEL). The stars indicate the locations of the path midpoints.

The best properties of the recorded VLF/LF signals in the Belgrade receiver station are those of the DHO signal. That can be explained by a not too long propagation path and a large emitted power (800 kW). This is why the DHO signal is used in many studies based on data collected by the Belgrade receiver station (see, for example, Reference [10,50]). Although the distance between the Italian transmitter and Belgrade receiver is shorter than the path in the first case, its emitted power is 40 times lower than that of the signal emitted in Germany. For this reason, we rank the DHO and ICV signals as the main and auxiliary ones, respectively.

3.2. Considered X-ray Flares

As one can see in Section 2, the presented model assumes a horizontally uniform Wait's ionosphere [42] for the area where both signals propagate. That assumption requires analyses of the time period when solar influences is similar above the considered part of Europe, e.g., periods around the midday. In addition, modeling of the electron density by the procedure given in Reference [34] is more appropriate for not too intensive flares. For this reason, we consider flares of up to class M5 (like in Reference [10]). Due to absence or insignificant ionospheric disturbances induced by low intensive flares, we consider events of classes larger than C5.0. In our collected database, we find 9 not too intensive events for which the differences in solar zenith angles, $\Delta\theta = \theta_{\text{DHO}} - \theta_{\text{ICV}}$ (calculated using the website <https://www.esrl.noaa.gov/gmd/grad/solcalc/azel.html> for the latitude/longitude points of the middle propagation paths DHO-BEL (49°16'48" N, 14°0'0" E) and ICV-BEL (42°48'36" N, 15°3'36" E), obtained in calculations by the program given at the website <https://www.gpsvisualizer.com/calculators>) satisfy the first mentioned condition. As

one can see in Table 1, classes of the considered flares are between C6.1 and M3.2, while differences in the solar zenith angles of the DHO and ICV signal mid-paths, θ_{DHO} and θ_{ICV} , respectively, are lower than 6.4° .

Table 1. Dates, times, and classes of the considered X-ray flares, and zenith angles θ_{DHO} and θ_{ICV} for the latitude/longitude points of the middle propagation paths DHO-BEL and ICV-BEL, respectively. Differences of these angles, $\Delta\theta$, are given in the last column. The positions of the considered VLF signal mid-paths, and corresponding angles θ_{DHO} , θ_{ICV} and $\Delta\theta$ are calculated using tools given at <https://www.gpsvisualizer.com/calculators> and <https://www.esrl.noaa.gov/gmd/grad/solcalc/azel.html>, respectively.

Flare XF	Date	Time (UT)	Flare Class	θ_{DHO} ($^\circ$)	θ_{ICV} ($^\circ$)	$\Delta\theta$ ($^\circ$)
F1	5 May 2010	11:37	C8.8	33.79	27.88	5.91
F2	12 June 2010	09:20	C6.1	35.39	31.25	4.14
F3	3 November 2014	11:23	M2.2	64.84	58.61	6.23
F4	15 November 2014	11:40	M3.2	53.57	51.35	2.22
F5	6 January 2015	11:40	C9.7	72.05	65.76	6.29
F6	21 January 2015	11:32	C9.9	69.25	62.88	6.37
F7	29 January 2015	11:32	M2.1	53.07	50.65	2.42
F8	17 Septembere 2015	09:34	M1.1	50.31	44.28	6.03
F9	14 May 2016	11:28	C7.4	37.50	35.31	2.19

4. Results and Discussion

The proposed methodology is applied to data obtained in observations described in Section 3. Here, we present the results of:

- Modeling the ionospheric parameters in midday periods over the part of Europe included within the location of transmitted signals (Sardinia, Italy, for the ICV signal) and (Lower Saxony, Germany for the DHO signal) and the receiver in Belgrade, Serbia, with respect to the daily smoothed sunspot number and season. This part consists of the following steps:
 - Modeling of pairs of Wait's parameters which satisfy conditions given by Equations (6) and (7) by the LWPC numerical program and determination pair (β_0^{XF} , H_0^{XF}) that provides the best fit of observational data for the considered X-ray flares.
 - Determination of dependencies of the midday Wait's parameters, β_0^{midday} and H_0^{midday} , and the electron density, N^{midday} , from parameters that describe the solar activity and Earth's motion: the smoothed daily sunspot number σ , and parameter χ describing seasonal variations.
- Modeling of daytime variations of ionospheric parameters for a particular day. This procedure consists of:
 - Modeling of time evolutions of Wait's parameters from comparisons of the recorded and modeled amplitude and phase changes with respect to their values in the midday.
 - Modeling of the electron density time evolution for the D-region heights during daytime.

For both analyses, it is necessary to know the modeled amplitude and phase of the considered signals. For this reason, we first present the description of their determination.

4.1. Modeling of the DHO and ICV Signal Amplitudes and Phases by the LWPC Numerical Program

As noticed in Section 2, the LWPC program simulates propagation of the VLF and LF signals from a particular transmitter to a particular receiver of these waves. Wait's

parameters, the “sharpness” β and signal reflection height H' are the input values for this program, while the modeled amplitude A_{mod} and phase P_{mod} are its outputs. In this study, we perform analysis for input values of β and H' in domains 0.2 km^{-1} – 0.6 km^{-1} and 55 km – 76 km , respectively, with corresponding steps of 0.01 km^{-1} and 0.1 km .

Results of modeling by the LWPC program for location of the Belgrade receiver and the DHO and ICV transmitters are shown in Figure 6. Here, it is important to pay attention to the fact that these panels represent the modeled amplitudes and phases (within the domain from -180° to 180°), while the procedure for comparison of recorded and modeled signal characteristics, described in Section 2.1.2, requires changes of these values in the disturbed with respect to quiet conditions. The dependencies of these changes on the input Wait’s parameters have the same distributions as the presented corresponding graphs because they have lower than those modeled by the LWPC program for a constant value of modeled amplitude or phase in quiet conditions.

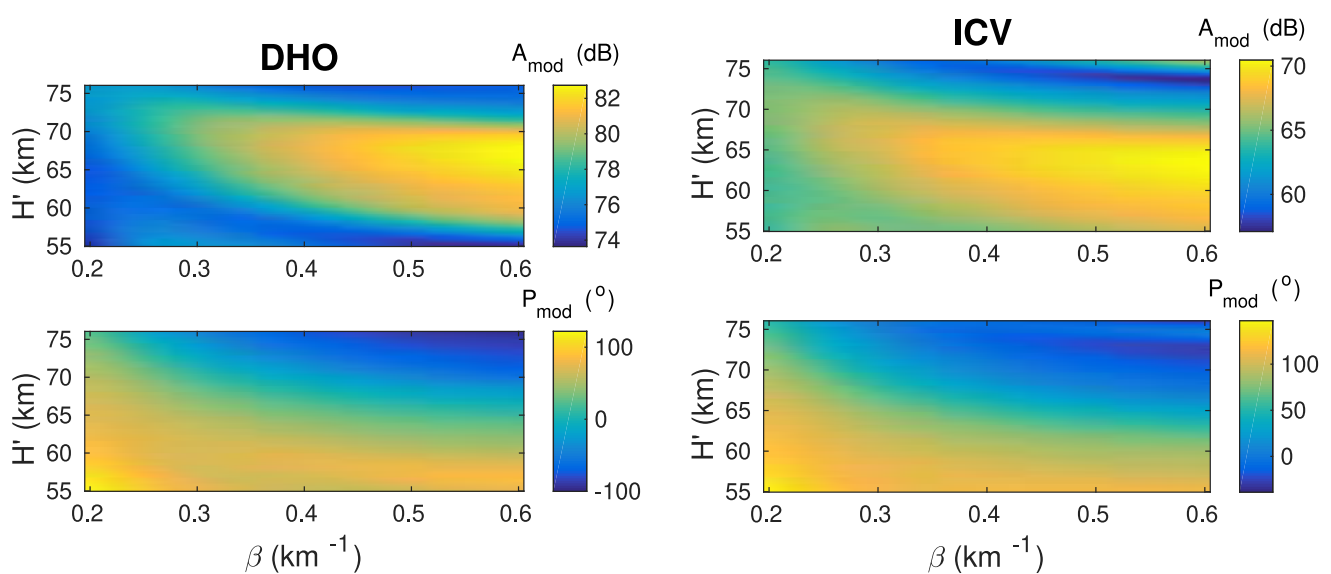


Figure 6. Surface plots of the modeled (by Long-Wave Propagation Capability (LWPC) program) amplitude (upper panels) and phase (lower panels) of the DHO (left panels) and ICV (right panels) signal for receiver located in Belgrade, Serbia, as functions of Wait’s parameters β and H' .

As one can see in Figure 6, there is no unique pair of Wait’s parameters that produce specific LWPC output values. That is why only one presented panel, even though the modeled amplitude/phase in quiet conditions are given, it cannot be used for determination of the input pair that provides the best fit of the observed data. The fact that it is impossible to determine a unique combination of Wait’s parameters from a single value of signal characteristic was noticed by other authors (see, e.g., Reference [36]).

4.2. Midday Values—Solar Cycle and Seasonal Variations

The procedure for determination of the considered midday values during the solar cycle and year consists of two parts:

- Determination of pairs $(\beta^{\text{XFq}}, H'^{\text{XFq}})$ which describe quiet states before the considered X-ray flares (Section 4.2.1).
- Determination of dependencies of Wait’s parameters and the electron density in midday quiet conditions on σ and χ (Section 4.2.2).

4.2.1. Determination of Pairs $(\beta^{\text{XFq}}, H'^{\text{XFq}})$

Comparison of the recorded and modeled changes in amplitude and phase of the DHO and ICV signals using the procedure described in Section 2.1.2 gives pairs of Wait parameters $(\beta^{\text{XFq}}, H'^{\text{XFq}})$ which satisfy the conditions given by Equations (6) and (7). These

values are presented for all considered events in Figure 7. To better visualize the precision in comparisons, we divide the extracted pairs in ten categories depending on relative errors in modeling of both amplitude and phase of the DHO and ICV signals. The category $c = 1, 2, 3, \dots, 10$ indicates that all relative errors defined by Equation (A1) for pairs (β^{XFq}, H'^{XFq}) have values less than $c \cdot 10\%$. The values of (β^{XFq}, H'^{XFq}) which have the largest total weight calculated by Equation (9), e.i. values $(\beta_0^{XFmiddy}, H_0^{XFmiddy})$ for a X-ray flare XF, are indicated by green diamonds.

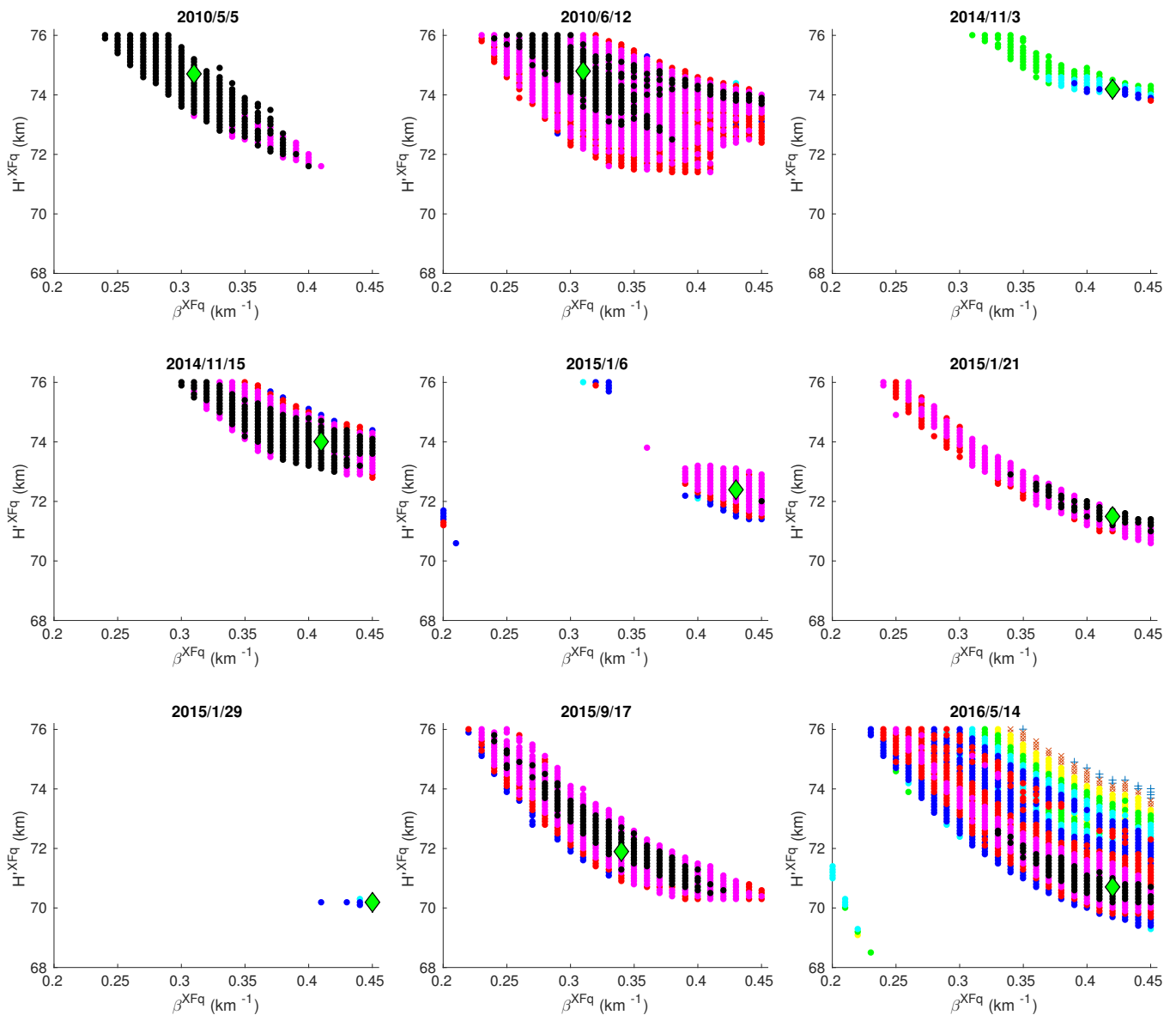


Figure 7. Visualization of pairs of Wait's parameters “sharpness” and signal reflection height (β^{XFq}, H'^{XFq}) in quiet state q that satisfy conditions given by Equations (6) and (7) for an X-ray flare XF that occurred on the date indicated on the corresponding panel (see Table 1). Categories $c = 1, 2, 3, \dots, 10$, describing relative errors defined by Equation (A1), are shown with different scatters: black, magenta, red, blue, cyan, green and yellow filled circles, x, +, and -, respectively. The pair (β^{XFq}, H'^{XFq}) which has the largest total weight calculated by Equation (9) for a particular event, i.e., value $(\beta_0^{XFmiddy}, H_0^{XFmiddy})$ for a X-ray flare XF, is indicated by green diamonds.

According to the number of neighbors (see Figure 7) that also satisfy the conditions given by Equations (6) and (7), stability of the obtained pairs $(\beta_0^{XFmiddy}, H_0^{XFmiddy})$ is good in 8 out of 9 cases. It can be also seen in Table 2 showing the relevant domains with higher $e\beta_{0+}^{XF}$ and eH_{0+}^{XF} , and lower $e\beta_{0-}^{XF}$ and eH_{0-}^{XF} values of Wait's parameters with

respect to $\beta_0^{XFm\text{midday}}$ and $H_0^{XFm\text{midday}}$ (for fixed other parameter), respectively. Visualization by different scatters shows that 6 cases have the highest precision of modeling for $c = 1$, while the lowest precision occurs for $c = 3$. The weights W_{tot}^{XF} , calculated by Equation (9) and given in Table 2, show large differences for the considered events (from 1.4 to 154.5).

Table 2. The obtained Wait’s parameters “sharpness”, $\beta_0^{XFm\text{midday}}$, and signal reflection height, $H_0^{XFm\text{midday}}$, and domains of their possible deviations going to larger ($e\beta_{0+}^{XF}$ and eH_{0+}^{XF}) and lower values ($e\beta_{0-}^{XF}$ and eH_{0-}^{XF}) for the considered flares. The last three columns show weights W_{tot}^{XF} of the determined pairs of Wait’s parameters ($\beta_0^{XFm\text{midday}}$, $H_0^{XFm\text{midday}}$), smoothed daily sunspot number σ , and seasonal parameter χ .

Flare XF No	$\beta_0^{XFm\text{midday}}$ (km ⁻¹)	$H_0^{XFm\text{midday}}$ (km)	$e\beta_{0+}^{XF}$ (km ⁻¹)	$e\beta_{0-}^{XF}$ (km ⁻¹)	eH_{0+}^{XF} (km)	eH_{0-}^{XF} (km)	W_{tot}	σ	χ
F1	0.31	74.7	0.01	0.04	0.5	1.4	104.0	10.7	0.3452
F2	0.31	74.8	0.08	0.06	1.2	2.6	103.5	23.1	0.4493
F3	0.42	74.2	0.03	0.03	0.3	0.2	5.6	100.5	0.8438
F4	0.41	74.0	0.04	0.05	0.9	0.9	154.5	100.1	0.8767
F5	0.43	72.4	0.02	0.03	0.7	0.9	29.7	112.6	0.0164
F6	0.42	71.5	0.01	0.03	0.2	0.5	56.8	87.6	0.0575
F7	0.45	70.2	0.00	0.02	0.1	0.1	1.4	84.8	0.0795
F8	0.34	71.9	0.04	0.04	1.1	1.0	115.9	54.0	0.7151
F9	0.42	70.7	0.03	0.06	3.6	1.0	111.5	68.6	0.3699

4.2.2. Wait’s Parameters and Electron Density in Quiet Conditions

The final step in determination of midday Wait’s parameters is analysis of their dependencies on daily smoothed solar sunspot number σ and seasonal variations described by parameter χ . To better visualize the difference due to larger solar radiation in the period around the maximum of the solar cycle than in the period around its minimum, we show the relevant points in Figure 8 with a filled and open scatters, respectively. Different seasons are described with blue (winter), green (spring), yellow (summer), and red (autumn) scatters.

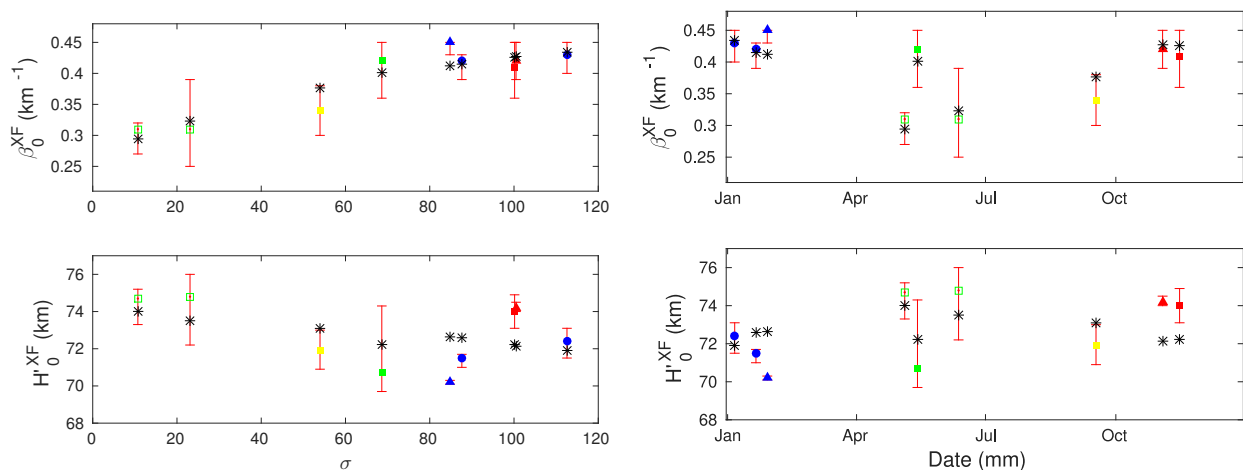


Figure 8. Dependencies of the “sharpness” β (upper panels) and signal reflection height H' on the smoothed daily sunspot number σ (left panels) and season (right panel). The modeled values $\beta_0^{XFm\text{midday}}$ and $H_0^{XFm\text{midday}}$ are shown as filled (for periods near the solar cycle maximum) and open (for periods near the solar cycle minimum) scatters. Different seasons are described by blue (winter), green (spring), yellow (summer), and red (autumn) scatters. Scatters marked by “*” indicate values obtained from Equations (16) and (17).

Dependencies of the midday Wait’s parameters on the solar sunspot number are shown in the left panels of Figure 8. Here, we consider the smoothed sunspot number (over 21 days) and take the value for the period of 20 days before and the considered day from the database given at <http://sidc.oma.be/silso/datafiles>. The upper panel indicates

the increase of the parameter β with σ , while decrease of the signal reflection height with σ is clearly shown in the bottom panel. These tendencies are in agreement with previous studies of Wait's parameters during solar X-ray flares where the increase/decrease of the "sharpness"/signal reflection height with the electron density is reported (see, for example, Reference [31]). In this case, the rise of the D-region electron density is a consequence of the Ly α radiation increase in approaching the solar cycle maximum. In fitting of these dependencies, we assume polynomial functions of the orders 2 and 1, respectively, which is by one order of magnitude larger than in Reference [38] where the dependency of the parameter β is given as a linear function of the sunspot number, while variation of H' with the sunspot number is not suggested. As one can see in the right panels in Figure 8, the seasonal variation is more complex than in the previous case. However, if two scatters related to the solar cycle minimum are excluded we can see approximative sinusoidal shapes in both cases. For this reason, we assume sinusoidal dependencies of Wait's parameters on parameter χ similarly as in Reference [38] but with daily (instead of monthly) changes and additional phase shifts which provide maximum/minimum values of β/H' for the summer solstice when the expected radiation coming in the considered area reaches its annual maximum.

Tow-dimensional fittings of Wait's parameters yield the following expressions:

$$\beta_0^{\text{midday}} = 0.2635 + 0.002573 \cdot \sigma - 9.024 \cdot 10^{-6} \sigma^2 + 0.005351 \cdot \cos(2\pi(\chi - 0.4712)) \quad (16)$$

and

$$H_0^{\text{midday}} = 74.74 - 0.02984 \cdot \sigma + 0.5705 \cdot \cos(2\pi(\chi - 0.4712) + \pi), \quad (17)$$

which provides good agreement of the computed Wait's parameters with their modeled values given in Table 1. The maximum differences of their values are less than 0.04 km^{-1} , and 2.5 km. These values are in good agreement with those obtained in Reference [51] for the night-time Wait's parameters and they are similar to the maximum "errors" given in Table 2. Wait's parameters are visualized in Figure 9 for β_0 (left panel) and H_0' (right panel). The obtained values lie in domains 0.31 km^{-1} – 0.45 km^{-1} and 70.6 km – 74.7 km , respectively. An increase/decrease in dependencies of the "sharpness"/reflection height with σ is visible during the whole year. The minimum/maximum values of β_0/H_0' for the same σ are reached during the summer solstice when the solar radiation has the greatest impact on the ionosphere.

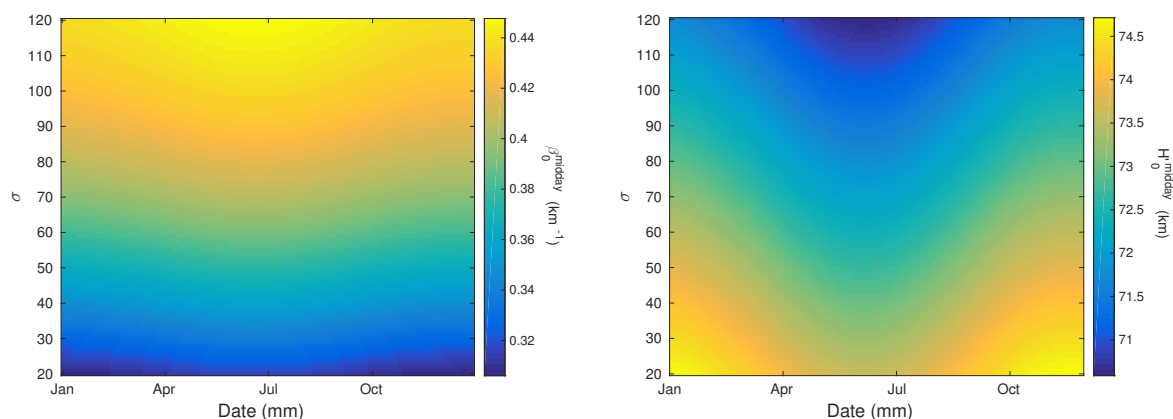


Figure 9. Dependencies of Wait's parameters in the quiet midday ionosphere, the "sharpness" β_0^{midday} (left panel) and signal reflection height H_0^{midday} (right panel) on season and smoothed daily sunspot number σ .

Introduction of Equations (16) and (17) in Equation (12) gives the midday electron density from σ and χ at altitude h . These dependencies at 70 km, 75 km, and 80 km are shown in Figure 10.

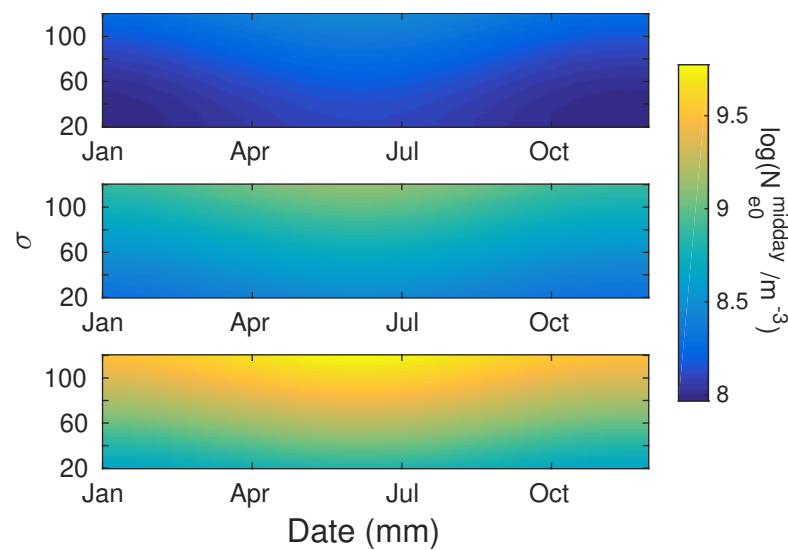


Figure 10. Dependencies of $\log(N_{e0}^{\text{midday}}/1\text{m}^{-3})$ at the altitudes of 70 km (upper panel), 75 km (middle panel), and 80 km (bottom panel) on season and smoothed daily sunspot number σ .

As one can see, variations are more visible at larger heights and can reach values near 10^{10} m^{-3} at 80 km for periods with large number of solar sunspot number. Due to the most intensive influences of solar radiation, the electron density has largest values during the summer solstice.

4.3. Daytime Variations

Knowing the midday Wait's parameters allows us to calculate their time evolutions during a quiet day. Here, we present an example using the DHO signal amplitude and phase recorded by the Belgrade VLF receiver on 6 September 2014 (DOY = 250; $\chi = 0.6849$) in which deviations, ΔA and ΔP , from the corresponding midday values are shown in the left panels of Figure 11. We consider a time interval from 9 UT to 15 UT when approximation of a horizontally uniform ionosphere within the medium where the signal propagates. A lack of data between 13 UT and 14 UT is due to a regular pause in the VLF/LF signals monitoring by the AWESOME receiver located in Belgrade.

To obtain the daytime evolution of β and H' , we first calculate their midday values. According to the database given at <http://sidc.oma.be/silso/datafiles>, the mean value of daily sunspot number for 20 days before and for the considered day is $\sigma = 107.1$. Introducing these values in Equations (16) and (17) gives the midday Wait's parameters for the analyzed day: $\beta_0^{\text{midday}} = 0.42 \text{ km}^{-1}$ and $H_0^{\text{midday}} = 72.5 \text{ km}$. The recorded midday amplitude $A_{\text{mod}}^{\text{midday}} = 30.35 \text{ dB}$ and phase $P_{\text{mod}}^{\text{midday}} = 1.11^\circ$ are estimated from time evolutions of the corresponding signal characteristics. Finally, the time evolution of Wait's parameters are calculated by the procedure as described in Section 2.2.2 and shown in the right panels of Figure 11. In the considered time period (excluding a short-term peak), these parameters have values within approximative domains 0.36 km^{-1} – 0.45 km^{-1} and 71.2 km – 74.2 km , respectively. Comparisons of the data obtained by the QIonDR model with those calculated by the LWPC default and IRI (see Reference [52] and references therein; Wait's parameters are calculated from electron density altitude distribution and expression for the electron density given in Reference [34]) models and with data presented in previous studies [27,33,35,53] show the best comparison of the QIonDR modeled amplitude and phase variations with the recorded ones. The QIonDR model fits better than the LWPC default model with data shown in Reference [27,33,35,53] for both Wait's parameters. The IRI model agrees better with the QIonDR ones for H'_0 , as well as in some periods for β_0 .

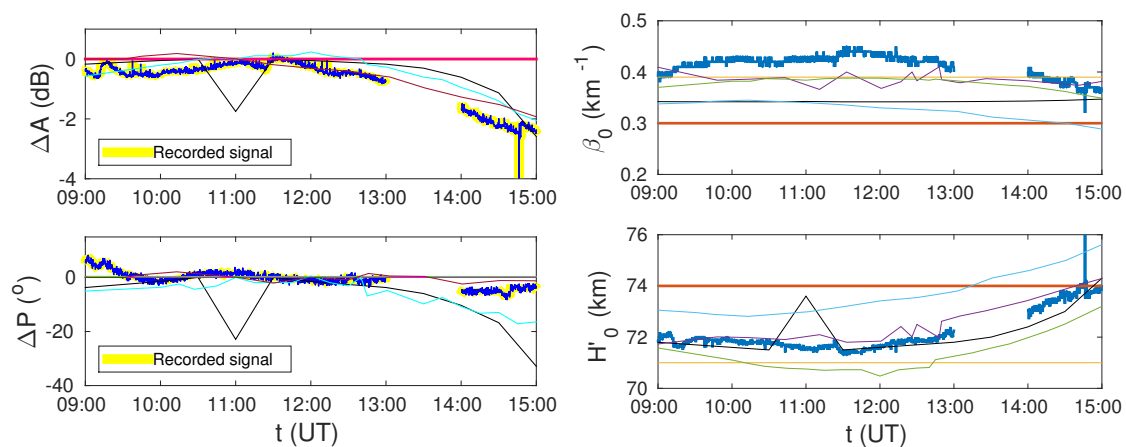


Figure 11. Daytime variations of the amplitude and phase changes (**left panels**) and Wait's parameters (**right panels**) during 6 September 2014 obtained by Quiet Ionospheric D-Region (QIonDR), default Long-Wave Propagation Capability (LWPC), and International Reference Ionosphere (IRI) models and compared with data presented in studies indicated in legend [22,27,33,35,52,53]. The gap between 13 UT and 14 UT is due to the one hour break in data receiving by the Atmospheric Weather Electromagnetic System for Observation Modeling and Education (AWESOME) receiver. — QIonDR; — LWPC default [22]; — IRI [52]; — Thomson et al., 2005 [27]; — Han et al., 2011 [33]; — McRae and Thomson, 2000 [35]; — Thomson et al., 2017 [53].

The daytime variation in the D-region electron density during the considered day, obtained from the calculated Wait's parameters and Equation (15), is shown in Figure 12. The time variation of electron density is more noticeable at higher altitudes while the vertical changes are most pronounced in the midday period. Similarly to the comparison of Wait's parameters, the QIonDR model fits better than the LWPC default model with data shown in Reference [27,33,35,53] for the electron density at 70 km and 80 km. The IRI model agrees better with the QIonDR ones for the electron densities at 70 km.

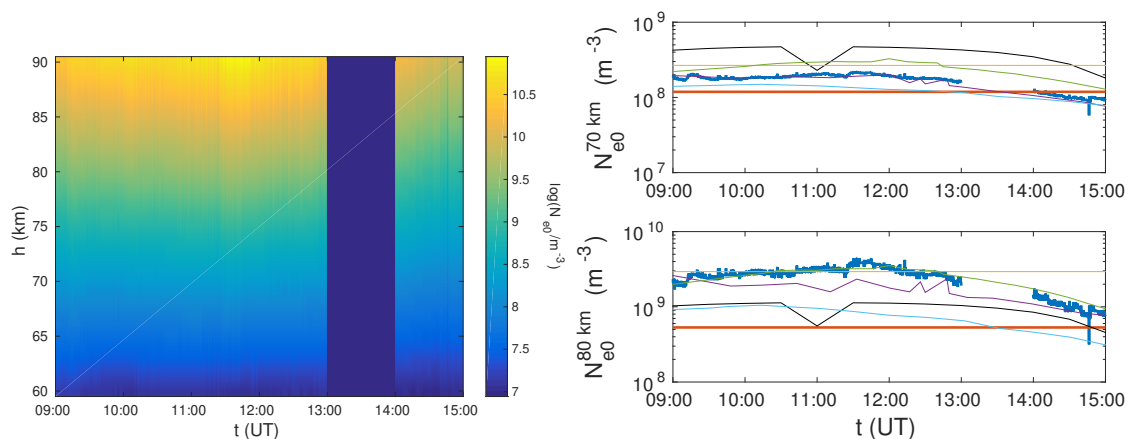


Figure 12. Left panel: Daytime variation of $\log(N_{e0}/1\text{m}^{-3})$ during 6 September 2014 obtained by the Quiet Ionospheric D-Region (QIonDR) model. The gap between 13 UT and 14 UT is due to the one hour break in data receiving by the Atmospheric Weather Electromagnetic System for Observation Modeling and Education (AWESOME) receiver. Right panels: Comparisons of the obtained electron density time evolutions at 70 km (upper panel) and 80 km (bottom panel) with those obtained for Wait's parameters presented in Figure 11. — QIonDR; — LWPC default [22]; — IRI [52]; — Thomson et al., 2005 [27]; — Han et al., 2011 [33]; — McRae and Thomson, 2000 [35]; — Thomson et al., 2017 [53].

A similar analysis is provided also for the D-region disturbed by a solar X-ray flare on 17 September 2015 (signal characteristics for this event are shown in Figure 2). Comparisons of the amplitude and phase changes, as well as time evolutions of Wait's parameters and the electron density for different values of initial Wait's parameters, are shown in Figure 13. In these calculations, we applied the LWPC model for the initial Wait's parameters obtained

by the QIonDR, LWPC default, and IRI models, and based on the studies presented in Reference [27,35,53]. In all these cases, the modeled amplitude and phase variations are in very good agreement with the recorded ones. For better visibility, we show only the obtained data for the QIonDR and LWPC default models. As one can see in Figure 13a, they are practically completely fitted with the recorded data except for the end of the observed period when minor deviations are noticeable in the case of LWPC default program for the amplitude changes. Agreement of β is better for QIonDR than for the LWPC default model with data obtained by IRI model and data from Reference [27,35], as well as for data from Reference [53], in some periods. In the cases of H' and electron density time evolutions, the QIonDR better fits with data obtained for initial parameters calculated by the IRI model, used in Reference [27], and, in some periods, for initial parameters given in Reference [35]. In addition, comparison of all parameters is in better agreement for the QIonDR than LWPC default model with data presented in Reference [26,29] for the maximum X-radiation flux of flares of the same or very similar class as the considered one.

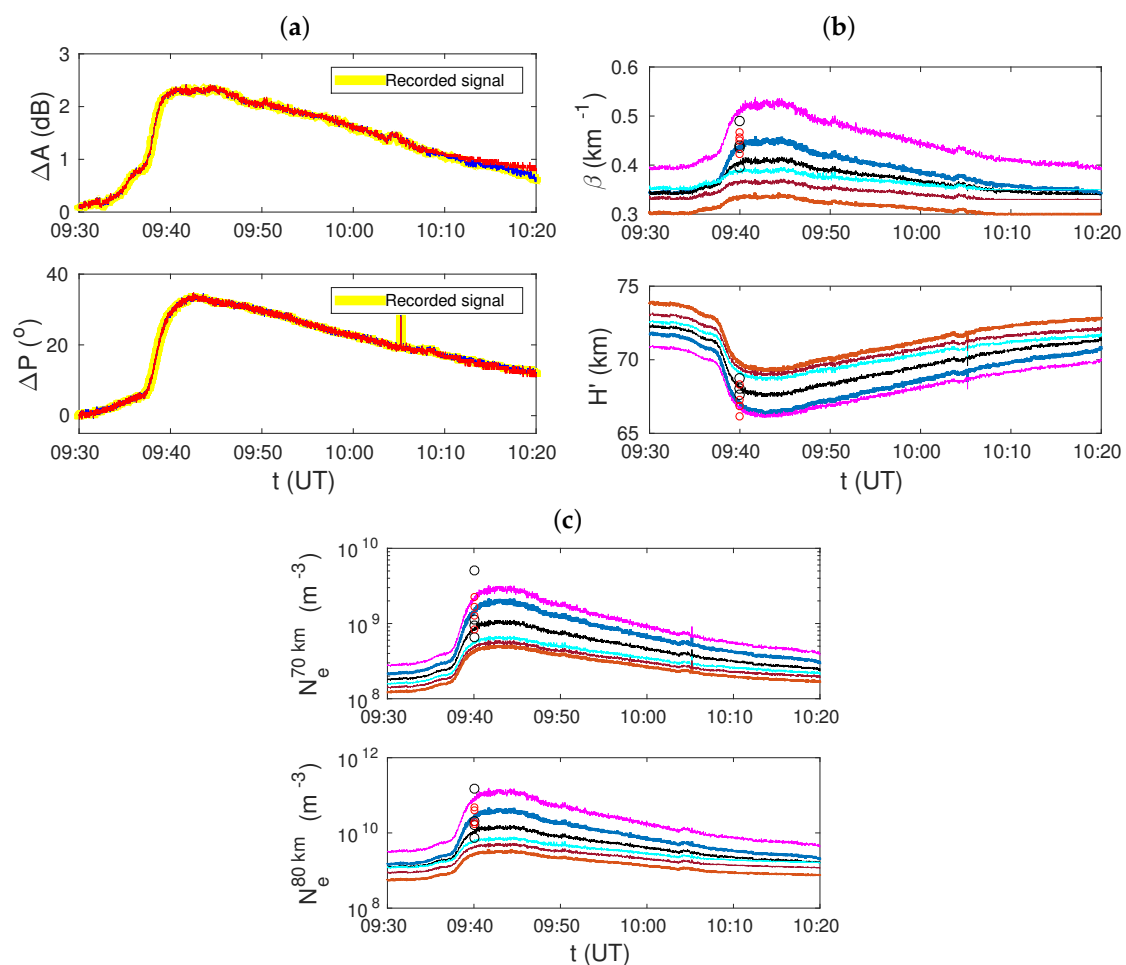


Figure 13. Comparisons for the D-region disturbed by a solar X-ray flare on 17 September 2015. (a) Comparisons of time evolutions of the recorded amplitude (upper panel) and phase (lower panel) changes with their modeled values by the Long-Wave Propagation Capability (LWPC) model for Wait's parameters β_0 and H'_0 determined by the Quiet Ionospheric D-Region (QIonDR) model (blue line) and by default (red line). (b) Comparison of time evolutions of Wait's parameters β and H' obtained by the LWPC program for their initial values modeled by the QIonDR, LWPC default and International Reference Ionosphere (IRI) models, and those presented in literature indicated in the legend [22,27,35,52,53]. The values obtained in Reference [26,29] at the moment of maximum X-radiation flux for flares of the same or very similar class as the considered one are shown by scatters. (c) Comparison of time evolutions of the electron density at 70 km (upper panel) and 80 km (bottom panel) for Wait's parameters shown in graph (b). — QIonDR; — LWPC default [22]; — IRI [52]; — Thomson et al., 2005 [27]; — McRae and Thomson, 2000 [35]; — Thomson et al., 2017 [53]; o Grubor et al., 2008 [29]; o McRae and Thomson, 2004 [26].

5. Conclusions

In this paper, we present a procedure for calculations of the D-region plasma parameters during quiet conditions. The proposed methodology is applied to areas monitored by the VLF/LF radio signals emitted and recorded by relatively closely located transmitters and receivers like, for example, in Europe. It is based on two different VLF/LF signals acquired by one receiver. We applied the proposed methodology to the DHO and ICV signals emitted in Germany and Italy, respectively, and recorded in Serbia. The obtained results of this study are:

- A new procedure for estimation of Wait's parameters and electron density. It is divided in two parts: (1) determination of dependencies of these parameters on the smoothed daily sunspot number and season at midday, and (2) determination of time evolution of these parameters during daytime;
- Estimation of Wait's parameters and electron density over the part of Europe included within the location of the transmitted signals (Sardinia, Italy, for the ICV signal) and (Lower Saxony, Germany for the DHO signal) and the receiver in Belgrade, Serbia. The obtained results show variations in which inclusion in different analyses of more events or time periods will allow more realistic comparisons and statistic studies;
- Analytical expressions for dependencies of Wait's parameters on the smoothed daily sunspot number and seasonal parameter valid over the studied area.

The determination of the "sharpness" β and signal reflection height H' during quiet conditions are needed for calculations of the electron density and other plasma parameters in the D-region during both the quiet and disturbed conditions. As a consequence, a more realistic modeling of the D-region can be attained based on results obtained by the proposed methodology. This could benefit to statistical analyses of the D-region related to different unperturbed conditions subject to daily and seasonal variations, as well as variations during a solar cycle. Furthermore, the most accurate modeling of the D-region based on the results obtained by the proposed methodology could also improve the mitigation of ionospheric propagation artefacts in telecommunication and microwave Earth Observation applications.

Due to approximation of the horizontally uniform ionosphere and neglect of influence of geomagnetic field variations on the VLF/LF signal propagation, application of the presented model is limited to:

- Time periods during quiet conditions or during disturbances that do not affect the assumed horizontal uniformity of the observed D-region (for example, the midday periods during the influence of solar X-ray flares),
- VLF/LF signals in which propagation paths between transmitters and receivers are relatively short, and
- Mid- and low-latitude areas where the spatial variations of the magnetic field are not significant in the given conditions.

In other words, the presented model cannot be used when losses, gyrotropy and anisotropy in the region of 70–90 km can significantly affect the propagation of VLF/LF signals in the waveguide Earth-Ionosphere, in particular in situations of large geophysical disturbances of the Lithosphere-Atmosphere-Ionosphere-Magnetosphere system caused by large magnetic storms, hurricanes, etc.

The proposed methodology can be applied during the daytime period when the solar influence on the ionosphere is the largest. During this period the electron density can significantly rise due to influence of intensive sudden solar phenomena like a solar X-ray flare, which can further importantly affect propagation of the mentioned electromagnetic waves.

It is worth noting that the proposed methodology can be applied only to relatively small areas like the one studied in this paper. For this reason, it is more relevant for Europe characterized by a high density network of VLF/LF transmitters and receivers. Improvements of the receiver and/or transmitter networks in future will make the application of

the proposed methodology more interesting in providing a real to near-real-time mapping of the D-region electron density above more regions around the world.

Author Contributions: Conceptualization, A.N.; methodology, A.N.; software, A.N. and S.T.M.; validation, G.N., L.Č.P., V.M.Č., S.T.M., I.R.M., and M.R.; formal analysis, A.N., G.N., V.M.Č., and L.Č.P.; investigation, A.N.; resources, A.N.; data curation, A.N. and S.T.M.; writing—original draft preparation, A.N.; writing—review and editing, all authors; visualization, A.N. and I.R.M.; funding acquisition, M.R. and A.N. All authors have read and agree to the published version of the manuscript.

Funding: The authors acknowledge funding provided by the Institute of Physics Belgrade and the Astronomical Observatory (the contract 451-03-68/2020-14/200002) through the grants by the Ministry of Education, Science, and Technological Development of the Republic of Serbia.

Data Availability Statement: Publicly available datasets were analyzed in this study. This data can be found here: https://hesperia.gsfc.nasa.gov/goes/goes_event_listings/; <https://www.gpsvisualizer.com/calculators>; <https://www.esrl.noaa.gov/gmd/grad/solcalc/azel.html>; <http://sidc.oma.be/silso/datafiles>; https://ccmc.gsfc.nasa.gov/modelweb/models/iri2012_vitmo.php.

Acknowledgments: The authors thank Frédéric Clette for help in preparation of our study and anonymous reviewers for very useful suggestions and comments. For visualization of the signal propagation paths, authors use website and for calculations the solar zenith angles website . The used daily sunspot numbers can be find at . The data for IRI model can be find at . Requests for the VLF data used for analysis can be directed to the corresponding author.

Conflicts of Interest: The authors declare no conflict of interest.

Sample Availability: The VLF data used for analysis is available from the corresponding author.

Appendix A

In this appendix, we provide details of determination of the observational, w_{obs}^{XF} , and modeled, w_{mod}^{XFq} , weights described in Section 2.1.2. Changes in the signal amplitude and phase can differ by more than one order of magnitude. For this reason, and also due to different unit of amplitude and phase measurements, in the following, we introduce relative errors of these changes. The observation and modeling weights are defined as follows:

- **Weight w_{obs}^{XF} .** The relative errors of the recorded signal amplitude and phase are obtained as a ratio of their absolute errors and the corresponding observed changes:

$$\delta(\Delta A^{XFsi}) = \frac{d(\Delta A^{XFsi})}{\Delta A^{XFsi}}; \quad \delta(\Delta P^{XFsi}) = \frac{d(\Delta P^{XFsi})}{\Delta P^{XFsi}}. \quad (A1)$$

The total relative error δ_{obstot}^{XF} of the observed changes related to a solar X-ray flare XF is given by:

$$\delta_{obstot}^{XF} = \sum_s \sum_i \left[\delta(\Delta A^{XFsi}) + \delta(\Delta P^{XFsi}) \right]. \quad (A2)$$

The observational weight for an X-ray flare XF is defined as reciprocal value of the total relative error:

$$w_{obs}^{XF} = \frac{1}{\delta_{obstot}^{XF}}. \quad (A3)$$

- **Weight w_{mod}^{XFq} .** This weight is computed for Wait's parameters in a quiet state q for which AT LEAST one corresponding pair (β^{XFd}, H'^{XFd}) is such that Equations (6) and (7) are satisfied for both signals s and both states i. In the case there are more pairs (β^{XFd}, H'^{XFd}) with the quiet state q, the relative error δ_{modtot}^{XFq} is defined as:

$$\delta_{modtot}^{XFq} = \min_d \left\{ \sum_s \sum_i \left[\delta(\Delta A_{mod}^{XFsiqd}) + \delta(\Delta P_{mod}^{XFsiqd}) \right] \right\}. \quad (A4)$$

The modeled weight is calculated as:

$$w_{\text{mod}}^{\text{XFq}} = \frac{1}{\delta_{\text{modtot}}^{\text{XFq}}}. \quad (\text{A5})$$

References

- Kintner, P.M.; Ledvina, B.M. The ionosphere, radio navigation, and global navigation satellite systems. *Adv. Space Res.* **2005**, *35*, 788–811.
- Meyer, F. Performance requirements for ionospheric correction of low-frequency SAR data. *IEEE Trans. Geosci. Remote Sens.* **2011**, *49*, 3694–3702.
- Jakowski, N.; Stankov, S.M.; Klaehn, D. Operational space weather service for GNSS precise positioning. *Ann. Geophys.* **2005**, *23*, 3071–3079.
- Benevides, P.; Nico, G.; Catalão, J.; Miranda, P.M.A. Bridging InSAR and GPS Tomography: A New Differential Geometrical Constraint. *IEEE Trans. Geosci. Remote Sens.* **2016**, *54*, 697–702.
- Benevides, P.; Nico, G.; Catalão, J.; Miranda, P.M.A. Analysis of Galileo and GPS Integration for GNSS Tomography. *IEEE Trans. Geosci. Remote Sens.* **2017**, *55*, 1936–1943.
- Su, K.; Jin, S.; Hoque, M.M. Evaluation of Ionospheric Delay Effects on Multi-GNSS Positioning Performance. *Remote Sens.* **2019**, *11*, 171.
- Yang, H.; Yang, X.; Zhang, Z.; Sun, B.; Qin, W. Evaluation of the Effect of Higher-Order Ionospheric Delay on GPS Precise Point Positioning Time Transfer. *Remote Sens.* **2020**, *12*, 2129.
- Farzaneh, S.; Forootan, E. A Least Squares Solution to Regionalize VTEC Estimates for Positioning Applications. *Remote Sens.* **2020**, *12*, 3545.
- Miranda, P.M.A.; Mateus, P.; Nico, G.; Catalão, J.; Tomé, R.; Nogueira, M. InSAR Meteorology: High-Resolution Geodetic Data Can Increase Atmospheric Predictability. *Geophys. Res. Lett.* **2019**, *46*, 2949–2955.
- Nina, A.; Nico, G.; Odalović, O.; Čadež, V.; Drakul, M.T.; Radovanović, M.; Č. Popović, L. GNSS and SAR Signal Delay in Perturbed Ionospheric D-Region During Solar X-ray Flares. *IEEE Geosci. Remote Sens. Lett.* **2020**, *17*, 1198–1202.
- Zhao, J.; Zhou, C. On the optimal height of ionospheric shell for single-site TEC estimation. *GPS Solut.* **2018**, *22*, 48.
- Nava, B.; Coïsson, P.; Radicella, S. A new version of the NeQuick ionosphere electron density model. *J. Atmos. Solar-Terr. Phys.* **2008**, *70*, 1856–1862.
- Scherliess, L.; Schunk, R.W.; Sojka, J.J.; Thompson, D.C.; Zhu, L. Utah State University Global Assimilation of Ionospheric Measurements Gauss-Markov Kalman filter model of the ionosphere: Model description and validation. *J. Geophys. Res.-Space* **2006**, *111*, 1–19.
- Silber, I.; Price, C. On the Use of VLF Narrowband Measurements to Study the Lower Ionosphere and the Mesosphere–Lower Thermosphere. *Surv. Geophys.* **2017**, *38*, 407–441.
- Nina, A.; Pulnits, S.; Biagi, P.; Nico, G.; Mitrović, S.; Radovanović, M.; Č. Popović, L. Variation in natural short-period ionospheric noise, and acoustic and gravity waves revealed by the amplitude analysis of a VLF radio signal on the occasion of the Kraljevo earthquake ($M_w = 5.4$). *Sci. Total Environ.* **2020**, *710*, 136406.
- Kumar, S.; NaitAmor, S.; Chanrion, O.; Neubert, T. Perturbations to the lower ionosphere by tropical cyclone Evan in the South Pacific Region. *J. Geophys. Res. Space* **2017**, *122*, 8720–8732.
- Nina, A.; Radovanović, M.; Milovanović, B.; Kovačević, A.; Bajčetić, J.; Č. Popović, L. Low ionospheric reactions on tropical depressions prior hurricanes. *Adv. Space Res.* **2017**, *60*, 1866–1877.
- Biagi, P.F.; Maggipinto, T.; Righetti, F.; Loiacono, D.; Schiavulli, L.; Ligonzo, T.; Ermini, A.; Moldovan, I.A.; Moldovan, A.S.; Buyuksarac, A.; et al. The European VLF/LF radio network to search for earthquake precursors: Setting up and natural/man-made disturbances. *Nat. Hazards Earth Syst. Sci.* **2011**, *11*, 333–341.
- Inan, U.S.; Lehtinen, N.G.; Moore, R.C.; Hurley, K.; Boggs, S.; Smith, D.M.; Fishman, G.J. Massive disturbance of the daytime lower ionosphere by the giant γ -ray flare from magnetar SGR 1806-20. *Geophys. Res. Lett.* **2007**, *34*, 8103.
- Tanaka, Y.T.; Raulin, J.P.; Bertoni, F.C.P.; Fagundes, P.R.; Chau, J.; Schuch, N.J.; Hayakawa, M.; Hobara, Y.; Terasawa, T.; Takahashi, T. First Very Low Frequency Detection of Short Repeated Bursts from Magnetar SGR J1550-5418. *Astrophys. J. Lett.* **2010**, *721*, L24–L27.
- Bajčetić, J.; Nina, A.; Čadež, V.M.; Todorović, B.M. Ionospheric D-Region Temperature Relaxation and Its Influences on Radio Signal Propagation After Solar X-Flares Occurrence. *Thermal Sci.* **2015**, *19*, S299–S309.
- Ferguson, J.A. *Computer Programs for Assessment of Long-Wavelength Radio Communications, Version 2.0*; Space and Naval Warfare Systems Center: San Diego, CA, USA, 1998.
- Marshall, R.A.; Wallace, T.; Turbe, M. Finite-Difference Modeling of Very-Low-Frequency Propagation in the Earth-Ionosphere Waveguide. *IEEE Trans. Antennas Propag.* **2017**, *65*, 7185–7197.
- Rapopot, Y.; Grimalsky, V.; Fedun, V.; Agapitov, O.; Bonnell, J.; Grytsai, A.; Milinevsky, G.; Liashchuk, A.; Rozhnoi, A.; Solovieva, M.; et al. Model of the propagation of very low-frequency beams in the Earth–ionosphere waveguide: Principles of the tensor impedance method in multi-layered gyrotropic waveguides. *Ann. Geophys.* **2020**, *38*, 207–230.

25. Morfitt, D.G.; Shellman, C.H. *MODESRCH, an Improved Computer Program for Obtaining ELF/VLF Mode Constants in an EARTH-Ionosphere Waveguide*; Naval Electronics Laboratory Center: San Diego, CA, USA, 1976.
26. McRae, W.M.; Thomson, N.R. Solar flare induced ionospheric D-region enhancements from VLF phase and amplitude observations. *J. Atmos. Solar Terr. Phys.* **2004**, *66*, 77–87.
27. Thomson, N.R.; Rodger, C.J.; Clilverd, M.A. Large solar flares and their ionospheric D region enhancements. *J. Geophys. Res. Space* **2005**, *110*, A06306.
28. Žigman, V.; Grubor, D.; Šulić, D. D-region electron density evaluated from VLF amplitude time delay during X-ray solar flares. *J. Atmos. Solar Terr. Phys.* **2007**, *69*, 775–792.
29. Grubor, D.P.; Šulić, D.M.; Žigman, V. Classification of X-ray solar flares regarding their effects on the lower ionosphere electron density profile. *Ann. Geophys.* **2008**, *26*, 1731–1740.
30. Basak, T.; Chakrabarti, S.K. Effective recombination coefficient and solar zenith angle effects on low-latitude D-region ionosphere evaluated from VLF signal amplitude and its time delay during X-ray solar flares. *Astrophys. Space Sci.* **2013**, *348*, 315–326.
31. Nina, A.; Čadež, V. Electron production by solar Ly- α line radiation in the ionospheric D-region. *Adv. Space Res.* **2014**, *54*, 1276–1284.
32. Poulsen, W.L.; Bell, T.F.; Inan, U.S. The scattering of VLF waves by localized ionospheric disturbances produced by lightning-induced electron precipitation. *J. Geophys. Res. Space* **1993**, *98*, 15553–15559.
33. Han, F.; Cummer, S.A.; Li, J.; Lu, G. Daytime ionospheric D region sharpness derived from VLF radio atmospheric. *J. Geophys. Res.-Space Phys.* **2011**, *116*, 5314.
34. Thomson, N.R. Experimental daytime VLF ionospheric parameters. *J. Atmos. Solar Terr. Phys.* **1993**, *55*, 173–184.
35. McRae, W.M.; Thomson, N.R. VLF phase and amplitude: Daytime ionospheric parameters. *J. Atmos. Solar Terr. Phys.* **2000**, *62*, 609–618.
36. Thomson, N.R.; Rodger, C.J.; Clilverd, M.A. Daytime D region parameters from long-path VLF phase and amplitude. *J. Geophys. Res.-Space* **2011**, *116*, 11305.
37. Gross, N.C.; Cohen, M.B. VLF Remote Sensing of the D Region Ionosphere Using Neural Networks. *J. Geophys. Res. Space* **2020**, *125*, e2019JA027135.
38. Davis, R.M.; Berry, L.A. *A Revised Model of the Electron Density in the Lower Ionosphere*; Technical Report TR III-77; Defense Communications Agency Command Control Technical Center: Washington, DC, USA, 1977.
39. Todorović Drakul, M.; Čadež, V.M.; Bajčetić, J.; L. C. Popović, D.B.; Nina, A. Behaviour of electron content in the ionospheric D-region during solar X-ray flares. *Serb. Astron. J.* **2016**, *193*, 11–18.
40. Srećković, V.; Šulić, D.; Vujičić, V.; Jevremović, D.; Vykylyuk, Y. The effects of solar activity: Electrons in the terrestrial lower ionosphere. *J. Geograph. Inst. Cvijic* **2017**, *67*, 221–233.
41. Morgan, R.R. *World-Wide VLF Effective Conductivity Map*; Westinghouse Electric: Cranberry Township, PA, USA, 1968.
42. Wait, J.R.; Spies, K.P. *Characteristics of the Earth-Ionosphere Waveguide for VLF Radio Waves*; NBS Technical Note: Boulder, CO, USA, 1964.
43. Belrose, J.S.; Burke, M.J. Study of the Lower Ionosphere using Partial Reflection: 1. Experimental Technique and Method of Analysis. *J. Geophys. Res.* **1964**, *69*, 2799–2818.
44. Kane, J. Re-evaluation of ionospheric electron densities and collision frequencies derived from rocket measurements of refractive index and attenuation. *J. Atmos. Terr. Phy.* **1961**, *23*, 338–347.
45. Mitra, A.P., Ed. *Ionospheric Effects of Solar Flares*. Astrophysics and Space Science Library; Springer Nature: Cham, Switzerland, 1974; Volume 46.
46. Ferguson, J.A. *Ionospheric Profiles for Predicting Nighttime VLF/LF Propagation*; Technical report; Naval Ocean Systems Center: San Diego, CA, USA, 1980.
47. Kumar, A.; Kumar, S. Solar flare effects on D-region ionosphere using VLF measurements during low- and high-solar activity phases of solar cycle 24. *Earth Planets Space* **2018**, *70*, 29.
48. Hayes, L.A.; Gallagher, P.T.; McCauley, J.; Dennis, B.R.; Ireland, J.; Inglis, A. Pulsations in the Earth's Lower Ionosphere Synchronized With Solar Flare Emission. *J. Geophys. Res.-Space* **2017**, *122*, 9841–9847.
49. Cohen, M.B.; Inan, U.S.; Paschal, E.W. Sensitive Broadband ELF/VLF Radio Reception With the AWESOME Instrument. *IEEE Trans. Geosci. Remote Sens.* **2010**, *48*, 3–17.
50. Nina, A.; Čadež, V.M.; Bajčetić, J.; Mitrović, S.T.; Popović, L.Č. Analysis of the Relationship Between the Solar X-ray Radiation Intensity and the D-Region Electron Density Using Satellite and Ground-Based Radio Data. *Solar Phys.* **2018**, *293*, 64.
51. Ammar, A.; Ghalila, H. Estimation of nighttime ionospheric D-region parameters using tweek atmospheric observations for the first time in the North African region. *Adv. Space Res.* **2020**, *66*, 2528–2536.
52. Bilitza, D. IRI the International Standard for the Ionosphere. *Adv. Radio Sci.* **2018**, *16*, 1–11.
53. Thomson, N.R.; Clilverd, M.A.; Rodger, C.J. Midlatitude ionospheric D region: Height, sharpness, and solar zenith angle. *J. Geophys. Res. Space* **2017**, *122*, 8933–8946.



Global Episteme Inc

Webinar on

MATERIAL SCIENCE

31 March 2021

Chemical doping of Langmuir-Blodgett assembled graphene films

Ivana R Milošević^{1*}, Borislav Vasić¹, Aleksandar Matković² and Jasna Vujin¹

¹University of Belgrade, Serbia

²Montanuniversität Leoben, Austria

abstract

Graphene has been identified as a promising material in electronics, especially as an electrode with the appropriate Work Function (WF). Graphene displays ability to have two different roles as an electrode in electronic and optoelectronic devices (as an anode and a cathode). To achieve the desired performance of the devices, tuning the electrodes' WF is very important. By modulating the WF, band-structure alignment at the interface can enhance the efficiency of carrier transport and lower contact resistance, thus improving performance of the devices. Chemical doping represents the effective method for modulating the WF by charge transfer between the graphene sheet films and dopants, especially in the cases where graphene fabrication procedure results with many exposed basal-plane edges of graphene. Graphene Sheet (GS) dispersions were obtained from liquid-phase exfoliation of graphite and films were prepared using Langmuir-Blodgett Assembled (LBA) method. Such fabrication pathway is compatible with low cost and large scale fabrication. With the LBA method, GS self-assemble at the water-air interface forming a film. Different approaches for chemical doping can be applied to LBA graphene films. In the first approach, doping with nitric acid was done after film formation and a fivefold improvement of sheet conductivity was achieved (doi:10.1088/2053-1583/3/1/015002). This process does not affect electrodes' transparency. In the second approach doping with Li and Au salts was done during the film formation in the LBA process. Li and Au standard solutions were introduced instead of the water in the LBA technique. Au-based salts increase the WF of the films (p-doping), while Li-based salts decrease it (n-doping). As a result, this method allowed to tune the WF of graphene electrodes in a range of 0.7 eV (doi.org/10.1038/s41598-020-65379-1). Chemical doping of LBA graphene films is a simple and low-cost method for modulating WF, thus can widen their possible applications in low-cost optoelectronic devices.

Biography

Ivana R Milošević defended her PhD thesis (2014) at the Faculty of Physical Chemistry, University of Belgrade, Serbia. She is an assistant research professor at "Laboratory for 2D materials" at Centre for Solid State Physics and New Materials, Institute of Physics Belgrade. From 2020 she is Head of the Laboratory. Earlier, her experimental work was focused on environmental issues. Recently, the field of research has been expanded to synthesis of 2D materials, fabrication of thin and transparent films of 2D materials, chemical doping of 2D materials and their potential application in flexible and printed optoelectronics.



PHYSICAL CHEMISTRY 2016

*13th International Conference on
Fundamental and Applied Aspects of
Physical Chemistry*

*Proceedings
Volume I*

BELGRADE
September 26 - 30, 2016



PHYSICAL CHEMISTRY 2016

*13th International Conference on
Fundamental and Applied Aspects of
Physical Chemistry*

*Proceedings
Volume I*

BELGRADE
September 26-30, 2016

ISBN 978-86-82475-34-7

Title: Physical Chemistry 2016 (Proceedings)

Editors: Željko Čupić and Slobodan Anić

Published by: Society of Physical Chemists of Serbia, Studentski trg 12-16, 11158, Belgrade, Serbia.

Publisher: Society of Physical Chemists of Serbia

For Publisher: S. Anić, President of Society of Physical Chemists of Serbia

Printed by: "Jovan", Printing and Publishing Company; 200 Copies.

Number of pages: 6+502; Format B5; printing finished in September 2016

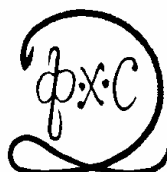
Text and Layout: "Jovan"

Neither this book nor any part may be reproduced or transmitted in any form or by any means, including photocopying, or by any information storage and retrieval system, without permission in writing from the publisher.

200 - Copy printing

CONTENT

<i>Volume I</i>	
<i>Organizer</i>	IV
<i>Comittes</i>	V
<i>Sponsors</i>	VI
<i>Plenary Lecture</i>	1
<i>Spectroscopy, Molecular Structure, Physical Chemistry of Plasma</i>	47
<i>Kinetics, Catalysis</i>	183
<i>Nonlinear Dynamics, Oscillatory Reactions, Chaos</i>	267
<i>Electrochemistry</i>	355
<i>Biophysical Chemistry, EPR Investigations of bio-systems, Photochemistry, Radiation Chemistry</i>	409



PHYSICAL CHEMISTRY 2016

*13th International Conference on
Fundamental and Applied Aspects of
Physical Chemistry*

Organized by

*The Society of Physical Chemists of
Serbia*

in co-operation with

Institute of Catalysis Bulgarian Academy of Sciences

and

*Boriskov Institute of Catalysis Siberian Branch of
Russian Academy of Sciences*

and

University of Belgrade, Serbia:

Faculty of Physical Chemistry

Institute of Chemistry, Technology and Metallurgy

Vinča Institute of Nuclear Sciences

Faculty of Pharmacy

Institute of General and Physical Chemistry, Belgrade, Serbia

International Organizing Committee

- Chairman:** S. Anić (Serbia)
Vice-chairman: M. Gabrovska (Bulgaria)
A. A. Vedyagin (Russia)
S. N. Blagojević (Serbia)
Members: N. Cvjetičanin (Serbia), S. M. Blagojević (Serbia), M. Daković (Serbia), J. Dimitrić-Marković (Serbia), T. Grozdić (Serbia), Lj. Ignjatović (Serbia), D. Jovanović (Serbia), J. Jovanović (Serbia), M. Kuzmanović (Serbia), D. Marković (Serbia), B. Milosavljević (USA), M. Mojović (Serbia), N. Ostrovski (Serbia), N. Pejić (Serbia), M. Petković (Serbia), A. Popović-Bjelić (Serbia), B. Simonović (Serbia), D. Stanisavljev (Serbia), M. Stanković (Serbia), Z. Šaponjić (Serbia), B. Šljukić (Serbia), G. Tasić (Serbia), N. Vukelić (Serbia), V. Vukojević (Sweden)

International Scientific Committee

- Chairman:** Ž. Čupić (Serbia)
Vice-chairmans: V. N. Parmon (Russia)
S. Rakovsky (Bulgaria)
B. Adnađević (Serbia)
Members: S. Anić (Serbia), A. Antić-Jovanović (Serbia), G. Bačić (Serbia), R. Cervellati (Italy), G. Ćirić-Marjanović (Serbia), A. Cricenti (Italy), V. Dondur (Serbia), S. D. Furrow (USA), L. Gábor (Hungary), Vilmos Gáspár (Hungary), K. Hedrih (Serbia), M. Jeremić (Serbia), E. Kiš (Serbia), Lj. Kolar-Anić (Serbia), U. Kortz (Germany), T. Kowalska (Poland), V. Kuntić (Serbia), Z. Marković (Serbia), S. Mentus (Serbia), K. Novaković (UK), B. Novakovski (Poland), T. Parac Vogt (Belgium), M. Perić (Serbia), M. Plavšić (Serbia), G. Schmitz (Belgium), I. Schreiber (Czech Republic), P. Ševčík (Slovakia), N. Stepanov (Russia), M. Trtica (Serbia), V. Vasić (Serbia), D. Veselinović (Serbia), Á. Tóth (Hungary)

Local Executive Committee

- Chairman:** S. N. Blagojević
Vice-chairmans: A. Ivanović-Šašić
A. Stoiljković
Members: M. Ajduković, P. Banković, N. Bošnjaković, I. N. Bubanja, D. Dimić, A. Dobrota, J. Dostanić, A. Ignjatović, S. Jovanović, Z. Jovanović, A. Jović, N. Jović-Jovičić, D. Lončarević, M. Kragović, J. Krstić, S. Maćešić, J. Maksimović, V. Marković, D. Milenković, M. Milovanović, B. Nedić-Vasiljević, M. Pagnacco, A. Pavićević, N. Potkonjak, D. Ranković, M. Ristić, B. Stanković, A. Stanojević

VARIATIONS IN LARCH TREE-RINGS METAL CONCENTRATIONS OF FOUR FORESTRY LOCATIONS

I. R. Milošević¹, D.M. Marković², D. Manojlović³ and G. Roglić³

¹ *University of Belgrade, Institute of Physics, Pregrevica 118, 11070 Belgrade, Serbia. (novovic@ipb.ac.rs)*

² *Singidunum University, The Faculty of Applied Ecology, Požeška 83a, 11030 Belgrade, Serbia.*

³ *University of Belgrade, Faculty of Chemistry, Studentski trg 12-16, 11000 Belgrade, Serbia.*

ABSTRACT

Cd, Fe, Mn, Pb, Sr and Zn were measured in larch (*Larix europaea* Lam.) tree-rings and corresponding soil samples collected at four forestry sites to investigate the variations in their concentrations from 1980. Concentrations were generally lowest at background sites. Elemental concentrations in soil samples were substantially higher than those measured in tree-rings. Among investigated elements the highest tree-ring concentration were measured for Mn while the Cd had the lowest concentration. The highest average tree-ring concentrations for Cd, Fe, Mn, Pb and Zn can be seen at the Avala location.

INTRODUCTION

The occurrence of trace elements in the environment is of particular concern due their environmental persistence, biogeochemical recycling and adverse effects. Several trace elements currently found in the environment are originated from anthropogenic impacts [1]. It has long been recognized that the tree-ring archive can capture changes in the chemical environment related to atmospheric chemistry, biogeochemical cycling and climate influences. Choosing tree-rings as potential bioindicators was due to trees large geographic distribution, long living and the fact that each year tree forms a new tree-ring that can be easily dated. Dendrochemistry relies on the basic assumption that the pollutant content of tree-rings reflects to some degree the chemical signal from the environment during the year of ring formation [2].

EXPERIMENTAL

The field studies were conducted in the three woodland locations in Serbia and one in Montenegro. Tree-rings of larch (*Larix europaea* Lam.) were collected together with corresponding soil (0-20 cm in depth). The first location is Avala (AA), a mountain located 16 km south-east of Belgrade. The Belgrade-Niš

highway, Kruni put and regional road to Mladenovac runs east, north and west from the mountain. The second location is REIK Kolubara (AK). Larch at the Kolubara location has been applied for the rehabilitation by afforestation of the mechanically damaged land. Background locations were management unit Donji Pek in Kučevo (AKC) and village Trepča in Andrijevića municipality in the north-east part of Montenegro (ACG).

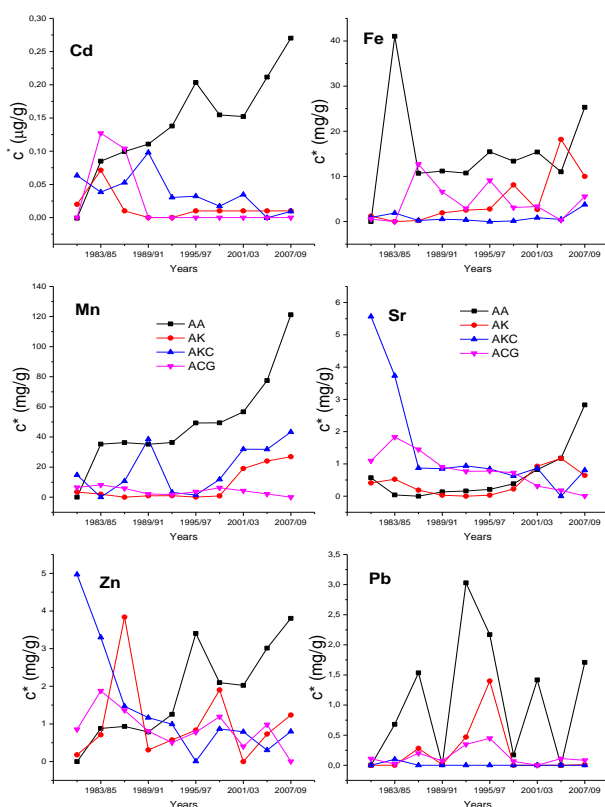


Figure 1. Mean Cd, Fe, Mn, Sr, Zn and Pb concentrations, c^* ($\mu\text{g/g}$), in larch tree-rings at four forestry locations

At each site three larch trees of similar size were selected and their stem disks were taken at breast height (1.3 m). For further analysis the disks were cut into 3 year segments starting from 1980 with a stainless steel knife. Inductively coupled plasma atomic emission spectrometry (ICP-OES) was used to determine element content in solution samples. ICP-OES measurement was performed using Thermo Scientific iCAP 6500 Duo ICP spectrometer equipped with CID86 detector, standard glass concentric type nebulizer, quartz torch, and alumina injector and purged with argon. The digestion of tree-rings was performed on an Advanced Microwave Digestion System ETHOS 1, using HPR-1000/10S high pressure segmented rotor. In the digestion, about 0.5 g of powdered tree-ring sample precisely weighed was mixed in each clean vessel with a mixture of 3 ml H_2SO_4 and 5 ml HNO_3 for tree-ring sample and then heated with microwave energy for 30 min. After cooling and without filtration, the solution was diluted to a fixed volume of 25 ml. The sequential extraction using the Tessier procedure [3] was used for the

examination of soil samples. The method involves five fractions (exchangeable, carbonate, Fe/Mn oxides, organic and residual), in which the mobility and bioavailability of elements decrease with increasing extraction phase. The extraction was carried out progressively based on an initial amount of about 1.0 g of soil, accurately weighed. The first three fractions form “mobile content”, i.e. the part of the total concentration which under certain conditions can be mobilized and thus enter biogeochemical cycles. Soil pH was measured as follows: 5.0 g of soil was precisely weighed and 5ml of 1M KCl added. The suspension was then subjected to continuous agitation for 10 min and left to stand before pH was determined.

RESULTS AND DISCUSSION

Element concentrations measured in tree-rings and soil are summarized in Figure 1 and Table 1. The variation in tree-ring concentrations due to different local conditions (the variation of the background levels) was minimize by subtracting the minimum value from the actual concentration. Element tree-ring concentrations, c^* , shown in Figure 1 do not refer to actual concentration in wood, but to the level of this content relative to the lowest level recorded for that tree. Subtracting the minimum value from the actual concentration reduces

Table 1. Average concentrations in larch tree-rings, mobile and total content in soil as well as pH values at four forestry locations.

Locations		AA	AK	AKC	ACG
Cd	Tree-ring	0.14	0.02	0.04	0.02
	Mobile content	0.36	<0.10	<0.10	<0.10
	Total content	0.46	0.23	0.94	0.90
Fe	Tree-ring	15.42	4.77	0.92	4.42
	Mobile content	1243	496	12409	10117
	Total content	8176	6723	66835	54436
Mn	Tree-ring	49.73	7.83	18.74	4.06
	Mobile content	603	141	1246	1607
	Total content	662	191	1949	1897
Pb	Tree-ring	1.07	0.22	0.01	0.15
	Mobile content	7.21	5.55	33.76	38.06
	Total content	16.50	13.04	51.14	55.53
Sr	Tree-ring	0.63	0.41	1.51	0.80
	Mobile content	15.59	7.33	16.38	30.00
	Total content	18.90	10.04	52.93	46.75
Zn	Tree-ring	1.82	1.03	1.47	0.88
	Mobile content	11.30	3.97	45.54	30.71
	Total content	33.35	23.08	147.58	151.11
pH		5.80	6.00	4.50	5.30

differences between trees that are due to different local conditions, and concentrate on the trends over time. From Figure 1 it can be seen that concentrations were generally lowest at background sites. The highest average tree-ring concentrations for Cd, Fe, Mn, Pb and Zn (Table 1) can be seen at the Avala location. Among investigated elements the highest tree-ring concentration were measured for Mn while the Cd had the lowest concentration. Highest Pb concentration fluctuations in tree-rings can be seen at the Avala location. Similar Pb fluctuations were observed in our investigation in linden tree-rings [4]. Expected trends in tree-ring concentrations for the majority of trace elements is that on locations where anthropogenic influence is low there is no trend [5-6]. At the Avala location growing trend of Cd, Mn, Zn and Sr was observed while at other locations, depending of the element, the weaker trend or a decline in the concentration can be seen. Elemental concentrations in soil samples (Table 1) were substantially higher than those measured in tree-rings. This could be attributed to the relatively longer exposure of the soil to the atmospheric pollutants. Soil act as final sink for the elements deposited from air and also transferred by falling needles. Mobile content, relative to the total content, is for the majority of investigated elements highest at the Avala location.

CONCLUSION

At the Avala location during the last 12 years (1998-2009) the increase of Cd, Fe, Mn, Sr and Zn in larch tree-rings, relative to the entire period of study, expressed in percentage is 30%, 4%, 43%, 85% i 40%. At this location the highest fluctuations in Pb concentration can be seen, the highest average Pb tree-ring concentrations, as well as decrease in Pb concentration for 18%. Traffic activity at this site appears to be the main reason. Other investigated location has lower tree-ring trace element concentrations.

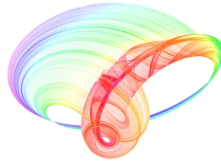
Acknowledgement

This work was partially supported by the Ministry of Education and Science of the Republic of Serbia (Grants no. III 43007 and OI 171005).

REFERENCES

- [1] G. Blackmore, *Science of the Total Environment*, 1998, **214**, 21-48.
- [2] H.C. MacDonald, C.P. Laroque, D. E. B. Fleming, M. R. Gherase, *Dendrochronologia*, 2011, **29**, 9-15.
- [3] A. Tessier, P.G.C. Campbell, M. Bisson, *Analytical Chemistry*, 1979, **51**, 844-851.
- [4] D.M. Marković, I.R. Milošević, D. Vilotić, 2013, *Environmental Science and Pollution Research*, **20**, 136-145.
- [5] S.A. Watmough, 1999, *Environmental Pollution*, **106**, 391-403.
- [6] C. Liang, H. Huang, 1992, *Trees*, **6**, 103-108.

Book of abstracts



PHOTONICA2019

The Seventh International School and Conference on
Photonics, 26 August – 30 August 2019, Belgrade, Serbia

& Machine Learning with Photonics Symposium
(ML-Photonica 2019)



& ESUO Regional Workshop



& COST action CA16221



Editors: Milica Matijević, Marko Krstić and Petra Beličev

Belgrade, 2019

ABSTRACTS OF TUTORIAL, KEYNOTE, INVITED LECTURES,
PROGRESS REPORTS AND CONTRIBUTED PAPERS

of

The Seventh International School and Conference on Photonics
PHOTONICA2019, 26 August – 30 August 2019, Belgrade, Serbia

and

Machine Learning with Photonics Symposium

and

ESUO Regional Workshop

Editors

Milica Matijević, Marko Krstić and Petra Beličev

Technical Assistance

Danka Stojanović and Goran Gligorić

Publisher

Vinča Institute of Nuclear Sciences

Mike Petrovića Alasa 12-14, P.O. Box 522

11000 Belgrade, Serbia

Printed by

Serbian Academy of Sciences and Arts

Number of copies

300

ISBN 978-86-7306-153-5

PHOTONICA2019 (The Seventh International School and Conference on Photonics-www.photonica.ac.rs) is organized by Vinča Institute of Nuclear Sciences, University of Belgrade (www.vinca.ac.rs), Serbian Academy of Sciences and Arts (www.sanu.ac.rs), and Optical Society of Serbia (www.ods.org.rs).



Institute of Nuclear Sciences Vinča



Serbian Academy of Sciences and Arts



Optical Society of Serbia

Other institutions that helped the organization of this event are: Institute of Physics Belgrade, University of Belgrade (www.ipb.ac.rs), School of Electrical Engineering, University of Belgrade (www.etf.bg.ac.rs), Institute of Chemistry, Technology and Metallurgy, University of Belgrade (www.ihtm.bg.ac.rs), Faculty of Technical Sciences, University of Novi Sad (www.ftn.uns.ac.rs), Faculty of Physics, University of Belgrade (www.ff.bg.ac.rs), and Faculty of Biology, University of Belgrade (www.bio.bg.ac.rs). Joint event “Machine learning with Photonics Symposium” has been co-organized with programme partners H2020-RISE-CARDIALLY, H2020 – MULTIPLY and H2020-EID-FONTE.

PHOTONICA2019 is organized under auspices and with support of the Ministry of Education, Science and Technological Development, Republic of Serbia (www.mpn.gov.rs). PHOTONICA2019 is supported and recognized by OSA - The Optical Society (www.osa.org), Integrated Initiative of European Laser Research Infrastructures Laser Lab-Europe (www.laserlab-europe.eu) and European Physical Society (www.eps.org).



Ministry of Education, Science and Technological Development of the Republic of Serbia



The support of the sponsors of PHOTONICA2019 is gratefully acknowledged:



Self-organization of soliton-tweezers in suspensions of nanocomposites and graphens

M. Lekić¹, I. Milosević¹, S. Rokotoarimalala² and V. Skarka^{1,2,3}

¹*Institute of Physics, University of Belgrade, Pregrevica 118, Belgrade, Serbia*

²*Laboratoire de Photonique d'Angers, EA 4464, University of Angers,
2 Boulevard Lavoisier, 49045 Angers, France*

³*Science Program, Texas A&M University at Qatar, P.O. Box 23874, Doha, Qatar*

e-mail: lekic@ipb.ac.rs

Laser beams and pulses are powerful tools for tweezing, photobiomodulation, and manipulation of soft matter including colloidal nanosuspensions, emulsions, foams, as well as all kinds of biomedica like myosin, kinesin, ribosomes, liposomes, bacterias, viruses, blood, and a variety of living cells in body water [1]. The laser modifies the nonlinear mater passing through. Simultaneously, the modified mater acts to the light altering it by a feedback mechanism. Therefore, light is controlled by light through interaction with nonlinear mater. Laser stability and precision are of crucial importance not only for brain surgery but also for nondestructive diagnostics using this feedback mechanism. In order to achieve the necessary dynamical stability, the promising mechanism is the self-structuring of the light into localized solitons via nonlinear interaction inside the colloidal nanosuspensions and other varieties of soft matter. Tweezing solitons stable propagation is self-organized by the balance of antagonist effects, *i.e.*, beam self-focusing and self-defocusing [2]. The high frequency pressure force of the laser field either attracts or repels the nanoparticles from the field region, depending if their optical index of refraction is larger or smaller than the background one [3]. In both cases, the nanoparticles density modification results in the nonlinear increase of effective index of refraction inside the beam making it self-focusing. We use this self-focusing effect to establish theoretically, numerically and experimentally the self-organization of soliton-tweezers as a novel kind of dynamically reconfigurable self-collimated tweezing facilities. Such soliton-tweezers will be able to photobiomodulate and manipulate, in a noninvasive way, micro and nanoparticles in body water and other soft mater of interest for medical and biological applications. Based on the synergy between theory and experiment via numerical simulations, other nanocomposites and colloidal nanosuspensions involving graphene and various two-dimensional materials will be tweezed using spatiotemporal dissipative solitons and multidimensional vortex solitons [4, 5].

REFERENCES

- [1] A. Ashkin, J. M. Dziedzic, T. Yamane, *Nature* 330, 769 (1987).
- [2] V. Skarka, N. B. Aleksic, *Phys. Rev. Lett.* 96, 013903 (2006).
- [3] V. Skarka et al., *Opt. Express* 25, 10090 (2017).
- [4] V. Skarka et al., *Opt. Quant. Electron.* 50, 37 (2018).
- [5] V. Skarka et al., *Phys. Rev. A* 90, 023845 (2014).

Chemical doping of Langmuir-Blodgett assembled few-layer graphene films with Au and Li salts aimed for optoelectronic applications

I. R. Milošević¹, B. Vasić¹, A. Matković², J. Vujin¹, S. Aškračić³, C. Teichert² and R. Gajić¹

¹Laboratory for Graphene, other 2D materials and Ordered Nanostructures of Center for Solid State Physics and New Materials, Institute of Physics, University of Belgrade, Belgrade, Serbia

²Institute of Physics, Montanuniversität Leoben, Leoben, Austria

³Nanostructured Matter Laboratory of Center for Solid State Physics and New Materials, Institute of Physics, University of Belgrade, Belgrade, Serbia

e-mail: novovic@ipb.ac.rs

For mass production of graphene, simple and low-cost methods are needed especially in the cases where high-quality films are not crucial for the desired purposes. Thus, liquid-phase exfoliation (LPE) is a perspective way of obtaining stable dispersion of few-layer graphene sheets (GS) in the solvent [1]. A promising pathway to achieve high degree of ordering of graphene sheets prepared via LPE-process is to utilize Langmuir-Blodgett assembly (LBA) technique. Thin-films are self-assembled from LPE dispersion by LBA technique at the water-air interface. LBA method is a suitable method for production of large-scale, transparent, thin solution-processed graphene films [2, 3]. Chemical doping of graphene films allows to tune its work function (WF) and therefore gives LPE GS films the ability to serve two different roles in electronic and optoelectronic applications, both as an anode and as a cathode.

Here, we demonstrate the method for the forming and doping of LPE graphene sheet films (LPE GS) in one-step by metal standard solutions. Doping of the graphene film occurs at the moment of its formation from the LPE graphene dispersion by LBA method at the air-metal standard solution interface. n-doping is achieved by Li standard solutions (LiCl, LiNO₃, Li₂CO₃), while Au standard solution (H(AuCl₄)) leads to p-doping. WF of the film was decreased with Li based salts, while Au based salts increase the WF of the film. The maximal doping in both directions allow a significant range of around 0.7 eV for the WF modulation. The results were obtained for 0.1 mol/dm³ concentration of dopants. Roughness of the LPE GS films does not change by the doping, except that doped films contain occasional agglomerates. FT-IR measurements point out that the charge transfer process is enabled by physical adsorption of the metal salts and that the graphene basal planes stay chemically unchanged by metal doping. No significant shifts of any characteristic Raman peaks of graphene were detected after chemical doping. Calculated values of the intensity ratio between D and D' peak indicate that the edges are the dominant type of defects in the undoped and metal salt doped LPE GS films. Electrical properties of the films were significantly influenced by changing the dopant (Au or Li). A significant suppression of the field-effect mobility and the increase of the sheet resistivity were observed in the case of the Li standard solution doping of the film. This indicates that adsorbed Li anions act as scattering centers for the charges. Lithium nitrate provides the largest work function modulation (by 400 meV) and the least influence on the sheet resistance of the film. Therefore, it was selected as the best choice for n-type doping.

Since, the proposed one-step method for chemical doping of graphene films allows to tune WF in a large range, it extends the potential use of these materials in low-cost optoelectronic applications, as in low-power lighting, sensors, transparent heating, and de-icing applications.

REFERENCES

- [1] C. Backes et al., Chem. Mater. 29, 243 (2017).
- [2] Q. Zheng et al., ACS Nano. 5, 6039 (2011).
- [3] A. Matković et al., 2D Mater. 3, 015002 (2016).

7-11th October 2019
Belgrade, Serbia



<http://www.sfkm.ac.rs/>

The 20th Symposium on Condensed Matter Physics

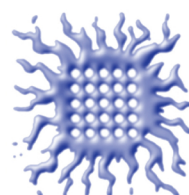
BOOK OF ABSTRACTS



University of Belgrade,
Faculty of Physics



Institute of Physics Belgrade



Vinca Institute
of Nuclear Sciences



Serbian Academy
of Sciences and Arts



Ministry of Education, Science and
Technological Development,
Republic of Serbia

Conference Chair

Cedomir Petrovic, *Brookhaven National Laboratory, USA*

Željko Šljivančanin, *Vinča Institute of Nuclear Sciences Serbia*

Organizing Committee

Jelena Pešić, *Institute of Physics Belgrade*

Andrijana Šolajić, *Institute of Physics Belgrade*

Petar Mali, *Faculty of Sciences, University of Novi Sad*

Jelena Pajović, *Faculty of Physics, University of Belgrade, Serbia*

Srđan Stavrčić, *Vinča Institute of Nuclear Sciences*

Svetislav Mijatović, *Faculty of Physics, University of Belgrade, Serbia*

Božidar Nikolić, *Faculty of Physics, University of Belgrade, Serbia – chair*

Organized by

Institute of Physics Belgrade

Faculty of Physics, University of Belgrade

Vinča Institute of Nuclear Sciences

Serbian Academy of Sciences and Arts

Program Committee

Ivan Božović, *Brookhaven National Laboratory, USA*

Vladimir Dobrosavljević, *Florida State University, USA*

Milan Damnjanović, *Faculty of Physics, University of Belgrade, Serbia*

Vladimir Djoković, *Vinča Institute, University of Belgrade, Serbia*

Gyula Eres, *Oak Ridge National Laboratory, USA*

Laszló Forró, *Ecole Polytechnique Fédérale de Lausanne, Switzerland*

Radoš Gajić, *Institute of Physics Belgrade, University of Belgrade, Serbia*

Igor Herbut, *Simon Fraser University, Canada*

Zoran Ikonić, *University of Leeds, UK*

Ivanka Milošević, *Faculty of Physics, University of Belgrade, Serbia*

Branislav Nikolić, *University of Delaware, USA*

Cedomir Petrovic, *Brookhaven National Laboratory, USA*

Dragana Popović, *National High Magnetic Field Laboratory USA*

Zoran S. Popović, *Vinča Institute, University of Belgrade, Serbia*

Zoran V. Popović, *Institute of Physics, University of Belgrade, Serbia*

Zoran Radović, *Faculty of Physics, University of Belgrade, Serbia*

Miljko Satarić, *Faculty of Technical Sciences, University of Novi Sad, Serbia*

Vojislav Stamenković, *Argonne National Laboratory, USA*

Željko Šljivančanin, *Vinča Institute, University of Belgrade, Serbia*

Bosiljka Tadić, *Jožef Štefan Institute, Slovenia*

Milan Tadić, *School of Electrical Engineering, University of Belgrade, Serbia*

Darko Tanasković, *Institute of Physics, University of Belgrade, Serbia*

XX SYMPOSIUM ON CONDENSED MATTER PHYSICS SFKM 2019

Conference presentations cover full range of research topics within the experimental, theoretical and computational condensed matter physics, including but not limited to the following:

Semiconductor physics. Electronic structure, Quantum dots and wires, Photonic crystals, High magnetic fields phenomena, Ultra-fast phenomena.

Surface, interface and low-dimensional physics. Graphene, Carbon and other nanotubes, Topological insulators, Complex oxide interfaces, Transport in nanostructures.

Magnetism. Magnetic materials and phase transitions, Magneto-electronics and spintronics, Magnetic nanoparticles.

Superconductivity. Conventional, high T_c , and heavy-fermion superconductors: Materials and mechanisms, Heterostructures: Proximity effect and transport phenomena.

Strongly correlated and disordered systems. Materials with strong correlations and disorder, Dynamical properties from time-resolved experiments, Quantum fluids, Cold atoms and BEC.

Phase transitions, phase ordering and structural ordering of condensed matter. Equilibrium and dynamic phenomena, Ferroelectricity, Multiferroics, Quasi-Crystals, Crystal surface morphology and dynamics, Crystal growth.

Soft and biological matter. Polymers, Liquids and gels, Liquid crystals, Elastomers, Membranes, Living cells and living matter.

Statistical physics of complex systems. Networks and other structures.

Conference venue:

Serbian Academy of Sciences and Arts, Knez Mihailova 35, Belgrade

Conference website: <http://www.sfkm.ac.rs>

LIST OF INVITED SPEAKERS

- Marco Aprili, PS-CNRS Université Paris-Sud, France
- Stefano Baroni, Scuola Internazionale Superiore di Studi Avanzati, Italy
- Wolfgang Belzig, University of Konstanz, Germany
- Emil Božin, Brookhaven National Laboratory, USA
- Harald Brune, Ecole Polytechnique Fédérale de Lausanne, Switzerland
- Liviu Chioncel, University of Augsburg, Germany
- Gyula Eres, Oak Ridge National Laboratory, USA
- Laszlo Forro, Ecole Polytechnique Fédérale de Lausanne, Switzerland
- Rudolf Gross, Walther Meissner Institute, Germany
- Rudi Hackl, Walther Meissner Institute, Germany,
- Igor Herbut, Simon Fraser University, Canada
- Kurt Hingerl, Johannes Kepler University, Linz, Austria
- Liv Hornekaer, Aarhus University, Denmark
- Zoran Ikonić, University of Leeds, UK
- Vladimir Juričić, Nordita, KTH Royal Institute of Technology and Stockholm University, Sweden
- Milos Knezevic, Berlin Institute of Technology, Germany
- Hechang Lei, Renmin University
- Marjana Ležaić, Forschungszentrum Jülich, Germany
- Zoran Mišković, University of Waterloo, Canada
- Francois Peeters, University of Antwerp, Belgium
- Axel Pelster, Technical University of Kaiserslautern, Germany
- Maria Peressi, University of Trieste, Italy
- Cedomir Petrovic, Brookhaven National Laboratory, USA
- Hyejin Ryu, Korea Institute of Science and Technology
- Milan Radović, Paul Scherrer Institute, Switzerland
- Nicolas Regnault, Ecole Normale Supérieure Paris, France
- Rastko Sknepnek, University of Dundee, UK
- Frank Steglich, MPICPFS Dresden and Zhejiang University
- Bosiljka Tadić, Jožef Štefan Institute, Slovenia
- Jack Tuszynski, University of Alberta, Canada
- Dieter Vollhardt, University of Augsburg, Germany
- Rok Zitko, Jožef Štefan Institute, Slovenia
- Qingming Zhang, Lanzhou University and Institute of Physics, Chinese Academy of Sciences

Liquid-phase Exfoliation of Graphene and Chemical Doping of Langmuir-Blodgett Assembled Graphene Films

Ivana R. Milošević^a, Borislav Vasić^a, Aleksandar Matković^b, Jasna Vujin^a and Radoš Gajić^a

^aLaboratory for Graphene, Other 2D Materials and Ordered Nanostructures of Center for Solid State Physics and New Materials, Institute of Physics, University of Belgrade, Serbia

^bInstitute of Physics, Montanuniversität Leoben, Austria

Abstract. In current optoelectronic devices transparent conductive (TC) electrodes are widely used [1]. Graphene films as new TC material can be used to overcome shortcomings of the existed TC electrodes especially using graphene films as an active electrode. They offer advantages such as higher transparency over a broad range of light wavelengths, higher flexibility, excellent electrical conductivity and chemical stability. Using graphene films as an active electrode, band-structure alignment at the interface can be achieved with an appropriate work function (WF). Therefore, appropriate WF can enhance the charge injection and improve device performances. Chemical doping is an effective method for tuning of the WF by charge transfer between the graphene sheet films and dopants [2, 3]. Liquid-phase exfoliation (LPE) via sonication was the method for the preparation of graphene sheet (GS) dispersion. The films were self-assembled from LPE few-layer GS dispersion by Langmuir-Blodgett (LBA) technique at the water-air interface. Chemical doping of the films was performed in two ways. In the first approach, chemical doping with nitric acid is introduced after the film was formed. Fivefold improvement of sheet conductivity was achieved, with no change in transparency [4]. In the second approach, chemical doping of the film was happening at the moment of its formation. To achieve doping, metal standard solutions were introduced instead of water. Au based salts increase the WF of the films (p-doping), while Li based salts decrease it (n-doping). A span of 0.7 eV in both directions was obtained. Formation of the graphene films and both procedures of their chemical doping are very simple, low-cost and extend their potential use in low-cost optoelectronic applications as well as using them as an active electrode.

REFERENCES

1. Syu, J-Y., Chen, Y-M., Xu, K-X., He, S-M., Hung, W-C., Chang, C-L. and Su, C-Y., *RSC Adv.* **6**, 32746-32756 (2016).
2. Park, J., Lee, W. H., Huh, S., Sim, S. H., Bin Kim, S., Cho, K., Hong, B. H. and Kim, K. S., *J. Phys. Chem. Lett.* **2**, 841-845 (2011).
3. Kwon, K. C., Choi, K. S., Kim, B. J., Lee, J. L., and Kim, S. Y., *J. Phys. Chem. C.* **118**, 8187-8193 (2014).
4. Matković, A., Milošević, I., Milićević, M., Tomašević-Ilić, T., Pešić, J., Musić, et al. *2D Mater.* **3**, 015002 (2016).

PHOTONICA2015.

V International School and Conference on Photonics
& COST actions: MP1204 and BM1205
& the Second international workshop "Control of light and
matter waves propagation and localization in photonic
lattices"
www.vin.bg.ac.rs/photonica_2015

Book of Abstracts



Editors

Suzana Petrović, Goran Gligorić and Milutin Stepić

Belgrade, 2015.

Book of abstracts



PHOTONICA2015

the Fifth international school and conference on
photonics

& COST actions: MP1204 and BM1205

& the Second international workshop "Control of light and matter
waves propagation and localization in photonic lattices"

24 August – 28 August 2015

Belgrade, Serbia

Editors

Suzana Petrović, Goran Gligorić and Milutin Stepić

Vinča Institute of Nuclear Sciences, Belgrade, Serbia

Belgrade, 2015

ABSTRACTS OF TUTORIAL, KEYNOTE AND INVITED
LECTURES AND CONTRIBUTED PAPERS

of

the Fifth international school and conference on photonics
PHOTONICA2015

and

COST actions MP1204 and BM1205

and

the Second international workshop
"Control of light and matter waves propagation and localization in
photonic lattices"

24 August – 28 August 2015

Belgrade Serbia

Editors

Suzana Petrović, Goran Gligorić, Milutin Stepić

Technical assistance

Petra Beličev, Marijana Petković

Publisher

Vinča Institute of Nuclear Sciences
Mike Petrovića Alasa 12-14, P.O. Box 522
11001 Belgrade, Serbia

Printed by

Serbian Academy of Sciences and Arts

Number of copies

300

ISBN 978-86-7306-131-3

The PHOTONICA2015 (The Fifth International School and Conference on Photonics) is organized by the Vinča Institute of Nuclear Sciences, University of Belgrade (www.vinca.rs), the Serbian Academy of Sciences and Arts, the Optical Society of Serbia and Aston University, Birmingham, UK. Co-organizers of this meeting are: the Institute of Physics Belgrade, University of Belgrade (www.phy.bg.ac.rs), Faculty of Electrical Engineering, University of Belgrade (www.etf.bg.ac.rs), Institute of Chemistry, Technology and Metallurgy, University of Belgrade (www.ihtm.bg.ac.rs), Faculty of Technical Sciences, University of Novi Sad (www.ftn.uns.ac.rs), Faculty of physics, University of Belgrade (www.ff.bg.ac.rs), and Faculty of biology, University of Belgrade (www.bio.bg.ac.rs), under auspices and with support of the Ministry of Education, Science and Technological Development, Serbia.

The support of the sponsors of the Conference is gratefully acknowledged:



Committees

Scientific Committee

Aleksandar Krmpot, Serbia
Antun Balaž, Serbia
Arlene D. Wilson-Gordon, Israel
Boris Malomed, Israel
Branislav Jelenković, Serbia
Dejan Gvozdić, Serbia
Dejan Milošević, Bosnia and Herzegovina
Detlef Kip, Germany
Dragan Indjin, UK
Feng Chen, China
Giorgos Tsironis, Greece
Goran Isić, Serbia
Goran Pichler, Croatia
Jelena Radovanović, Serbia
Jovana Petrović, Serbia
Kurt Hingerl, Austria
Laurentius Windholz, Austria
Ljupčo Hadžievski, Serbia
Milutin Stepić, Serbia
Milivoj Belić, Qatar
Misha Sumetsky, UK
Nikola Burić, Serbia
Pavle Anđus, Serbia
Paul Harrison, UK
Radoš Gajić, Serbia
Sergei Turitsyn, UK
Slobodan Vuković, Serbia
Stefka Cartaleva, Bulgaria
Vladimir Škarka, France
Željko Šljivančanin, Serbia

Organizing Committee

Milutin Stepić, (Chair)
Misha Sumetsky, (Co-Chair)
Suzana Petrović, (Secretary)
Ljupčo Hadžievski
Jovana Petrović
Aleksandra Maluckov
Goran Gligorić
Petra Beličev
Aleksandar Daničić
Marija Ivanović
Nevena Raičević
Ana Radosavljević
Milan Trtica
Slobodan Zdravković
Biljana Gaković
Dalibor Čevizović
Branislav Jelenković
Zoran Grujić
Jelena Radovanović
Peđa Mihailović
Jovan Elazar
Bratislav Obradović
Milorad Kuraica
Zoran Jakšić
Slobodan Vuković
Miloš Živanov

COST actions BM1205 and MP1204 Training School Steering Committee

Mauro Pereira, UK
Anna Wojcik-Jedlinska, Poland
Dragan Indjin, UK
Jelena Radovanovic, Serbia
Antoine Muller, Switzerland
Andreas Wacker, Sweden
Ivan Bucharov, Bulgaria
Johan Stiens, Belgium
Florin Mihalescu, Romania
Czeslaw Skierbiszewski, Poland
Shumin Wang, Sweden
Igor Meglinski, Finland

Conference Topics

1. Quantum optics
2. Nonlinear optics
3. Ultrafast phenomena
4. Laser spectroscopy
5. Devices and components
6. Biophotonics
7. Optical communications
8. Sensing: plasmonics, fiber optics and interferometers
9. Holography and adaptive optics
10. Optical materials



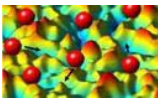
BMBS COST Action BM1205

European Network for Skin Cancer Detection using Laser Imaging
(24-28 August)



MPNS COST Action MP1204

TERA-MIR Radiation: Materials, Generation, Detection and Applications
(24-28 August)



WORKSHOP

Control of light and matter waves propagation and localization in photonic lattices
(28-29 August)

The **International School and Conference on Photonics- PHOTONICA**, is a biennial event held in Belgrade since 2007. The first meeting in the series was called ISCOM (International School and Conference on Optics and Optical Materials), but it was later renamed to Photonica to reflect more clearly the aims of the event as a forum for education of young scientists, exchanging new knowledge and ideas, and fostering collaboration between scientists working within emerging areas of photonic science and technology.

A particular educational feature of the program is to enable students and young researchers to benefit from the event, by providing introductory lectures preceding most recent results in many topics covered by the regular talks. In other words, apart from the regular lectures, the plenary speakers will also give tutorial lectures specifically designed for students and scientists starting in this field.

The Conference consists of oral presentations and vibrant poster sessions. The wish of the organizers is to provide a platform for discussing new developments and concepts within various disciplines of photonics, by bringing together researchers from academia, government and industrial laboratories for scientific interaction, the showcasing of new results in the relevant fields and debate on future trends. This year our conference will contribute celebration of the International Year of Light as a global initiative which will highlight to the citizens of the world the importance of light and optical technologies. This PHOTONICA 2015 will include two COST Action meetings and one workshop with the main objective to promote knowledge in various disciplines of photonics. In addition to the lectures and seminars, a Round Table "Scientific publishing: Editors et altera" will be organized where the editors will present editorial and publishing policies of their journals and share their experiences. Following the official program, the participants will also have plenty of opportunity to mix and network outside of the lecture theatre with planned free time and social events.

This book contains 219 abstracts of all presentations at the **5th International School and Conference on Photonics, PHOTONICA2015**. Authors from 50 countries from all continents will present their work at the conference. There will be six tutorial and seven keynote lectures to the benefits of students and young researches. Twenty four invited lectures, five progress reports of young Serbian researchers and thirty one contributed talks will present most recent results in their research fields. Within the two poster sessions, students and young researches will present 146 poster presentations on their new results in a cozy atmosphere of the Serbian academy of science and arts.

Belgrade, July 2015
Editors

Transparent and conductive films from liquid phase exfoliated graphene

T. Tomašević-Ilić¹, J. Pešić¹, I. Milošević¹, J. Vujin¹, A. Matković¹, M. Spasenović¹ and R. Gajić¹

¹Center for Solid State Physics and New Materials, Institute of Physics, University of Belgrade, Pregrevica 118, 11080 Belgrade, Serbia
e-mail: ttijana@ipb.ac.rs

Liquid phase exfoliation of graphite presents a promising route for large-scale graphene production [1]. We describe basic advantages and disadvantages of the controlled deposition of few-layer graphene using the Langmuir-Blodgett (LB) method, which is compatible with usage in transparent conductors [2,3]. The graphene sheets (GS) were exfoliated from graphite by ultrasonic treatment in N-Methyl-2-pyrrolidone (NMP) and dimethylacetamide (DMA) solvents. For comparison, graphene sheets were also exfoliated in a water solution of surfactants. We confirm a higher exfoliation rate for surfactant-based processing compared to NMP and DMA. Furthermore, we demonstrate that our films exfoliated in NMP and DMA and deposited with LB have a higher optical transmittance compared to films obtained with vacuum filtration, which is a necessary step for GS exfoliated in water solutions [4]. The structural, optical and electrical properties of graphene layers were characterized with scanning electron microscopy, atomic force microscopy, ellipsometry, UV/VIS spectrophotometry and sheet resistance measurements. Our facile and reproducible method results in high-quality transparent conductive films with potential applications in flexible and printed electronics and coating technology.

This work is supported by the Serbian MPNTR through Projects OI 171005 and Innovation Project 451-03-2802-IP/1/167 and by Qatar National Research Foundation through Projects NPRP 7-665-1-125.

REFERENCES

- [1] K. R. Paton et al., *Nat. Mater.* 13, 624 (2014).
- [2] H. K. Kim et al., *Nanoscale* 5, 12365 (2013).
- [3] F. Bonaccorso et al., *Nat. Photon.* 4, 611 (2010).
- [4] M. Lotya et al., *J. Am. Chem. Soc.* 131, 3611 (2009).

XIX Symposium on
Condensed Matter Physics
SFKM 2015

Book of Abstracts



The 19th Symposium on Condensed Matter Physics - SFKM 2015, Belgrade - Serbia

Conference Chair

Leonardo Golubović, *West Virginia University*

Co-Chairs

Antun Balaž, *Institute of Physics Belgrade*

Igor Herbut, *Simon Fraser University*

Mihajlo Vanević, *Faculty of Physics Belgrade*

Nenad Vukmirović, *Institute of Physics Belgrade*

Organizing Committee

Antun Balaž, *Institute of Physics Belgrade*

Edib Dobardžić, *Faculty of Physics Belgrade*

Marko Mladenović, *Institute of Physics Belgrade*

Jovana Petrović, *Vinča Institute of Nuclear Sciences*

Mihajlo Vanević, *Faculty of Physics Belgrade*

Vladimir Veljić, *Institute of Physics Belgrade*

Nenad Vukmirović, *Institute of Physics Belgrade*

Organized by

Institute of Physics Belgrade

Faculty of Physics Belgrade

Vinča Institute of Nuclear Sciences

Serbian Academy of Sciences and Arts

Program Committee

Nataša Bibić, *Vinča Institute of Nuclear Sciences*

Ivan Božović, *Brookhaven National Laboratory*

Milan Damnjanović, *Faculty of Physics Belgrade*

Vladimir Dobrosavljević, *Florida State University*

Laszlo Forro, *EPFL Lausanne*

Gyula Eres, *Oak Ridge National Laboratory*

Radoš Gajić, *Institute of Physics Belgrade*

Zoran Hadžibabić, *Cambridge University*

Igor Herbut, *Simon Fraser University*

Zoran Ikonić, *University of Leeds*

Darko Kapor, *Dept. of Physics, University of Novi Sad*

Irena Knežević, *University of Wisconsin Madison*

Milan Knežević, *Faculty of Physics Belgrade*

Miodrag Kulić, *Goethe-Universität Frankfurt*

Milica Milovanović, *Institute of Physics Belgrade*

Ivanka Milošević, *Faculty of Physics Belgrade*

Branislav Nikolić, *University of Delaware*

Čedomir Petrović, *Brookhaven National Laboratory*

Zoran Popović, *Institute of Physics Belgrade*

Velimir Radmilović, *Faculty of Technology and Metallurgy Belgrade*

Zoran Radović, *Faculty of Physics Belgrade*

Miljko Satarić, *Faculty of Technical Sciences Novi Sad*

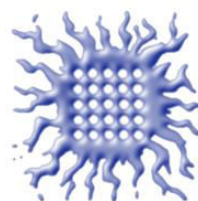
Vojislav Spasojević, *Vinča Institute of Nuclear Sciences*

Bosiljka Tadić, *Jožef Štefan Institute Ljubljana*

Milan Tadić, *School of Electrical Engineering Belgrade*

Filip Vukajlović, *Vinča Institute of Nuclear Sciences*

Ministry of Education, Science and Technological Development of Republic of Serbia
has financially supported the organization of SFKM 2015.



XIX Symposium on Condensed Matter Physics SFKM 2015

Conference Topics

Conference presentations cover a wide range of research topics within the experimental, theoretical, and computational condensed matter physics, including but not limited to the following:

Semiconductor physics: Electronic structure, Quantum dots and wires, Photonic crystals, High magnetic fields phenomena, Ultra-fast phenomena

Surface, interface, and low-dimensional physics: Graphene, Carbon and other nanotubes, Topological insulators, Complex oxide interfaces, Transport in nanostructures

Magnetism: Magnetic materials and phase transitions, Magneto-electronics and spintronics, Magnetic nanoparticles

Superconductivity: Conventional, high T_c , and heavy-fermion superconductors: Materials and mechanisms, Heterostructures: Proximity effect and transport phenomena

Strongly correlated and disordered systems: Materials with strong correlations and disorder, Dynamical properties from time-resolved experiments, Quantum fluids, Cold atoms and BEC

Phase transitions, phase ordering, and structural ordering of condensed matter: Equilibrium and dynamic phenomena, Ferroelectricity, Multiferroics, Quasi-Crystals, Crystal surface morphology and dynamics, Crystal growth

Soft and biological matter: Polymers, Liquids and gels, Liquid crystals, Elastomers, Membranes, Living cells and living matter

Statistical physics of complex systems: Networks and other structures

Conference venue:

Serbian Academy of Sciences and Arts, Knez Mihailova 35, Belgrade

Conference website: <http://www.sfkm.ac.rs>

Spectroscopic And Scanning Probe Microscopic Investigations And Characterization Of Graphene

A. Matković^a, I. Milošević^a, M. Milićević^a, A. Beltaos^a, T. Tomašević-Ilić^a, J. Pešić^a, M. M. Jakovljević^a, M. Musić^a, U. Ralević^a, M. Spasenović^a, Dj. Jovanović^a, B. Vasić^a, G. Isić^a and R. Gajić^a

^aCenter for Solid State Physics and New Materials, Institute of Physics, University of Belgrade, Pregrevica 118, 11080 Belgrade, Serbia

Abstract. Graphene synthesized by various techniques has different properties. Here we give an overview of several graphene synthesis techniques and device fabrication processes; as micromechanical exfoliation, fabrication of free standing membranes, chemical vapor deposition, liquid phase exfoliation, Langmuir-Blodgett assembly, wet transfer, shadow mask and UV photolithography. We employ various scanning probe and optical spectroscopy techniques to determine how these different fabrication processes affect properties of graphene, and present advantages and drawbacks for various applications.

In particular we focus on optical properties of graphene obtained using spectroscopic ellipsometry, and how these are altered by the interaction with an ambient [1], or various dielectric and metallic substrates [2], or by different fabrication processes [3]. We highlight how transfer residue and sample annealing affect optical properties of graphene [3], as well as how the interaction between graphene and a gold substrate can be observed through spectroscopic ellipsometry and Kelvin probe force microscopy [2]. In addition, we demonstrate how graphene can be manipulated by an atomic force microscope, using dynamic plow lithography [4].

Acknowledgement: This work is supported by the Serbian MPNTR through Projects OI 171005, III 45018, 451-03-2802-IP/1/167, by the EU FP7 project NIM_NIL (gr. a. No 228637 NIM_NIL: www.nimnil.org), and by the Qatar National Research Foundation through Project NPRP 7-665-1-125.

REFERENCES

1. Matković, A., Beltaos, A., Milićević, M., Ralević, U., Vasić, B., Jovanović, Dj., and Gajić, R., *Journal of Applied Physics* **112**, 123523 (2012).
2. Matković, A., Milićević, M., Chhikara, M., Ralević, U., Vasić, B., Jovanović, Dj., Belić, M., Bratina, G., and Gajić, R., *Journal of Applied Physics* **117**, 015305 (2015).
3. Matković, A., Ralević, U., Chhikara, M., Jakovljević, M. M., Jovanović, Dj., Bratina, G., and Gajić, R., *Journal of Applied Physics* **114**, 093505 (2013).
4. Vasić, B., Kratzer, M., Matković, A., Nevsad, A., Ralević, U., Jovanović, Dj., Ganser, C., Teichert, C., and Gajić, R., *Nanotechnology* **24**, 015303 (2013).

Chemical Doping Of Langmuir-Blodgett Assembled Graphene Films For Flexible Transparent Conductive Electrodes

A. Matković^a, I. Milošević^a, M. Milićević^a, T. Tomašević-Ilić^a, J. Pešić^a, M. Musić^a, M. Spasenović^a, Dj. Jovanović^a, B. Vasić^a, M. R. Belić^b and R. Gajić^a

^aCenter for Solid State Physics and New Materials, Institute of Physics, University of Belgrade, Pregrevica 118, 11080 Belgrade, Serbia

^bTexas A&M University at Qatar, P.O. Box 23874 Doha, Qatar

Abstract. We demonstrate how chemical doping can be used to enhance properties of liquid-phase exfoliated (LPE) graphene films. Langmuir-Blodgett assembly (LBA) on a water-air interface was used to fabricate multi-layer graphene films several square centimeters in size (Fig. 1(a)). Sheet conductivity of these films is enhanced through doping with nitric acid, leading to a fivefold improvement while retaining the same transparency as un-doped films (Fig. 1(b)). In addition, chemical doping increases the work function by 0.75 eV, to a value of 4.95 eV, making these films a promising candidate for anode electrodes in hybrid solar cells and organic electronics.

Acknowledgement: This work is supported by the Serbian MPNTR through Projects OI 171005, III 45018, 451-03-2802-IP/1/167 and by the Qatar National Research Foundation through Project NPRP 7-665-1-125.

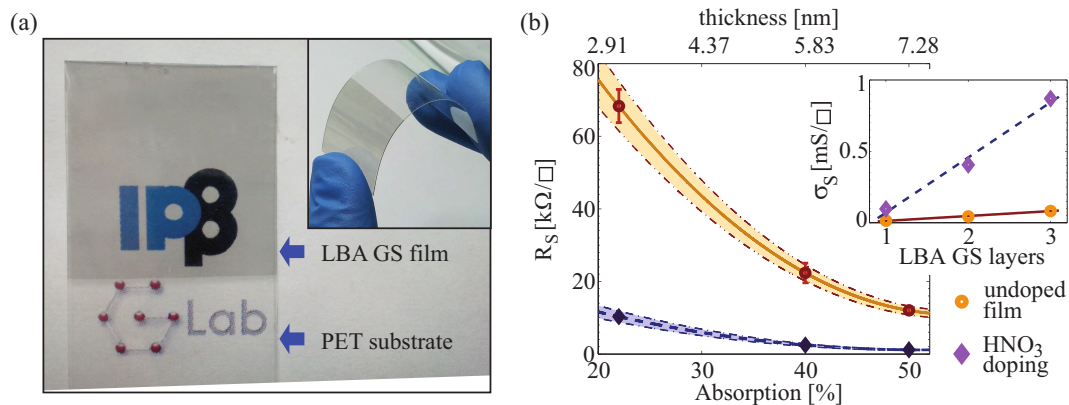


FIGURE 1. (a) 2×2 cm² LBA graphene sheet (GS) film on a polyethylene terephthalate (PET) substrate. (b) The sheet resistance (R_S) and sheet conductivity (σ_S) (inset) of stacked LBA GS layers, prior and after chemical doping.



Society of Physical Chemists of Serbia

PHYSICAL CHEMISTRY 2021

*15th International Conference on
Fundamental and Applied Aspects of
Physical Chemistry*

PC2021

The Conference is dedicated to the

30th Anniversary of the founding of the Society of Physical Chemists of Serbia

and

100th Anniversary of Bray-Liebhafsky reaction



PHYSICAL CHEMISTRY 2021

15th International Conference on Fundamental and Applied Aspects of Physical Chemistry

Organized by

The Society of Physical Chemists of Serbia (SPCS)



in co-operation with

Institute of Catalysis, Bulgarian Academy of Sciences



Boreskov Institute of Catalysis, Siberian Branch of Russian Academy of Sciences



and

Members of the University of Belgrade:



Faculty of Physical Chemistry



Institute of Chemistry, Technology and Metallurgy



VINČA Institute of Nuclear Sciences



Faculty of Pharmacy



and

Institute of General and Physical Chemistry, Belgrade





PHYSICAL CHEMISTRY 2021

International Organizing Committee

- Chairman:** S. Anić (Serbia)
Vice-chairman: M. Gabrovska (Bulgaria)
 A. A. Vedyagin (Russia)
 S. N. Blagojević (Serbia)
- Members:** N. Cvjetičanin (Serbia), S. M. Blagojević (Serbia), M. Daković (Serbia), J. Dimitrić-Marković (Serbia), T. Grozdić (Serbia), Lj. Ignjatović (Serbia), D. Jovanović (Serbia), M. Kuzmanović (Serbia), D. Marković (Serbia), B. Milosavljević (USA), M. Mojović (Serbia), N. Pejić (Serbia), M. Petković (Serbia), A. Popović-Bjelić (Serbia), B. Simonović (Serbia), M. Stanković (Serbia), B. Šljukić (Serbia), G. Tasić (Serbia), S. Veličković (Serbia), N. Vukelić (Serbia),

International Scientific Committee

- Chairman:** Ž. Čupić (Serbia)
Vice-chairman: V. Bukhtiyarov (Russia)
 S. Todorova (Bulgaria)
 B. Adnađević (Serbia)
- Members:** S. Anić (Serbia), A. Antić-Jovanović (Serbia), A. Azizoğlu (Turkey), R. Cervellati (Italy), G. Ćirić-Marjanović (Serbia), V. Dondur (Serbia), I. I. Grinvald (Russia), R. Jerala (Slovenia), M. Jeremić (Serbia), G. N. Kaluđerović (Germany), E. Kiš (Serbia), A.V. Knyazev (Russia), Lj. Kolar-Anić (Serbia), U. Kortz (Germany), T. Kowalska (Poljska), A. Lemarchand (France), G. Lente (Hungary), Z. Marković (Serbia), S. Mentus (Serbia), K. Novaković (UK), N. Ostrovski (Serbia), V. Parmon (Russia), Z. Petkova Cherkezova-Zheleva (Bulgary), M. Plavšić (Serbia), J. Savović (Serbia), G. Schmitz (Belgium), I. Schreiber (Czech), L. Schreiberova (Czech), D. Stanisavljev (Serbia), N. Stepanov (Russia), M. Stojanović (USA), E. Szabó (Slovakia), Zs. Szakacs (Romania), Z. Šaponjić (Serbia), Á. Tóth (Hungary), M. Trtica (Serbia), V. Vasić (Serbia), D. Veselinović (Serbia), V. Vukojević (Sweden)

Local Executive Committee


- Chairman:** S. N. Blagojević
Vice-chairman: A. Ivanović-Šašić
 N. Jović-Jovičić
 A. Stanojević
- Members:** M. Ajduković, I. N. Bujanja, A. Dobrota, J. Dostanić, D. Dimić, S. Jovanović, Z. Jovanović, D. Lončarević, M. Kragović, J. Krstić, B. Marković, S. Maćešić, J. Maksimović, S. Marinović, D. Milenković, T. Mudrinić, M. Pagnacco, N. Potkonjak, B. Stanković, I. Stefanović, G. Stevanović, A. Stojković, M. Vasić

Event Schedule

Tue Sep 21	Wed Sep 22
---------------	---------------

🌐 Displaying agenda in event timezone (11:05 AM CEST)

Oral Lecture H5 - CHEMICAL DOPING OF LANGMUIR-
BLODGETT ASSEMBLED FEW-LAYER GRAPHENE
FILMS WITH Li AND Au SALTS

3:00 PM - 3:10 PM

 Live Stream: [Join stream](#)

Ivana Milošević
Assistant Research Professor
Institute of Physics Belgrade
[Speaker's Page](#)

C


Event Schedule




Thu
Sep 23

Fri
Sep 24

🌐 Displaying agenda in event timezone (11:25 AM CEST)

Oral Lecture K1 - UPTAKE AND ACCUMULATION OF 
Pb AND Ni IN SPRUCE AND DOUGLAS-FIR TREE-
RINGS AND BARK

1:20 PM - 1:30 PM

 Live Stream: [Join stream](#)

Ivana Milošević
Assistant Research Professor
Institute of Physics Belgrade
[Speaker's Page](#)
